# MULTISCALE MODELING AND SIMULATION OF DAMAGE BY VOID NUCLEATION AND GROWTH

Thesis by

Celia Reina Romo

In Partial Fulfillment of the Requirements

for the Degree of

Doctor of Philosophy


California Institute of Technology

Pasadena, California

2011

(Submitted November 4, 2010)

*To my parents*

# Acknowledgements

I owe so much to so many people, that this acknowledgment section cannot be complete. I will therefore explicitly thank a few people and hope to implicitly thank the rest of them.

First and foremost I truly want to thank my supervisor Professor Michael Ortiz. It has been a great honor to work with him as well as an extremely fun experience. The work written here is the result of many hours of exciting discussions and it would not have been possible without his guidance, his enthusiasm and his continuous encouragements and efforts towards our objectives. *¡Gracias Miguel!*. The second person to whom I am very grateful is Jaime Marian. I had the pleasure to work with him during a 10-week stay at Lawrence Livermore National Laboratory and since then, he has served as a mentor and a friend. Chapter 2 is work that has been done in very close collaboration with him.

I would like to thank my committee members, Professor Guruswami Ravichandran, Professor Kaushik Bhattacharya and Professor Chiara Daraio, for their expert advice on my thesis work as well as on my future plans. I would like to acknowledge as well the support received from the faculty members at my university in Seville. In particular, I would like to thank Pilar Ariza who made possible my arrival at Caltech through the Fellowship from the Agency of Innovation and Development of Andalusia. Very certainly, this thesis would have not happened without it.

I also owe my deepest gratitude to Paco, who has always been available for discussion and has shown his support in many different ways, and to my colleagues and friends Luigi, Olive, Sigrid, Kerstin, Phanish, Daniel and Malena amongst others. Interaction with them was highly beneficial for the completion of this work. In addition, I would like to give special thanks to Bo, who made possible the parallel simulations shown in Section 3.8.

I would like to extend my warmest thanks to Lydia and Marta who made my life in the office a lot more enjoyable. Always ready to help, they have been an essential support

during all these years.

Finally, but certainly not least, I would like to acknowledge all my friends (at Caltech and abroad) and my family, who have always encouraged me to pursue my dreams and have made me happy everywhere I have been. In particular I would like to express my gratitude to my parents and my sister, whom I deeply admire and to whom I simply owe everything.

# Abstract

Voids are observed to be generated under sufficient loading in many materials, ranging from polymers and metals to biological tissues. The presence of these voids can have drastic implications at the macroscopic level including strong material softening and more incipient fracture. Developing tools to appropriately account for these effects is therefore very desirable.

This thesis is concerned with both, the appearance of voids (nucleation process) and the modeling and simulation of materials in the presence of voids. A particular nucleation mechanism based on vacancy aggregation in high purity metallic single crystals is analyzed. A multiscale model is developed in order to obtain an approximate value of the time required for vacancies to form sufficiently large clusters for further growth by plastic deformation. It is based on quantum mechanical results, kinetic Monte Carlo methods and continuum mechanics estimates calibrated with quasi-continuum results. The ultimate goal of these simulations is to determine the feasibility of this nucleation mechanism under shock loading conditions, where the temperature and tensions are high and vacancy diffusion is promoted.

On the other hand, the effective behavior of materials with pre-existent voids is analyzed within the general framework of continuum mechanics and is therefore applicable to any material. The overall properties of the heterogeneous material are obtained through a two-level characterization: a representative volume element consisting of a hollow sphere is used to describe the "microscopic" fields, and an equivalent homogeneous material is used for the "macroscopic" behavior. A variational formulation of this two-scale model is presented. It provides a consistent definition of the macro-variables under general loading conditions, extending the well-known static averaging results so as to include microdynamic effects under finite deformations. This variational framework also provides a suitable starting point for time discretization and consistent definitions within discrete

time. The spatial boundary value problem resulting from this multiscale model is solved with a particular spherical shell element specially developed for this problem. The approximation space is based on spherical harmonics, which respects the symmetries of the porous material and allows the representation of the fields on the sphere with very few degrees of freedom. Numerical tools, such as the exact representation of the boundary conditions and an exact quadrature rule, are also provided. The resulting numerical model is verified extensively, demonstrating good convergence results, and its applicability is shown through several material point calculations and a full two-scale finite element implementation.

# Contents

# List of Figures

# List of Tables

# Chapter 1

# Introduction

Voids are observed to be generated under sufficient loading in many materials (see 1.1), ranging from polymers (Gent and Lindley, 1958, Huang and Kinloch, 1992, Azimi et al., 1996) and metals (Tvergaard, 1990) to biological tissues (Pishchalnikov et al., 2003). Even materials that are nominally "pure" are seen to develop voids in order to accommodate the applied deformation (Bauer and Wilsdorf, 1973).

The presence of initial microscopic defects in the form of voids can have drastic implications at the macroscopic level. In the case of elastomers, the maximum pressure that the solid can sustain changes from a theoretical infinite value for an undamaged material, to a well defined finite value when those defects are considered (Ball, 1982). This critical pressure is associated to a sudden increase in the void volume fraction, a phenomenon called cavitation, which weakens the material and ultimately leads to the fracture of the specimen. In the case of metals, small void volume concentrations can also substantially alter the plastic behavior. The usual assumption of plastic incompressibility does not hold from a macroscopic perspective in the presence of voids. An effective change in volume occurs by void growth and incompressible plastic deformation of the matrix surrounding the cavity. As a result, both, the yield surface of the porous material and fracture initiation, become sensitive to volumetric stress states (Hancock and Mackenzie, 1976, Johnson and Addessio, 1985b). Developing modeling tools to appropriately account for these effects is therefore very desirable. This thesis is concerned with the appearance of the voids in the material (the nucleation process), which is treated in Chapter 2, and the modeling and simulation of material with voids (porous material), which is the subject of Chapter 3. The nucleation process is very material specific. The present study is limited

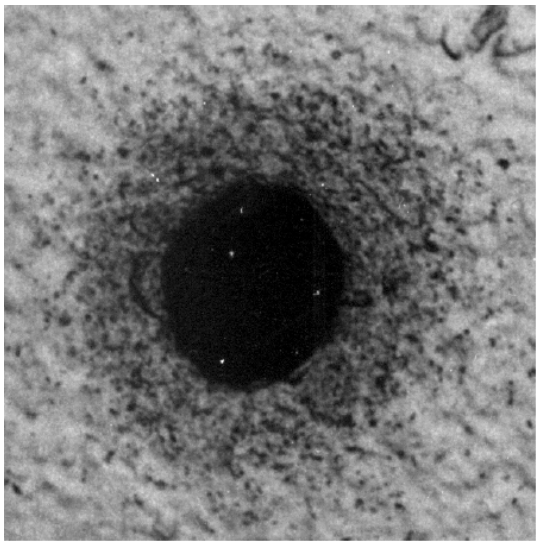

(a)

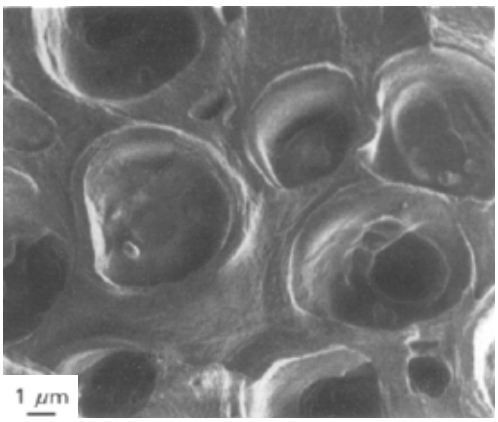


(b)

(c)

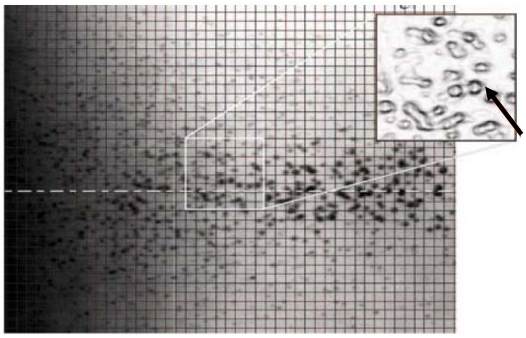

(d)

(e)

Figure 1.1: Presence of voids in different materials. (a) Plastically deformed zone surrounding an incipient void. Belak (2005). (b) Scanning electron micrograph of the fracture surface of rubber-modified epoxy polymers. Azimi et al. (1996). (c) Quasi-static rupture of a copper sample. Curran et al. (1977). (d) Experimental observation of kidney tissue subjected to shock-wave lithotripsy. Bailey et al. (2003). (e) Partial spall on a 5 mm aluminum plate of commercial purity. Curran et al. (1977).

to a particular nucleation mechanism of interest in ductile failure. It is based on vacancy diffusion in high-purity metallic single crystals under extreme conditions. Damage evolution under preexistent voids, on the other hand, is treated within the general framework of continuum mechanics and is therefore applicable to any material.

Throughout this thesis a multiscale approach is adopted so as to root the behavior of the material at a given scale in the response at the lower scales. In the classical description of materials, the effective response is characterized by a few numbers, called "material parameters", which allow us to describe the behavior in a simplistic way, hiding the underlying complexity that is ultimately responsible for such behavior. This includes parameters such as Young's modulus, Poisson's ratio, strain hardening or critical energy release rate at the macroscopic level, and diffusion coefficient or cohesive energy for instance, at an atomistic level. This simplification is very appealing. The problem relies on the fact that these "material properties" are not really intrinsic. Rather, they can be highly dependent on the load history of the material in question, and a single set of numbers is unable to describe the response under varying conditions. This is particularly true in the presence of damage, which is the situation of interest in the present study. The ultimate goal of this type of multiscale models is to enable numerical simulations with predictive capability. This would be very desirable as a design tool, reducing tremendously the experimental costs, and would also allow us to be predictive in situations where experiments are not possible. Current limitations of multiscale models lie in validation at the lower scales, which is of great experimental difficulty. However, recent experimental developments, such as X-ray tomography (Maire et al., 2005, Morgeneyer et al., 2008) or high-angle annular dark-field imaging in a scanning transmission electron microscopy (Voyles et al., 2002, Kaiser et al., 2002) hold great promise for generating accurate models.

Ductile failure, which is of high interest in industrial applications and in this work, is an example of a complex process that is inherently multiscale. More particularly, this type of failure occurs via nucleation, growth, and coalescence of voids (Garrison and Moody, 1987) both under quasi-static and dynamic loading conditions. Classical fracture theory describes the growth of a flaw based on the critical value of the stress intensity factor K (Irwin and Washington, 1957) or of the J-integral (Rice, 1968). See for instance Kanninen and Popelar (1985) for a comprehensive treatment of fracture mechanics. In general,

as previously mentioned, such critical values are not really material parameters. This is especially the case for ductile materials, in which the the crack advance is governed by the nucleation and growth of voids, a phenomenon that is dependent on the complete load history (Curran et al., 1977). This observation has lead to the development of more physically based descriptions of fracture (see review paper Pineau (2006)). Due to its importance, a large number of authors have contributed to the field with more phenomenological continuum damage mechanic theories (Tuler and Butcher, 1968, Chaboche, 1988), micromechanically based models (Gurson, 1977a, Curran et al., 1977, Koplik and Needleman, 1988, Tvergaard, 1990, Pardoen and Hutchinson, 2000, Rudd and Broughton, 2000, Antoun et al., 2003, Weinberg and Ortiz, 2009) or molecular dynamics simulations (Rudd and Belak, 2002, Seppälä et al., 2004, Marian et al., 2004, 2005, Ahn et al., 2007, Potirniche et al., 2006, Zhu et al., 2007, Dvila et al., 2005). A complete review of the different proposed approaches is out of the scope of this manuscript. Only the relevant background for the work presented here is summarized in the corresponding chapters.

The goal of this thesis is to develop nucleation and growth models that could ultimately be included in a complete multiscale model of failure. These two phenomena are treated independently here. The rigorous connection between them and the study of the final stage of failure remains an open problem that requires further analysis. In the following, a brief introduction to the nucleation in ductile materials is presented and an outline of the work developed in each chapter is provided.

It is well known that void nucleation in ductile materials occurs mainly at second-phase particles by interfacial decohesion or particle fracture (Puttick, 1959, Goods and Brown, 1979). See for instance, Fig.1.2(a), where the growth of voids within an inclusion colony is shown. Models for this type of nucleation exist and are usually based on the stresses or the strains at the interface (Gurson, 1977b, Neddleman, 1987). In polycrystals, grain boundaries and triple points are also weak points that supply preferred nucleation sites (Hull and Rimmer, 1959, Christy et al., 1986, Belak, 1998, Rudd and Belak, 2002). Fig. 1.2(b) shows experimental evidence of this nucleation process. Although neither of these two mechanisms can operate in high-purity single crystals, void growth and coalescence is still observed experimentally (Bauer and Wilsdorf, 1973). Lyles and Wilsdorf (1975) suggested that, in such cases, nucleation may take place by clustering of vacancies produced

during plastic deformation, irradiation, quenching, or by other means (Cawthorne and Fulton, 1967). Chapter 2 addresses this latter mechanism. In particular, the attempt is to estimate critical times required for the nucleation of nanovoids via vacancy aggregation in high-purity single crystals and to determine if it is fast enough to operate under shock loading conditions.

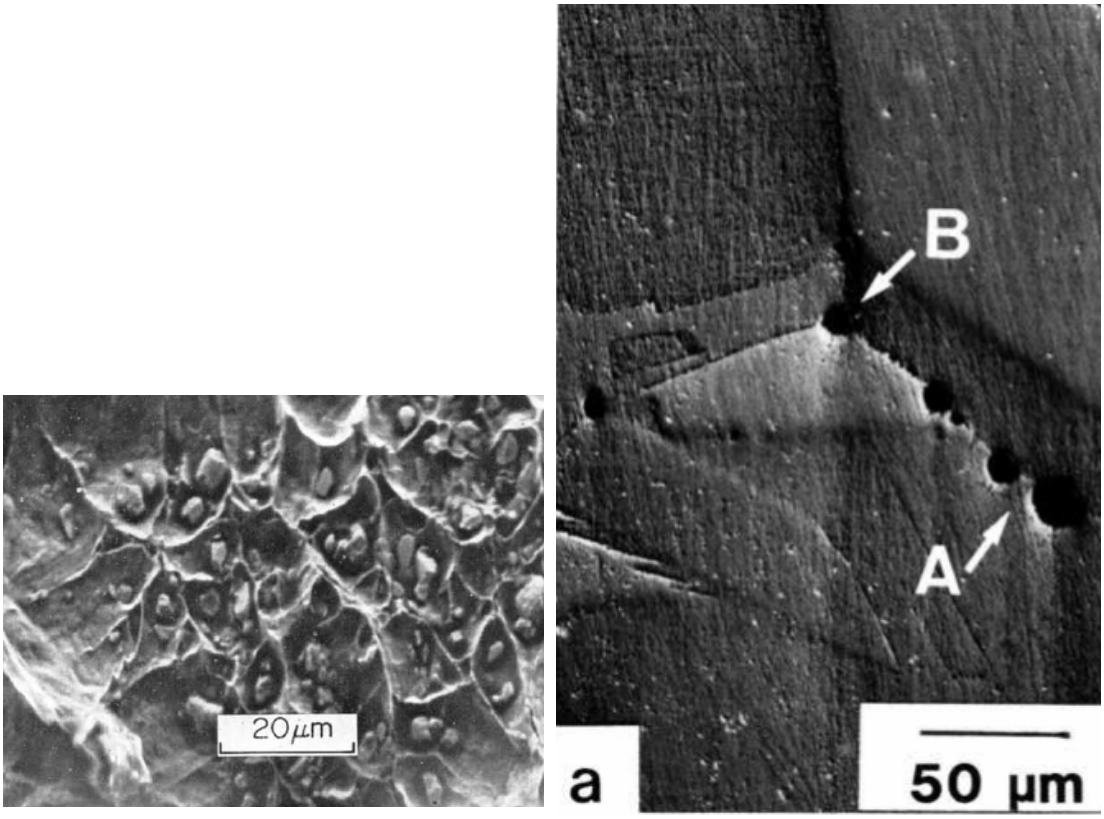


(a) (b)

Figure 1.2: Various nucleation sites. (a) Void growth within an inclusion colony in a low-alloy, quenched and tempered steel. Hancock and Mackenzie (1976). (b) Nucleation of spherical voids at grain boundary and grain boundary triple point. Christy et al. (1986).

In the vacancy-diffusion problem, many spatial and temporal scales can be identified (Phillips, 2001). The smallest scale is associated with the electronic degrees of freedom, a subject of quantum mechanics. The next scale corresponds to the thermal vibration of the atoms around their equilibrium position, which is followed by the time span associated with the jump frequency of the atoms towards empty neighboring positions. The last identifiable time scale emerges from the accumulation of sufficient discrete jumps, resulting in a local concentration change. The methodology employed in this thesis takes advantage of this separation of time scales to build a model in which parameters are obtained from

results at the lower scales. In particular, a kinetic Monte Carlo approach is used to describe the discrete atomic jumps. Such a model uses jump rates that emanate from statistical mechanics, and the parameters involved are taken from quantum mechanical calculations, in particular orbital-free density functional theory. Finally, this atomistic model is used to determine the time required for vacancies to aggregate into clusters of a size that is visible macroscopically under shock loading conditions. The proposed nucleation criterion is based on the critical size for subsequent growth by dislocation-mediated plasticity (see Meyers et al. (2009) for a review of the role of dislocations on void growth). A continuum mechanics estimate calibrated with quasi-continuum models of void growth (Marian et al., 2004) is developed to determine such critical size. The computed nucleation times resulting from the analysis suggest that vacancy aggregation and cluster coarsening is a feasible mechanism of nanovoid nucleation in high-purity aluminum single crystals over pulse durations, temperatures and tensile volumetric strains typical of, for example, spall tests.

In Chapter 3, an attempt is made towards defining the overall dynamic behavior of materials where voids have already nucleated. This is done through a two-level representation of the material. The lower scale, termed "microscopic", is treated through a representative volume element (RVE) composed of two phases: a homogeneous matrix and voids. The behavior of the RVE is then suitably averaged to provide the so called macroscopic behavior of the material, which is now treated as homogeneous. The connection between the two scales is well understood for the static case under infinitesimal (Hill, 1963, 1967) and large strains (Hill, 1972, Ogden, 1974, Castañeda, 1991, Nemat-Nasser, 1999). However, the connection between the micro and macro levels is less well understood under dynamic loading, and little can be found in the literature in that respect (Molinari and Mercier, 2001, Wang and Sun, 2002). The work presented in the first part of Chapter 3 is an effort towards building such a connection. In particular, fully consistent macroscopic quantities are derived that behave exactly as the local counterparts under dynamic conditions. The extension to dynamics is made by taking a variational perspective of the two-level problem and by selecting suitable boundary conditions to impose over the RVE. This variational structure also allows us to take advantage of the variational integrators for time discretization and the macro-variables are immediately defined within discrete

time. The formulation presented is not restricted to this particular case of heterogeneity. The range of applications is very wide and extends to composites and materials with evolving microstructure.

The second part of Chapter 3 is dedicated to the spatial discretization. The RVE chosen to represent porous materials is the hollow sphere, as thought of by Gurson (1977a). A particular type of finite element, adapted to the considered geometry, is developed. It consists of an approximation space based on spherical harmonics. This set of functions constitutes a complete orthogonal space on the sphere, and is therefore suitable for a finite element discretization. Two specific properties make this discretization advantageous with respect to more standard finite element formulation. First, it allows a representation of the different fields on the sphere with a very low number of degrees of freedom, and secondly and most importantly, the symmetries of the porous material, if existent, are respected upon discretization. The necessary tools for solving boundary value problems on the hollow sphere are also provided. This includes a quadrature rule that integrates exactly the stiffness matrix, the mass matrix and the void volume fraction under the proposed discretization; and an explicit analytic formula for imposing the boundary conditions that emanated from the consistent two-level representation of the porous material.

The resulting finite element procedure has been verified extensively. Comparisons with several analytic solutions are performed and convergence analyses indicate close to ideal convergence rates for different materials under arbitrary loading conditions. This work is then concluded by the multiscale simulation of a real example problem in order to demonstrate its applicability. The example consists of a high speed Taylor test of polyurea material. A material model for polyurea is proposed and the results are compared with experimental observations.

Finally, some conclusions about the work presented are provided in Chapter 4, where some ideas for future directions are also discussed.

# Chapter 2

# Nucleation of voids

## 2.1 Introduction

This chapter is concerned with the nucleation of voids via diffusion-mediated vacancy aggregation in high-purity metallic single crystals. This is an accepted nucleation mechanism in failure under creep at elevated temperatures (Raj and Ashby, 1975, Cocks and Ashby, 1982). More debate exists, though, in the literature as to its viability as a nucleation mechanism in fast failure processes under extreme conditions. The present work is concerned with the latter. More precisely, a multiscale model based on first principles is developed. It allows the determination of the time required for the voids to attain a size that can alter the macroscopic behavior.

Qualitatively, the diffusion of an atom to a empty neighbor position in the lattice evolves in the following manner. By thermal excitation, the atom is in permanent vibration around its equilibrium position. These vibrations can be seen as attempts to cross the saddle point separating the two neighboring potential wells. If one of these attempts is successful, the system evolves to a new configuration characterized by different vacancy positions. This process is commonly referred to as vacancy movement, although, obviously, the atoms are the entities in motion. By this mass transport process, vacancies can find each other to form aggregates or clusters. The energy of such clusters is in general smaller than the energy of the system with isolated vacancies. Therefore, the system tends to evolve towards vacancy aggregation. This process of vacancy condensation and cluster coarsening is diffusion-limited, and therefore sensitive to temperature, pressure and microstructure, e.g., dislocation density and grain boundaries.

The details of these diffusion processes can be computed accurately by means of molecular dynamic calculations (Sinno et al., 1996, Hastings et al., 1997, Belak, 1998, Rudd and Belak, 2002), in which the classical equations of motion for the system of atoms are propagated in time. Such computations require the use of very small time steps in the numerical analyses ($\sim 10^{-15}$) and resolve the atomic vibrations, which are not of interest in the present study. Another methodology widely used in diffusive processes is the kinetic Monte Carlo method (Young and Elcock, 1966, A. La Magna, 1999, Haley et al., 2006). In this approach, only the discrete jumps of the vacancies are considered, but an a priori knowledge of the microscopic motions and their rates is required. This is not always trivial, as demonstrated by examples found in the literature of complex non-intuitive transitions occurring in surface and bulk diffusion (Liu and Adams, 1992, Uberuaga et al., 2004). Failure to consider some physically possible motions can lead to an erroneous evolution of the system. Within kinetic Monte Carlo (KMC), the rates of the motions are commonly obtained with transition state theory (Vineyard, 1957), which borrows elements from statistical mechanics. A third alternative to describe the vacancy diffusion process relies on continuum descriptions (Seitz, 1948, Penrose, 1997, Weinberg and Böhme, 2009). The concentration of vacancies is thought of as a function of space and time, and evolution equations are used to describe its progression. This constitutes a more phenomenological description of the diffusion process, but allows the study of very large systems over a long period of time.

As a compromise between accuracy and size of the domain and time span that can be explored computationally, a lattice kinetic Monte Carlo (LKMC) approach is used in this work. A brief review of the algorithms used in the simulations (Bortz et al., 1975, Martinez et al., 2008) is presented in Section 2.3. The required rates of the possible motions are computed by transition state theory with parameters obtained from Orbital Free Density Functional Theory (OFDFT) calculations (Gavini, 2009a, Ho et al., 2007); and by approximating the energy through an Ising Hamiltonian that considers first and second nearest neighbor interactions. The vacancy cluster kinetics are then examined in Section 2.5 with particular regard for the effect of temperature and volumetric strain.

Finally, in Section 2.6 the feasibility of this diffusion-mediated vacancy aggregation and cluster coarsening as a void nucleation mechanism under shock-loading conditions

is discussed for the case of aluminum. Towards that goal, the critical time required for nanovoid nucleation over the range of temperatures and volumetric strains of interest is computed. A void will be considered nucleated when it attains a size sufficient for subsequent growth by dislocation-mediated plasticity. Simple continuum estimates calibrated with quasi-continuum calculations (Marian et al., 2004) are used to determine such critical cavitation sizes. Based on this estimate, together with the LKMC results, the sought-after nanovoid nucleation times as a function of temperature and volumetric strain are computed.

Models of the type just described have been extensively used in the past to simulate vacancy aggregation in metals (A. La Magna, 1999, Lo and Skodje, 2000). These models suffer from several limitations, most notably: the rigid lattice approximation, which neglects elastic interactions between vacancies; the simplified Ising Hamiltonian, which tends to break down for complex cluster geometries and at void surfaces; and limitations attendant to the use of harmonic transition state theory. Because of these and other limitations, it is expected that the results presented in this chapter are mostly qualitative and to mainly provide a preliminary assessment as to the feasibility of nanovoid nucleation by vacancy aggregation at high tensile pressures and temperatures. A number of improvements of LKMC simulations have been proposed (e.g., Dai et al. (2006)) but they will not be considered here in the interest of simplicity.

## 2.2 Physical model

The model system under consideration consists of a face-centered cubic (fcc) aluminum crystal containing a random distribution of vacancies at prescribed temperature, volume and concentration. The system is analyzed in the canonical $nVT$ ensemble, where $n$ is the number of vacancies, $V$ is the periodic cell volume and $T$ is the equilibrium absolute temperature of the sample. The state of the system is taken to be characterized solely by the spatial distribution of vacancies on a frozen lattice. The relaxation of the atoms surrounding the vacancies is partially taken into account through the energies considered. For computational purposes, though, each atomic position is mapped to its ideal lattice position.

The system is assumed to evolve according to the master equation

$$\frac{dp_i}{dt} = \sum_{j \neq i} \left[ r_{ji} p_j - r_{ij} p_i \right] \tag{2.1}$$

where $p_i$ is the probability of finding the system in state $i$ and $r_{ji}$ is the transition rate from state $j$ to $i$. The objective of the simulations is to track the diffusion of the vacancies through the lattice and the attendant formation of clusters of various sizes. As it has previously been mentioned, the master equation 2.1 is solved by means of lattice kinetic Monte Carlo (LKMC), i.e., by allowing the vacancies to execute first nearest-neighbor random jumps. More specifically, the rejection-free, $n$-fold algorithm (also known as "BKL"), both in serial (Bortz et al., 1975) and parallel (Martinez et al., 2008) implementations, is used. These algorithms are reviewed in the following section.

## 2.3 Kinetic Monte Carlo

The "BKL" algorithm is a Monte Carlo method that gives the temporal evolution of Markovian processes through a sequence of Monte Carlo steps. An introduction to the KMC method can be found in Sickafus et al. (2007). The steps consist of the following:

1 Identification of all the possible atomistic motions and their corresponding rates $r_i$. According to the assumptions previously stated, a possible motion consists of the

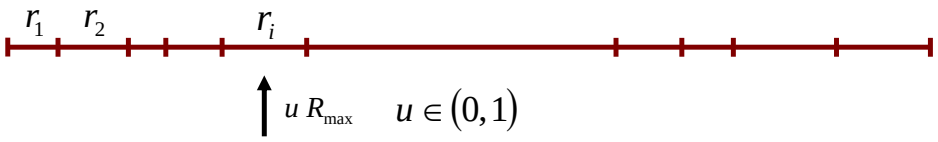


Figure 2.1: Frequency line (aggregate of the individual rates) and schematic representation of the procedure for selecting a vacancy movement with probability $p_i = \frac{r_i}{R_{\max}}$.

movement of a vacancy to a first nearest-neighbor position not occupied by another vacancy. The details of the calculations of the rates are provided in the next section.

2 Computation of the cumulative rates $R_i = \sum_j^i r_j$ and total rate $R_{\max} = \sum_i r_i$.

3 Evolution of the system by carrying out event $i$ satisfying $R_{i-1} \leq uR_{\max} < R_i$, where $u$ is a uniform random number in the interval $(0, 1)$. A schematic illustration of this procedure is shown in Fig. 2.3.

4 Update of the time with a random time step from the exponential distribution for the rate $R_{\max}$. Equivalently, $\Delta t = -\frac{\log \xi}{R_{\max}}$, $\xi$ being another uniform random number in the interval $(0, 1)$. Once the system is in the new state, the list of rates needs to be updated.

5 Repeat the cycle from step 2 until the desired time is reached.

The temporal evolution of the diffusing vacancies is intrinsically sequential, and therefore very difficult to parallelize. The two main issues that arise are the time synchronization between domains and the conflicts between neighboring partitions. However, a parallel implementation is very desirable to analyze larger systems for longer periods of time. There have therefore been significant efforts in the literature towards the objective of parallelization (Lubachevsky, 1988, Johnson and Addessio, 1985a, Shima and Oyane, 2005, Martinez et al., 2008).

The parallel implementation used in this work is the one developed by Martinez et al. (2008). As in any parallel implementation, the computational cell $\Omega$ is divided into several subdomains $\Omega_k$, each of which is provided to a different processing unit. The main characteristic of the algorithm is the perfect synchronicity, which is achieved by the introduction of "null" events (see Fig. 2.3). The rate of the null processes is such

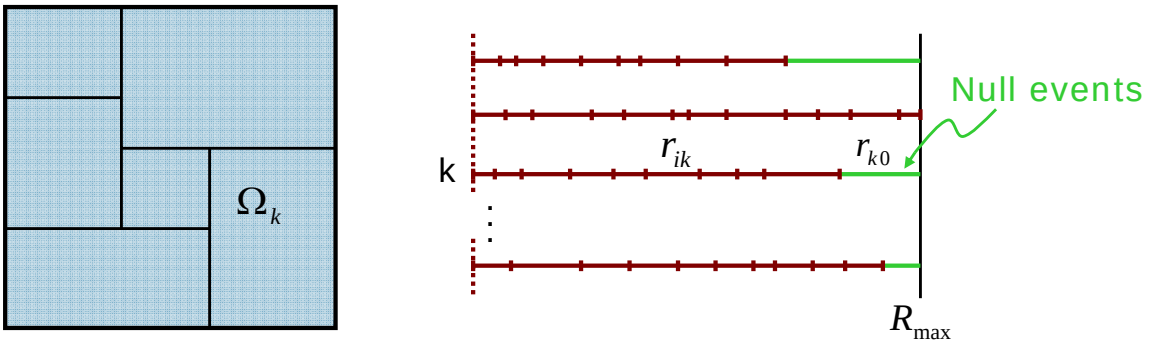


Figure 2.2: Schematic representation of the null events in the synchronous parallel Kinetic Monte Carlo proposed by Martinez et al. (2008)

that $R_{\max}$ is equal in all the domains. If one of such events is chosen in a Monte Carlo step, no action is taken. The null processes therefore slow the system down if compared with perfect speedup, but the partition of the global domain can be performed so as to minimize those null events. Aside from these considerations, the algorithm proceeds in a manner very similar to the serial version. Fig. 2.3 shows the speedup of the parallel code versus the serial one for two different concentrations. It is computed as $\eta = \frac{t_s}{K t_p}$, where $t_s$ and $t_p$ are the computational times for the serial and parallel code respectively, and $K$ is the number of processors. Close to ideal speedup is obtained.

Details on the serial implementation are provided in Section 2.7, whereas the parallel code was implemented by Enrique Martinez, author of the algorithm used.

## 2.4 Rate catalog

The requisite event rates $r_{ij}$ in Eq. (2.1) are assumed to obey harmonic transition state theory (HTST) (Vineyard, 1957). TST assumes that there exists a critical surface between two neighboring potential wells, with the property that if such a surface is crossed, complete transition occurs. It fails to account for those cases in which an atom crosses the surface and returns before complete transition, and therefore tends to overestimate the true rates. Although dynamical corrections exist to recover the exact rates (Keck, 1962), those will not be used in this work. The harmonic assumption, on the other hand, is based on a second order approximation of the potential energy landscape at the bottom of the energy wells (equivalent to harmonic vibration modes) and at the saddle points

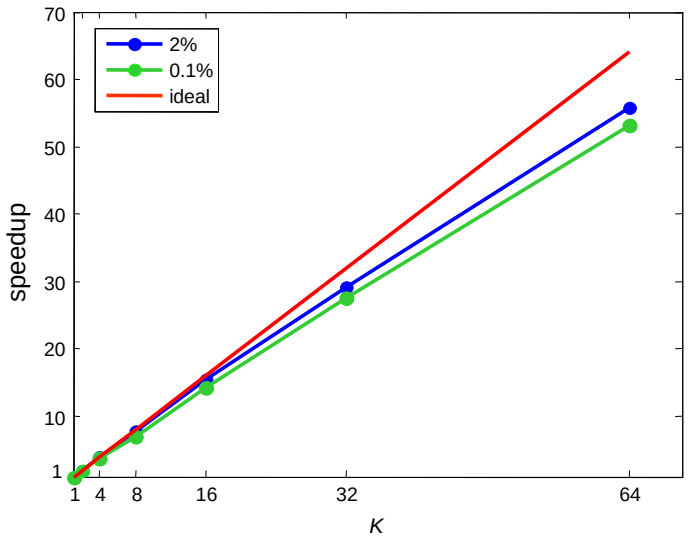


Figure 2.3: Speed improvement obtained with the parallel implementation as a function of the number of processors $K$. Both codes ran on 2.4GHz processors with 16GB of memory per node. Version 1 MPI was used for the parallel implementation. The system analyzed consists of $10^5$ vacancies at $T = 728$ K and $\varepsilon_{vv} = 0$.

in between them. Such approximations tend to be very accurate in solid-state diffusive processes up to at least half the melting temperature, and higher errors are incurred as the temperature increases (Sorensen and Voter, 2000).

Under these assumptions, the rates read (see Weiner (2002), for instance, for a complete derivation)

$$r_{ij} = \begin{cases} \nu e^{-\beta(E_m + \Delta E_{ij})}, & \text{if } \Delta E_{ij} > 0, \\ \nu e^{-\beta(\Delta E_{ij})}, & \text{if } \Delta E_{ij} < 0, \end{cases} \tag{2.2}$$

where $\Delta E_{ij} = E_j - E_i$ is the difference in energy between states $i$ and $j$, $E_m$ is the corresponding migration energy, $\nu$ is the attempt frequency and $\beta = 1/k_B T$, where $k_B$ is Boltzmann's constant and $T$ is the temperature. A schematic representation of the two cases considered is shown in Fig. 2.4. The energy of a distribution of vacancies is assumed to be well approximated by an Ising Hamiltonian with first (1NN) and second nearest-neighbor (2NN) interactions, namely,

$$E = -J \sum_{\langle m,n \rangle} \sigma_m \sigma_n, \quad J = \begin{cases} E_1, & \text{if } \langle m,n \rangle \text{ 1NN}, \\ E_2, & \text{if } \langle m,n \rangle \text{ 2NN}, \\ 0, & \text{otherwise}, \end{cases} \tag{2.3}$$

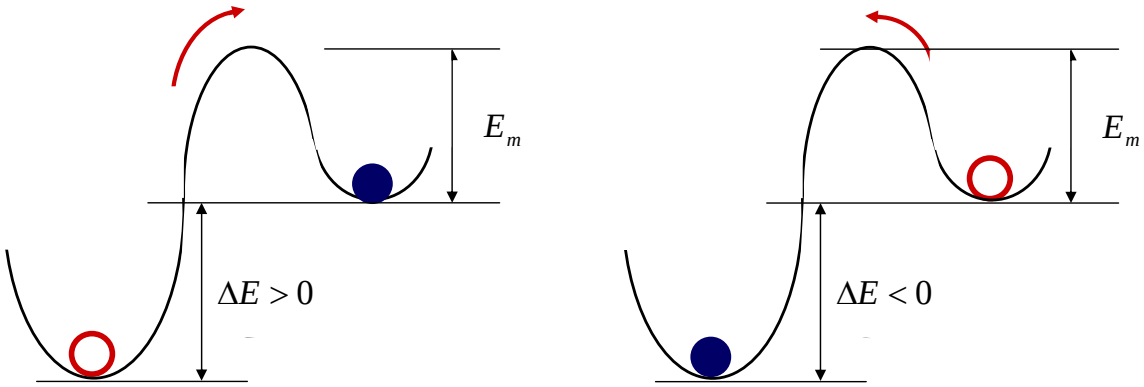


Figure 2.4: Schematic representation of the movement of a vacancy (red color) to a neighboring position with a higher energy (left figure) or lower energy (right figure).

where $\sigma_m \in \{0, 1\}$ is the occupation state of site $m$ of the lattice. The calculations presented here use the di-vacancy binding energies, $E_1$, $E_2$, and the migration energy, $E_m$, computed by Gavini (2009a) using zero-temperature quasi-continuum orbital-free density functional theory calculations (QC-OFDFT). As shown in Fig. 2.5, the di-vacancy binding energies are positive, which promotes vacancy aggregation and subsequent cluster coarsening. The nearest-neighbor binding energy decreases with volumetric strain, regardless of sign, whereas the second nearest-neighbor binding energy decreases monotonically with increasing volumetric strain. Therefore, nearest-neighbor binding is dominant under positive volumetric strain (expansion) whereas both nearest and second-nearest neighbor interactions play a roughly equal role under negative volumetric strain (compression). The migration energy decreases monotonically with increasing volumetric strain, which is expected to accelerate the kinetics. Additionally, the pre-exponential factor $\nu$ calculated by Ho et al. (2007) using OFDFT is used. Fig. 2.4 shows that the jump-attempt frequency decreases monotonically with increasing volumetric strain, which is expected to decelerate kinetics.

The number of possible transition rates for a given temperature and volumetric deformation are finite and comprise a "rate catalog" that can be tabulated and looked up in the simulation.

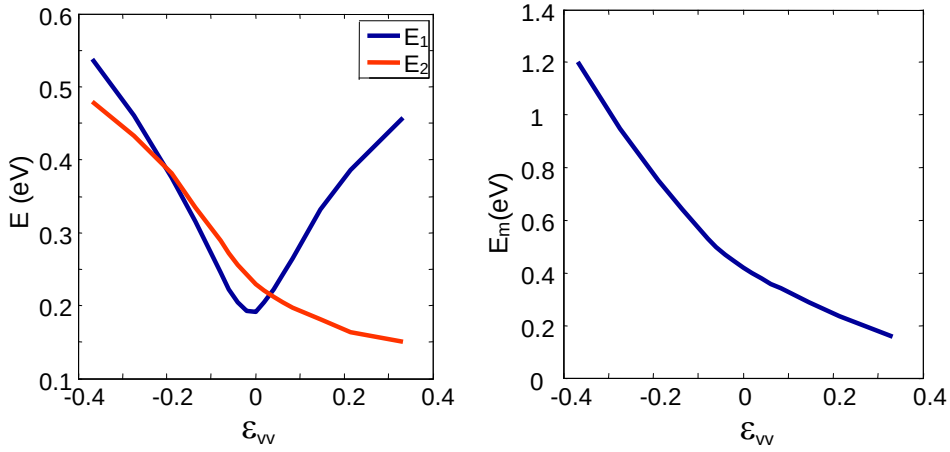


(a) (b)

Figure 2.5: QC-OFDFT calculations for aluminum (Gavini, 2008). (a) Di-vacancy binding energies versus macroscopic volumetric strain. (b) Migration energy versus macroscopic volumetric strain.

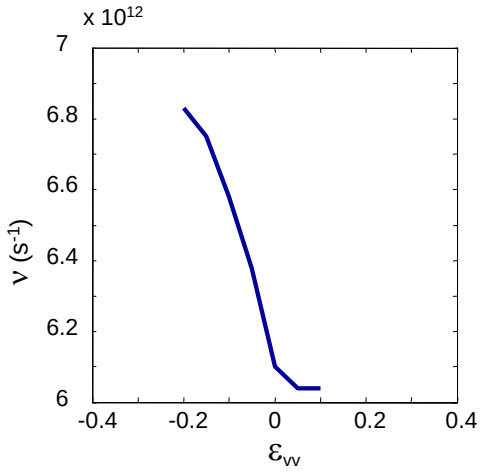


Figure 2.6: OFDFT calculations for aluminum (Ho et al., 2007). Jump frequency as a function of the volumetric deformation.

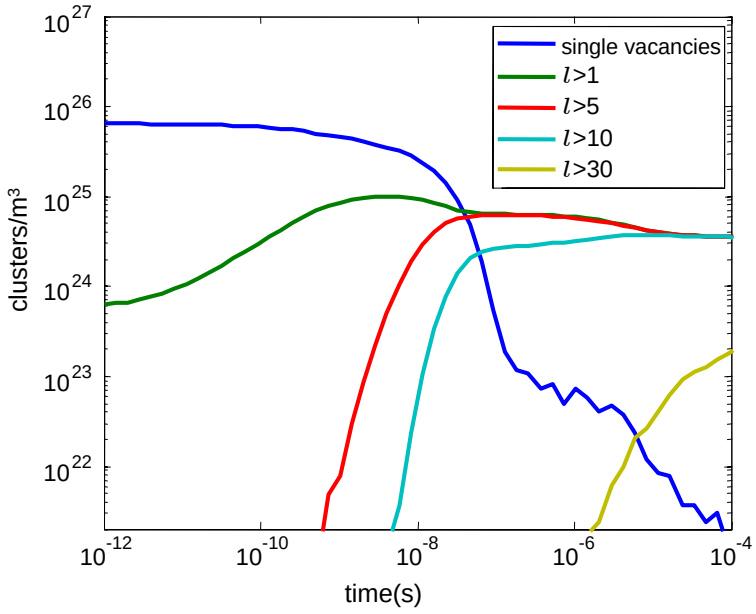


Figure 2.7: 118 nm cubic periodic cell of fcc aluminum ($\sim 10^8$ atoms) containing at 0.1% concentration ($\sim 10^5$ vacancies), $T = 728$ K, and $\varepsilon_{vv}= 0$.

## 2.5 Clustering kinetics

Of primary interest in the present study is the time evolution of vacancy-cluster statistics by size. In particular, the purpose is to ascertain whether nanovoids capable of cavitating plastically can be nucleated in sufficiently short times for the mechanism to operate under shock-loading conditions. A vacancy cluster is defined as a connected component of the graph defined by connecting first and second nearest-neighbor vacancies. In particular, a cluster of size $l$ is a cluster consisting of exactly $l$ vacancies. It is of note that this working definition of cluster is topological in nature and does not take the geometry of the cluster into account, e. g., whether the cluster is globular or linear.

The time evolution of cluster-size statistics in a 118 nm cubic periodic cell of fcc aluminum ($\sim 10^8$ atoms) at 0.1% concentration ($\sim 10^5$ vacancies), $T = 728$ K, and $\varepsilon_{vv} = 0$ is shown in Figs. 2.7 and 2.8. Nominally identical calculations over larger periodic cells using the parallel LKMC algorithm of Martinez et al. (2008) reveal that a periodic-cell size of 118 nm suffices to provide converged statistics. As expected from the attractive character of di-vacancy interactions, the cluster-size evolution exhibits an overall trend towards vacancy aggregation into clusters and a subsequent coarsening of the cluster

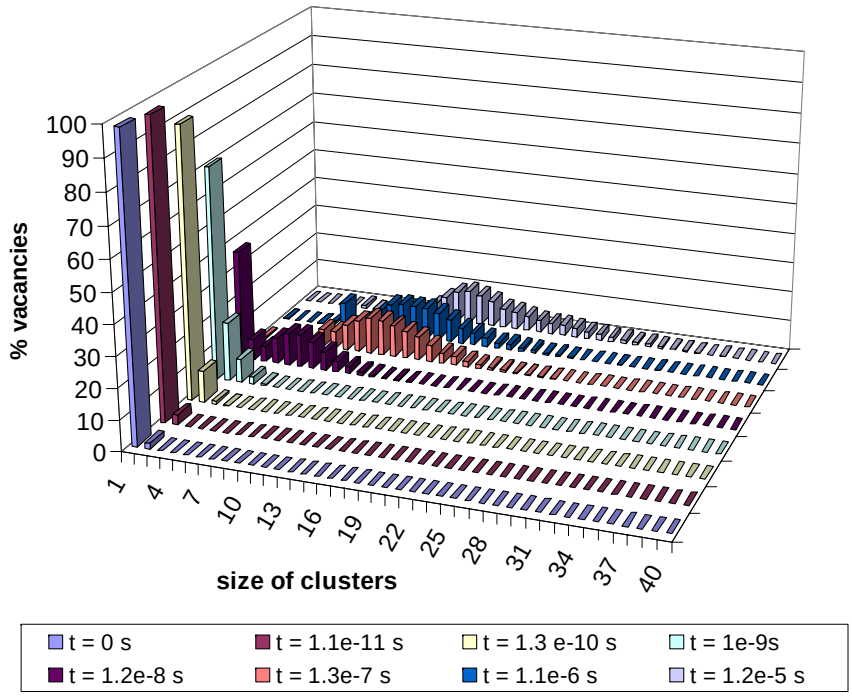


Figure 2.8: 118 nm cubic periodic cell of fcc aluminum ($\sim 10^8$ atoms) containing at 0.1% concentration ($\sim 10^5$ vacancies), $T = 728$ K, and $\varepsilon_{vv}$= 0. Evolution of histogram of cluster sizes.

distribution. Thus, clusters of a certain size appear after an incubation time and their densities initially grow at the expense of smaller clusters, later decreasing as even larger clusters become established. Predictably, the effect of increasing vacancy concentration is to decrease incubation times and accelerate the overall kinetics of aggregation and coarsening, as shown in Fig. 2.10.

The influence of volumetric strain and temperature on the evolution of cluster statistics up to 1 $\mu$s is shown in Fig. 2.9. As expected, temperature accelerates the kinetics, resulting in shorter incubation times and faster cluster coarsening. The net effect of positive volumetric strain (expansion) is also a marked acceleration of the kinetics. Thus, at 900 K, clusters of size 10 nucleate at $\sim 10^{-2}$ $\mu$s for a volumetric strain of $\varepsilon_{vv} = -0.13$, whereas the same clusters nucleate at around $\sim 10^{-4}$ $\mu$s for a volumetric strain of $\varepsilon_{vv} = 0.28$, or a two order-of-magnitude acceleration of the kinetics.

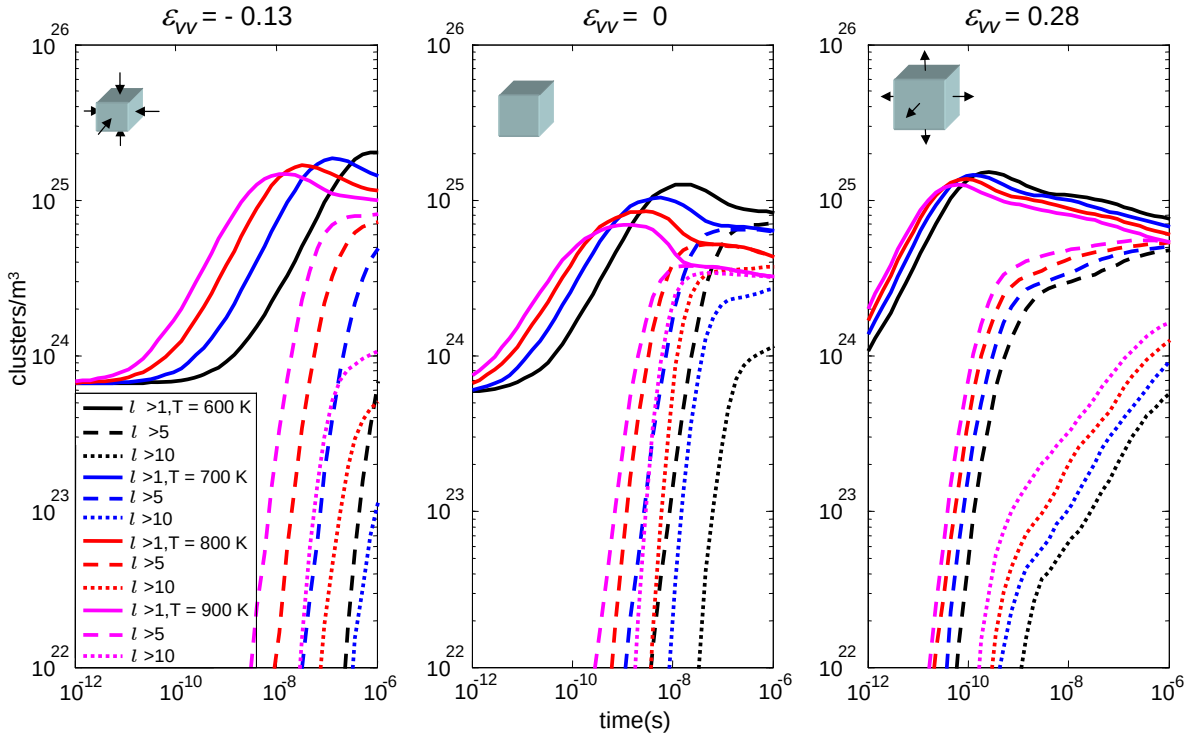


Figure 2.9: 100,000 vacancies at concentration of 0.1% ($10^8$ atoms). Influence of volumetric strain and temperature.

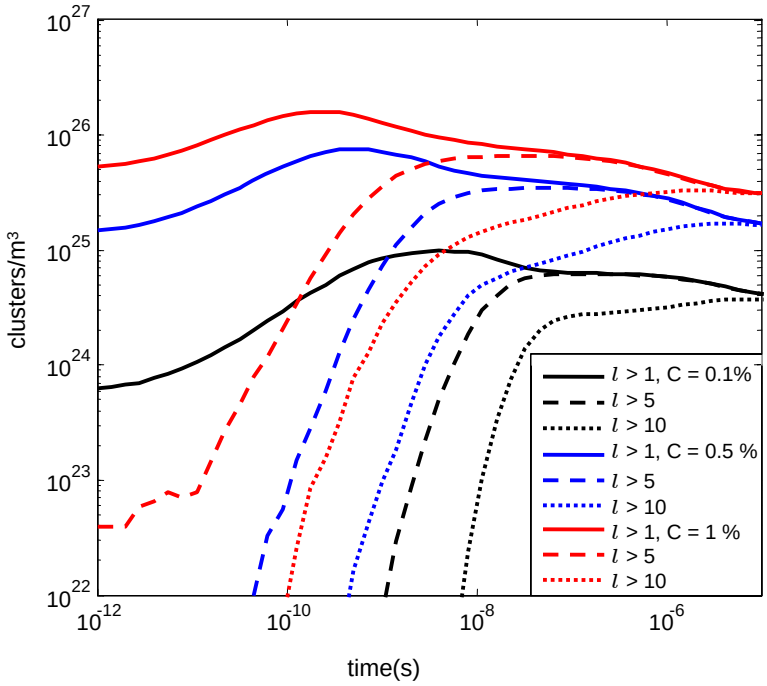


Figure 2.10: 100,000 vacancies. $T$= 728K, $\varepsilon_{vv}$= 0.

## 2.6 Application to spall fracture

The LKMC calculations summarized in the foregoing reveal that nanovoid nucleation by vacancy aggregation and cluster coarsening is sensitively dependent on both temperature and volumetric deformation. In particular, both temperature and volumetric expansion accelerate the kinetics markedly. Finally, the question of whether the mechanism is fast enough to operate under shock-loading conditions is addressed.

First, estimates of typical vacancy concentrations in aluminum at high temperatures and volumetric deformations in the range $T > 800$ K and $\varepsilon_{vv} > 0.075$ (Kanel et al., 2001, Dalton et al., 2007) are performed. The calculations of Gavini (2009a) show that, in this range of volumetric strains, the vacancy-formation energies are exceedingly small or even negative, which suggests that vacancies may be generated nearly spontaneously. This conclusion is in agreement with the molecular dynamics calculations of Strachan et al. (2001), who observed profuse cavitation in shocked metallic samples and showed that such cavitation may be understood as a critical phenomenon. In view of this observation, the vacancy concentration is assumed to be at or near its equilibrium value, neglecting other vacancy sources such as dislocation activity (Cuitino and Ortiz, 1996). Such value is determined by the minimum of the free energy. Two competing factors exist. The first one is related to the energy of formation of the vacancies $E_{fv}$, while the second factor is dependent on the configurational entropy of the system and can be approximated by the entropy of mixing between atoms and vacancies. The total free energy per atom as a function of defect concentration $c_v$ then reads (Porter and Easterling, 1981, Phillips, 2001)

$$A(c_v) = c_v(E_{fv} - T\Delta S_v) + kT\left[c_v \ln c_v + (1 - c_v)\ln(1 - c_v)\right] \tag{2.4}$$

where $\Delta S_v$ is the change in vibrational energy. A dilute approximation is made, both by presuming a value of the energy of formation that is independent of vacancy interactions and by neglecting any possible correlation in the position of the vacancies in the entropic term.

The resulting equilibrium concentration of vacancies is obtained through differentiation

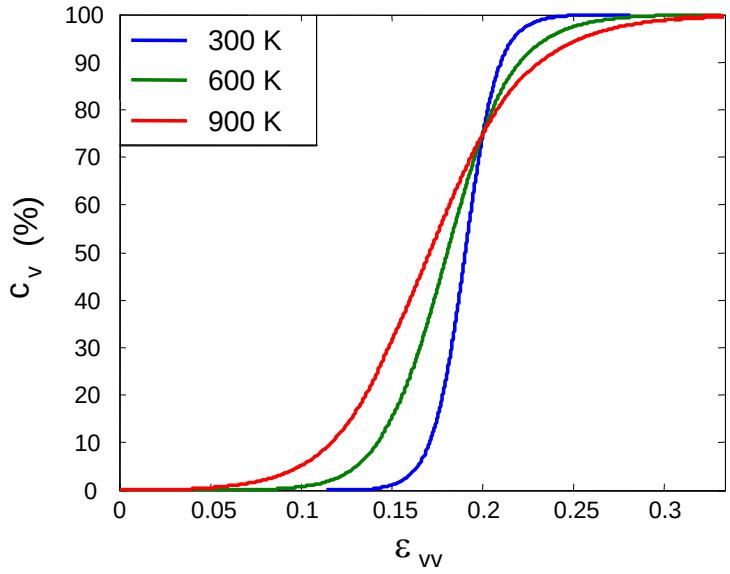


Figure 2.11: Equilibrium concentration of vacancies versus volumetric strain at different temperatures.

$(\partial A/\partial c_v = 0)$ resulting in

$$c_v = \frac{e^{\frac{\Delta S_v}{k_B}} e^{-\frac{\Delta E_{fv}}{k_B T}}}{1 + e^{\frac{\Delta S_v}{k_B}} e^{-\frac{\Delta E_{fv}}{k_B T}}} \tag{2.5}$$

By the assumptions made, this expression constitutes an estimate of the current concentration. The values of $E_{fv}$ computed by Gavini (2009a) as a function of volumetric deformation using QC-OFDFT are used in the calculations. In addition, $e^{\frac{\Delta S_v}{k_B}} \simeq 3$ is assumed (Porter and Easterling, 1981). Fig. 2.11 shows that the resulting equilibrium concentration of vacancies exhibits a sharp upturn in vacancy concentration at volumetric deformations of the order 0.2, at which the vacancy-formation energy becomes vanishingly small.

A nanovoid is said to have been nucleated when it attains the critical size at which it can emit dislocations and subsequently grow by dislocation-mediated plasticity. The process of dislocation emission from nanovoids has been studied by Marian et al. (2004, 2005) using quasi-continuum molecular statics. For purposes of the present discussion, a simple continuum estimate of the critical radius for plastic cavitation will suffice. To this end, a void with inner radius $a$ in an infinite medium expanding under an outer

tensile pressure $P$ is considered. The material is assumed to obey isotropic von Mises ideal elasto-plasticity. Under these assumptions, the critical radius $a_c$ for which yielding starts at a given pressure $P$ (see Section 2.6.1.1) follows from the relation

$$P = \frac{2}{3}\sigma_Y + \frac{2\gamma}{a_c} \tag{2.6}$$

where $\sigma_Y$ is the yield stress and $\gamma$ is the surface energy. In order to account for the temperature-dependence of the yield stress, a simple linear thermal-softening relation is assumed

$$\sigma_Y = \sigma_0 \frac{T - T_m}{T_0 - T_m} \tag{2.7}$$

where $\sigma_0$ is the yield stress at the reference temperature $T_0$, and $T_m$ is the melting temperature. Due to the small sizes of the voids at nucleation time, the attendant dislocation activity is confined to very small volumes. Under these conditions, the strength of the material may be expected to be greatly in excess of bulk macroscopic values. In order to account for this effect, a hardness law of the Hall-Petch type is assumed

$$\sigma_0 = C/\sqrt{a_c} \tag{2.8}$$

where the constant $C$ is calibrated so as to match the critical volumetric deformation computed by Marian et al. (2004). Similar scaling relations have been used elsewhere to describe nanoscopic plasticity, e.g., at the tip of a nanoindentor (Gao et al., 1999). In the calculations $\gamma = 0.98$ J/m$^2$ (Murr, 1975), $T_0 = 0$K, $C = 22.77$ GPa $\sqrt{\text{nm}}$ and $T_m = 933.5$K (Cardarelli, 2008) are used as being representative of aluminum.

In order to relate pressure to volumetric deformation and temperature a Mie-Grüneisen equation of state (e.g., Meyers (1994)) is used

$$P(\epsilon_{vv}, T) = P_{0K}(\epsilon_{vv}) - \frac{\bar{\gamma}}{V}\int_0^T C_v(T)\, dT \tag{2.9}$$

In particular, the $0K$ isotherm $P_{0K}(\epsilon_{vv})$ computed by Gavini (2009b) using QC-OFDFT

is adopted. It is further assumed (Meyers, 1994)

$$\frac{\bar{\gamma}}{V} \approx \frac{3\alpha}{Cv\ \kappa}\bigg|_{T=298.1K} \approx 2.232\ 10^{-5} \approx \text{constant} \tag{2.10}$$

The heat capacity $C_v$ at constant volume is assumed to depend solely on the temperature (see Fig. 2.12(a)). It is obtained via a $C_v - C_p$ relation (Giauque and Meads, 1941) and experimental values of the heat capacity at constant pressure $C_p$ (National Institute of Standards and Technology and Giauque and Meads (1941)). The resulting equation of state for aluminum at several values of the temperature is shown in Fig. 2.12(b).

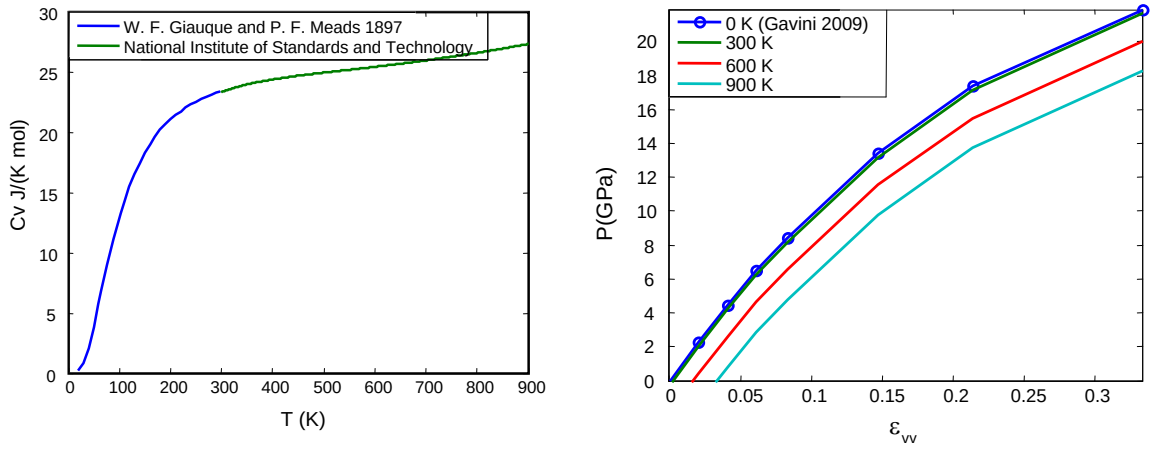


(a) (b)

Figure 2.12: (a) Heat capacity at constant pressure versus temperature. (b) 0 K equation of state extended to positive temperatures through a Mie-Grüneisen equation of state.

Fig. 2.13 shows the dependence of the critical cluster size $l_c$ on volumetric deformation and temperature predicted by the model just described. As may be seen from the figure, the critical cluster sizes become very small at high temperatures and tensile volumetric strains.

A combination of the plastic cavitation model and the LKMC simulations described in the foregoing finally enables the calculation of the times required for the nucleation of a critical nanovoid. The critical times thus predicted for aluminum are shown in Fig. 2.14. The remarkable conclusion afforded by the figure is that the critical nucleation times can be exceedingly small at high temperatures and tensile volumetric strains. In particular, such critical nucleation times are well within pulse duration times typical of plate-impact

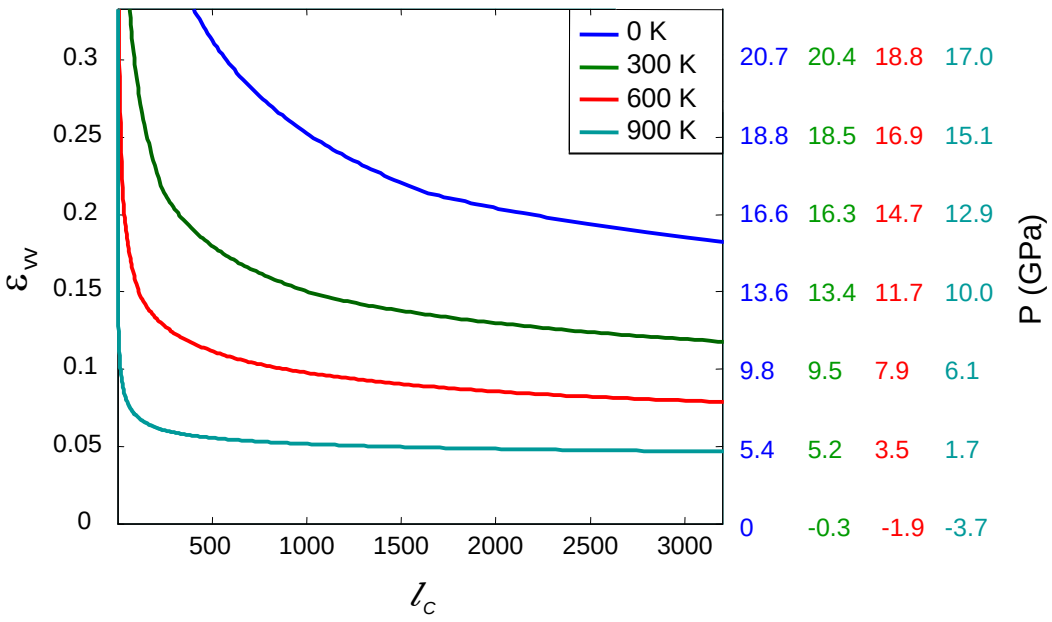


Figure 2.13: Critical cluster size in aluminum as a function of volumetric strain and temperature. The corresponding pressures at the different temperatures are indicated on the right ordinate axis.

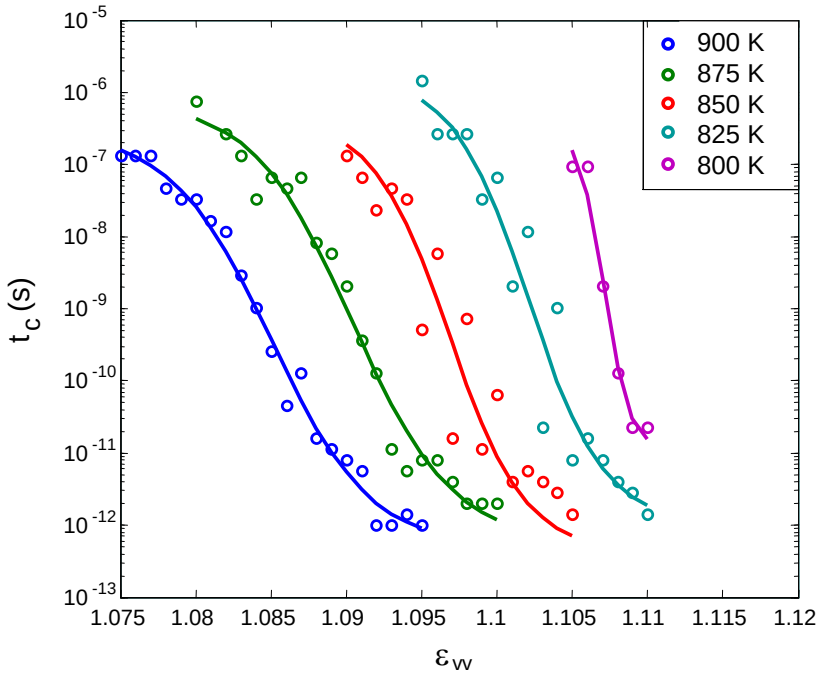


Figure 2.14: Time required for the formation of critical nanovoids capable of growing by dislocation-mediated plasticity as a function of the volumetric deformation and temperature. Solid lines represent tanh fits of the data.

experiments (Antoun et al., 2003), which establishes the feasibility of diffusion-mediated vacancy aggregation and subsequent vacancy cluster coarsening kinetics in high-purity metallic single crystals under conditions typical of, e.g., spall tests.

### 2.6.1 Critical pressure for plasticity induced void growth

In this subsection a preexistent spherical void of radius $a$ in an infinite medium is considered, and the required stress applied at infinity in order for plasticity to initiate at the surface of the cavity is computed. The theory of continuum mechanics is used in order to obtain such estimate.

Due to the spherical symmetry, the stresses obey the following equilibrium and compatibility equations in spherical coordinates

$$\begin{aligned} &\frac{d\sigma_{rr}}{dr} - \frac{2}{r}(\sigma_{\theta\theta} - \sigma_{rr}) = 0 \\ &\frac{d}{dr}(\sigma_{rr} + 2\sigma_{\theta\theta}) = 0 \end{aligned} \tag{2.11}$$

which have as general solution

$$\begin{aligned} \sigma_{rr} &= A + \frac{B}{r^3} \\ \sigma_{\theta\theta} &= A - \frac{B}{2r^3} \end{aligned} \tag{2.12}$$

$A$ and $B$ are constants to be determined by the boundary conditions. The stress imposed at infinity is $\sigma_{rr}(r \to \infty) = P$, while the effect of the surface energy $\gamma$ on the inner surface will be proven to be $\sigma_{rr}(r = a) = \frac{2\gamma}{a}$ in Section 2.6.1.1. The resulting stresses then are

$$\begin{aligned} \sigma_{rr} &= P\left(1 - \frac{a^3}{r^3}\right) + \frac{2\gamma}{a}\frac{a^3}{r^3} \\ \sigma_{\theta\theta} &= P\left(1 + \frac{a^3}{2r^3}\right) - \frac{\gamma}{a}\frac{a^3}{r^3} \end{aligned} \tag{2.13}$$

Applying the von Mises yield criterion, plasticity will occur in the inner surface when

$\sigma_{\theta\theta}(a) - \sigma_{rr}(a) = \sigma_Y$. Equivalently

$$P = \frac{2}{3}\sigma_Y + \frac{2\gamma}{a} \tag{2.14}$$

which is the desired relation.

#### 2.6.1.1 Pressure induced by the surface energy

In order to obtain the pressure at the surface of the cavity $\left(\sigma_{rr}(r=a) = \frac{2\gamma}{a}\right)$, the matrix surrounding the void is first assumed to be finite with radius $b$ and made of isotropic homogeneous material. The desired analytical result is then evaluated as the external radius and the stiffness of the material tend to infinity. A Hookean constitutive law with parameters $\lambda$ and $\mu$ is used

$$\begin{aligned}
\sigma_{rr} &= \lambda\left(\varepsilon_{rr} + \varepsilon_{\theta\theta} + \varepsilon_{\phi\phi}\right) + 2\mu\varepsilon_{rr} \\
\sigma_{\theta\theta} &= \sigma_{\phi\phi} = \lambda\left(\varepsilon_{rr} + \varepsilon_{\theta\theta} + \varepsilon_{\phi\phi}\right) + 2\mu\varepsilon_{\theta\theta}
\end{aligned} \tag{2.15}$$

where $\varepsilon_{rr} = \frac{du}{dr}$ and $\varepsilon_{\theta\theta} = \varepsilon_{\phi\phi} = \frac{u}{r}$ under spherical symmetry; $u(r)$ being the radial displacement.

The potential energy of the hollow sphere, assuming a surface energy $\gamma$ at the inner surface and a pressure $P$ on the outer surface, is

$$W(u) = \int_a^b 2\pi\left(\sigma_{rr}\varepsilon_{rr} + 2\sigma_{\theta\theta}\varepsilon_{\theta\theta}\right) r^2\, dr - 4\pi b^2 P u(b) + 4\pi\gamma\left(a + u(a)\right)^2 \tag{2.16}$$

By the principle of minimum potential energy, the solution needs to satisfy $\frac{dW(u+\epsilon\eta)}{d\epsilon}|_{\epsilon=0}$ for every admissible variation $\eta(r)$.

$$
\begin{aligned}
0 = \frac{\partial W}{\partial \epsilon}\Big|_{\epsilon=0} &= \int_a^b 2\pi r^2 \left[\sigma_{rr}(u)\varepsilon_{rr}(\eta) + 2\sigma_{\theta\theta}(u)\varepsilon_{\theta\theta}(\eta) + \sigma_{rr}(\eta)\varepsilon_{rr}(u) + 2\sigma_{\theta\theta}(\eta)\varepsilon_{\theta\theta}(u)\right] dr \\
&\quad - 4\pi b^2 P\eta(b) + 8\pi\gamma\left(a + u(a)\right)\eta(a) \\
&= \int_a^b 2\pi r^2 \left[2\sigma_{rr}(u)\frac{d\eta}{dr} + 4\sigma_{\theta\theta}(u)\frac{\eta}{r}\right] dr \\
&\quad - 4\pi b^2 P\eta(b) + 8\pi\gamma\left(a + u(a)\right)\eta(a) \\
&= -\int_a^b 4\pi r^2 \left[\frac{d\sigma_{rr}}{dr} + \frac{2}{r}(\sigma_{rr} - \sigma_{\theta\theta})\right]\eta \\
&\quad + 4\pi b^2\left(\sigma_{rr}(b) - P\right)\eta(b) - 4\pi a^2\sigma_{rr}(a)\eta(a) + 8\pi\gamma\left(a + u(a)\right)\eta(a)
\end{aligned}
\tag{2.17}
$$

The equilibrium equation and the boundary conditions are recovered.

$$
\begin{aligned}
&\frac{d\sigma_{rr}}{dr} + \frac{2}{r}(\sigma_{rr} - \sigma_{\theta\theta}) = 0, \quad a < r < b \\
&\sigma_{rr}(b) = P \\
&\sigma_{rr}(a) = 2\gamma\frac{a + u(a)}{a^2}
\end{aligned}
\tag{2.18}
$$

In the limit of a rigid material, the inner boundary condition can be simplified to

$$
\sigma_{rr}(a) = \frac{2\gamma}{a} \tag{2.19}
$$

and the sought-after result is obtained. This pressure difference emanating from a curved surface characterized by a surface energy is very well known in fluids and the same relation holds for solids.

## 2.7 Notes on the numerical implementation of the serial code

In this section a few details concerning the implementation of the serial code are provided. Special attention is given to the memory allocation, which was designed for a fast update

of the stored information after each Monte Carlo step. As has been mentioned throughout the chapter, the code aims to follow the position of a given number of vacancies in an fcc lattice using a kinetic Monte Carlo algorithm with an Ising Hamiltonian that considers first and second nearest-neighbor interactions. The domain of the simulation is a periodic cubic cell of side $n_{\text{side}}$ and the coordinate system is chosen to have its origin at one of its corners with the axes oriented along the sides of the cubic domain. The side of a unit cube representative of the fcc structure is taken to be of size 2, so that the positions of the vacancies can always be determined by a triplet of integers. It is of note that the sum of the coordinates of each vacancy needs to be even for a position to be plausible. An odd value of this sum corresponds to the center of a unit cube in the lattice, which cannot be occupied by any atom in an fcc structure.

In view of the low concentrations that are simulated, a sparse representation is used to store the vacancy positions. This reduces the size of the data stored in the memory, but obviously adds complications to the task of finding the neighboring entities. Memory structures were designed for storing the information in a way that is advantageous for the search process. It consists of 3 independent matrices, called $X$, $Y$ and $Z$, of length equal to the number of vacancies and with width 4, 2 and 2 respectively. The first column of each of these matrices contains the $x$, $y$ and $z$ coordinates of the vacancies in increasing order. A given row of the three matrices therefore corresponds, in general, to three different vacancies. The second column of matrices $Y$ and $Z$ indicate the index of the row in $X$ associated to the same vacancy and the second and third column of $X$ contain the indices of the rows in $Y$ and $Z$ of the corresponding vacancy. Finally, the last column of $X$ contains a pointer, where other information about the vacancy, such as neighbors or rates of the possible jumps are stored. As an example to illustrate the structures just described, the following four vacancies are stored in such a manner: $(1, 5, 8)$, $(7, 2, 4)$, $(4, 4, 6)$ and $(3, 5, 1)$. The resulting matrices are

| | X | | | | Y | | Z | |
|---|---|---|---|---|---|---|---|---|
| | $x_{\text{coord}}$ | $j_{\text{index}}$ | $k_{\text{index}}$ | vacancies | $y_{\text{coord}}$ | $i_{\text{index}}$ | $z_{\text{coord}}$ | $i_{\text{index}}$ |
| 0 | 1 | 2 | 3 | $p_1$ | 2 | 3 | 1 | 1 |
| 1 | 3 | 3 | 0 | $p_2$ | 4 | 2 | 4 | 3 |
| 2 | 4 | 1 | 2 | $p_3$ | 5 | 0 | 6 | 2 |
| 3 | 7 | 0 | 1 | $p_4$ | 5 | 1 | 8 | 0 |

where $p_i$ are the pointers to the vacancy structures. As will be seen, this structure proves to be advantageous for the neighbor search and the update of the position of the vacancies after each Monte Carlo step.

The code starts with the following sequence of initialization steps

1 Reading from an input file the initial configuration of vacancies to be analyzed and storage of their position in the matrices previously described.

2 Calculation of the rates of all possible motions for the given volumetric deformation and temperature. There are 12 nearest-neighbors and 6 second nearest-neighbors in an fcc structure, which leads to at most $25 \times 13$ different rates, stored in a matrix data structure. Position $(i, j)$ in the matrix ($i \in [0, 24], j \in [0, 12]$) corresponds to a change of $\Delta n_1 = i - 12$ and $\Delta n_2 = j - 6$ in number of first nearest-neighbors and second nearest-neighbors respectively. Some of the rates correspond to impossible situations, but are left in the matrix for simplicity.

3 Initial neighbor search. Each vacancy structure contains an array (of total size 78) with pointers to the 18 first and second nearest-neighbors and the remaining 60 first and second nearest-neighbors of the first nearest-neighbors not previously included. If a position is not occupied by a vacancy, a null pointer is stored. The neighbors can easily be found by examination of the entries below and above the vacancy in question in matrix $X$. Only vacancies for which the difference in the $x_{\text{coord}}$ is less or equal than 3 are possible neighbors. The actual coordinates indicate the type of neighbor and its relative position. As can be seen in the example of the storage structure, it is possible to have several vacancies with a common coordinate. For randomly generated vacancies, there are on average $\frac{N}{n_{\text{side}}}$ vacancies per coordinate. For the case of $N = 10000$ vacancies and a concentration of 2%,

there are 500000 atoms. Each unitary cube nominally contains 4 full atoms (8 on the corners, shared between 8 cubes each, and 6 on the centers of the faces, shared between two cubes each), which indicates that the domain is composed of 125000 of such unitary cells, 50 per side and $n_{\text{side}} = 100$. In this example, there are then 100 vacancies with a same given coordinate . In general, for a given concentration $C$, $\frac{N}{n_{\text{side}}} = \frac{C(\frac{n_{\text{side}}}{2})^3 4}{n_{\text{side}}} = \frac{C}{2} n_{\text{side}}^2$. Therefore the algorithm of neighbors search becomes slower as the size of the system is increased at a constant concentration of vacancies. This is due to the fact that the proposed method is based in an orthogonal range search over the projection of the coordinates in a given plane. If larger systems are to be solved, search trees algorithms would be advantageous with respect to the procedure just described.

4 Initial rate calculation. Additionally, each vacancy structure contains an array of size 12 with the rates of its 12 possible movements. If a first nearest-neighbor is occupied by a vacancy, the rate corresponding to the associated movement is taken to be zero. The rates are computed according to Eq. 2.4, where $\Delta E = \Delta n_1 E_1 + \Delta n_2 E_2$. The values of $\Delta n_1$ and $\Delta n_2$ can easily be computed from the neighbor information obtained in the previous step. In the notation used, $\Delta n > 0$ indicates an increase of the number of atoms surrounding the vacancy if a given movement is considered. This indicates that the vacancy is moving away from a cluster of vacancies and therefore there is an increase in the energy barrier.

5 Computation of the rate histogram and total rate. The number of events with a given rate are stored in increasing rate order so as to accurately compute the total maximum rate. Numerical errors occurred if an unordered sum of the individual rates is performed.

6 Cluster computation. Each vacancy contains the pointer to the cluster it belongs to, and each cluster structure contains the pointers of the vacancies that composes that cluster. The storage of the cluster information is organized in double linked lists, where each list corresponds to clusters of the same number of vacancies. The first cluster of each list is stored in an array of clusters. The first element of the array is a pointer to the first cluster of the list of clusters of 2 vacancies (if they exist, a 0

otherwise); the second element, is a pointer to the first cluster of the list of clusters of 3 vacancies, and so on. The size of this array can be increased dynamically if necessary. Since the number of clusters of all sizes tends to increase monotonically, the size of the array is never decreased. The algorithm for the cluster search is done in the following manner

6.1 Initialization of cluster pointer of every vacancy to zero; the variable containing the number of single vacancies is set to 0.

6.2 The first time the clusters are computed, their size is going to vary very often. Therefore, first, a simple linked list of clusters is used, where all the clusters are in the same unordered list independently of their size. For each vacancy:

6.2.1 If the vacancy has not had a cluster assigned to it (pointer to the cluster still at zero)

- If it does not have any neighboring vacancies then it is isolated, and the number of single variables is increased.
- If it does have neighbors and they do not have any cluster assigned yet, a new cluster is created and the vacancy and all its neighbors are included.
- If a neighbor belongs to a cluster, the vacancy is added to that cluster, as well as all the other neighbors that did not have a cluster.

6.2.2 If the vacancy has a cluster assigned, the first and second nearest-neighbors that do not have a cluster are added to the cluster. If one of the neighboring vacancies belongs to a different cluster, the big cluster is made to contain the small one, and the number of vacancies contained in the small one is set to zero.

6.3 If a cluster has size zero, nothing needs to be done, since it is the same as if it did not exist. Otherwise, geometrical information such as the cluster's center of mass and scalar moment of inertia can be computed. These magnitudes need to be calculated carefully due to the existence of the periodic boundary conditions. The center of mass is therefore not the simple arithmetic average of the positions of the vacancies contained in the cluster. The center of mass

is calculated with respect to the first vacancy of the cluster, from which the absolute position of the center of mass is then inferred. It has been assumed that there is no percolation of clusters and that the size of the clusters in any direction is smaller than half of the side of the cubic domain, so that the distance between vacancies can be computed from their coordinates and without needing to examine their connectivities.

Once this initialization has been performed, each Monte Carlo step consists of the following

1 Selection of the event that is going to be carried out. A binary tree is used to select the corresponding rate.

2 Update the matrices $X$, $Y$, and $Z$ according to the movement of the vacancy. When a vacancy moves, two of its coordinates are increased or decreased by a value of 1. As will be explained, each of these simple processes involves at most, the exchange of two rows in the matrices $X$, $Y$ or $Z$, resulting in a fast update. The 6 possible cases are summarized in the table below

| | |
|---|---|
| 0 | y++ |
| 1 | x++ |
| 2 | y– – |
| 3 | x– – |
| 4 | z++ |
| 5 | z– – |

Cases 0, representative of cases 0, 2 and 4, and case 1, equivalent to case 5, are summarized

Case 0:

The first step consists on checking the $y$ coordinate in the next element of the array $y_{\text{coord}}$ of the structure $Y$. If a difference in the values is encountered, the update simply consists of increasing the value of the $y$ coordinate of the moving vacancy. In case that the two $y$ coordinates are equal, the last element with the same $y$ coordinate is identified and the two rows in the structure $Y$ are then exchanged.

The corresponding value of $j_{\text{index}}$ in the structure $X$ needs to be updated as well. Due to the boundary conditions, the matrices need to be looked at as cyclic, and the end of the array is followed by the first element of the array. A flag can be included for the improbable situation in which all the vacancies are aligned, so as to avoid an infinite loop.

Case 1:

This case is similar to the previous one. If the next position in the array $x_{\text{coord}}$ is the same as the current $x$ coordinate (otherwise the update simply consists of changing its value), the last element with the same value is searched for. The two rows of the structure $X$ are then interchanged and the corresponding elements of the array $i_{\text{index}}$ of the structures $Y$ and $Z$ are updated.

3 Update of the neighbors information of the neighbors of the moving vacancy. This task can be performed efficiently with the stored neighbor information of each vacancy.

4 Calculation of the new neighbors of the vacancy that has moved. This is done in a manner very similar to the initial neighbor search.

5 Update of the rate of the moved vacancy and its old and new neighbors. Update as well the rate list and total rate.

6 Cluster information update. When a vacancy that belonged to a cluster moves, the cluster can become bigger, get separated into two or more clusters or remain the same. In order to take all these possibilities into account, the cluster pointer of all the vacancies in such cluster is set to zero, the old cluster is deleted and the number of single vacancies is increased. For these vacancies, the cluster search is performed in a similar manner to the initialization stage. As the clusters are now ordered, the new clusters need to be positioned in the appropriate location. When a vacancy forms part of a cluster, the number of single vacancies is decreased. Also, if a cluster has changed, its geometrical information needs to be updated.

7 Update time.

# Chapter 3

# Material response under void damage

In this chapter a self-consistent micromechanical model for void growth based on a representative volume element is developed. The first section is dedicated to reviewing existing models based on the response at the microscopic level. Two other approaches can be found in the literature, although they will not be followed in this study. The first one, more phenomenological, sits in the theory of continuum damage mechanics and is based on internal variables that evolve according to the thermodynamics of irreversible processes (Pineau, 1982, Germain et al., 1983, Lemaitre, 1986, Rousselier, 1987, Pineau, 2006). The second approach is based on variational bounds for nonlinear composites (Castañeda and Zaidman, 1994, Castañeda and Suquet, 1998).

As will be discussed in the following, most of the previously proposed micromechanical models for porous materials are based on representative volumes, such as a hollow sphere or a matrix with a periodic distribution of voids. The relation to the macroscopic behavior is then established through the introduction of simplifying assumptions, required to obtain tractable analytic solutions. The resulting models are often complemented with additional parameters that require fitting to experimental results.

Thanks to growing computing capabilities, a recent trend has emerged where multi-scale finite element simulations are performed with resolution of several scales (see for instance Smit et al. (1998) in the context of voided materials). One of the goals of this type of effort is to root the macroscopic behavior directly in models that sit at a lower scale, and ultimately derive the overall behavior uniquely from fundamental physics and no experimental inputs. This is very appealing from a scientific understanding point of

view as well as for its application as a design tool. Further, one of the most important applications lies in the prediction of fracture initiation. Full simultaneous resolution of the lower scales produces quantitative information on the local deviations, which cannot be derived from the average values used at the scale immediately above them in the hierarchy. These deviations could correspond, for instance, to local stress concentrations due to heterogeneities that can initiate failure at the microscopic level, and then evolve into macroscopic damage and final failure of the system. Without resolution of the lower scales, such deviations cannot be captured in the simulations. The stochastic character of the lower scales could also allow us to recover the statistical aspects of fracture by a bottom-up approach.

In this work, a consistent two-level model is developed to define the behavior of porous media under general loading conditions, including dynamics. A classical representative volume element (RVE) consisting of a single hollow sphere is chosen to characterize the lower scale governed by damage in the form of voids. Results from this heterogeneous scale, termed "microscopic", are then suitably averaged to provide the so called "macroscopic" behavior of the material, which is treated as homogeneous. The connection between the two scales is based on the fact that some averaged quantities depend exclusively on the values of the corresponding microscopic field at the boundary of the RVE. These quantities therefore set a basis for defining a boundary value problem at the microscopic level that is physically meaningful. This is well understood for the static case, both in infinitesimal strains and finite kinematic framework (Hill, 1963, 1967, 1972, Ogden, 1974, Nemat-Nasser, 1999), where the governing balance equations are seen to be the same at both scales. Less information is found in the literature concerning the dynamic case (Molinari and Mercier, 2001, Wang and Sun, 2002), especially under large strains. In Section 3.2 and 3.3 the choice of the RVE, together with the appropriate definition of the boundary conditions and macro variables, is discussed. In particular, the well known averaging results under static conditions are revisited from a variational perspective, providing the necessary abstraction for obtaining analogous results under dynamic conditions. The results here obtained are not limited to the case of a hollow sphere as a choice of the RVE. The range of applications is very wide and extends to other heterogeneous media such as composites or polycrystals. As will be discussed in Section 3.4, the variational

structure of the resulting multiscale model also provides a basis for the time discretization.

The spatial discretization needed to numerically resolve the solution is treated in Section 3.5. An approximation space based on spherical harmonics is employed so as to preserve the rotational symmetries of the problem. This basis is also capable of representing the fields on the domain with far fewer degrees of freedom than more standard finite element discretizations. The potential difficulties arising from the boundary conditions and the spatial integration scheme to be used are also addressed in detail. As will be shown, the boundary conditions can be represented in an exact and explicit fashion, and a quadrature rule is proposed that provides exact integration of the stiffness matrix, mass matrix and void volume fraction.

Numerical verifications are performed in Section 3.6. Several analytical solutions of the elastic deformation of the hollow sphere under static conditions are found. Convergence analysis for these simple cases, and for other more general ones, show a close to ideal convergence rate for linear and nonlinear materials in elastic and plastic regimes undergoing general deformations.

The following section is dedicated to material point calculations. The damage resulting from the presence of voids is discussed for a wide variety of materials and loading conditions. Some comparisons with previous and well established models are also performed.

This chapter concludes with Section 3.8, where the applicability of developed model is demonstrated with a complete multiscale simulation ($FE^2$) and some comparisons to experimental results.

## 3.1 Previous micromechanical models of void growth

Pioneering micromechanical studies of void growth were performed in the late 1960's by McClintock (1968) and Rice and Tracey (1969). They analyzed the growth of preexistent cylindrical and spherical cavities, respectively, in an infinite plastic medium. In both studies, an exponential growth of the void is observed as a function of the stress triaxiality[1], when such measure of stress is high.

[1]The stress triaxiality is defined as $\sigma_m/\sigma_e$ with $\sigma_m = \sigma_{kk}/3$ being the mean stress, $\sigma_e = \sqrt{3 s_{ij} s_{ij}/2}$ the effective stress and $s_{ij}$ the deviatoric part of the stress tensor.

These theoretical investigations were compared to experimental observations by Marini et al. (1985). The exponential dependence of the void growth on the stress triaxiality was confirmed by the experiments, although the theoretical studies seemed to underestimate the void growth, especially at large values of the void volume fraction.

The effect of the void volume fraction was first included analytically in the macroscopic behavior by Gurson (1977a), leading to what has been the most popular porous material model so far. Gurson obtained an upper bound approximation of the yield function for porous materials based on the response of a hollow sphere (or hollow cylinder) under a macroscopic deformation rate imposed on the outer boundary. The matrix material containing the void was assumed to be a homogeneous rigid perfectly plastic material obeying the von Mises yield criterion. By making use of approximate forms of the velocity field and upper bound inequalities of the macroscopic stresses, Gurson then obtained analytic formulas that approximated the yield locus. For the more realistic case of a hollow sphere the expression found for the yield surface was

$$\Phi(\sigma_{ij}, \sigma_Y, f) = \left(\frac{\sigma_e}{\sigma_Y}\right)^2 + 2f\cosh\left(\frac{3}{2}\frac{\sigma_m}{\sigma_Y}\right) - 1 - f^2 = 0 \tag{3.1}$$

where $\sigma_{ij}$ is the macroscopic stress tensor, $\sigma_e = (s_{ij}s_{ij})^{1/2}$ is the Mises equivalent macroscopic stress, $s_{ij} = \sigma_{ij} - \sigma_m\delta_{ij} = \sigma_{ij} - \frac{\sigma_{kk}}{3}\delta_{ij}$ is the deviatoric part of the stress tensor, $\sigma_Y$ is the yield stress of the matrix material containing the voids, and $f$ is the void volume fraction.

The resulting yield surface is represented in Fig. 3.1 for different values of the void volume fraction. As can be noted in the figure, the yield function reduces to the von Mises criterion ($J2$ flow theory) when the void volume fraction vanishes, and shrinks to the origin as the void volume fraction increases towards unity.

The model is completed with a normal flow rule and an evolution law for the void volume fraction. Gurson (1977b) showed that normality of the plastic flow rule for the matrix material leads to macroscopic normality, and therefore, the plastic strain rate tensor can be determined as follows

$$\dot{\varepsilon}_p = \Lambda\frac{\partial\Phi}{\partial\sigma} \tag{3.2}$$

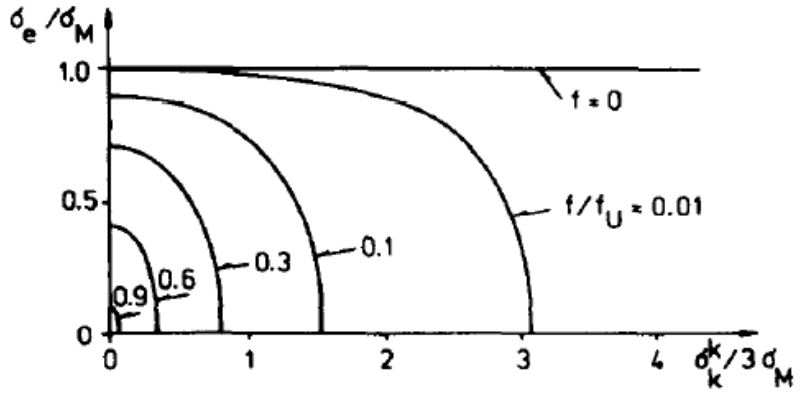


Figure 3.1: Yield function as a function of the hydrostatic stress for several values of the void volume fraction. (Tvergaard, 1982)

where the yield function is used as plastic potential and $\Lambda$ is a proportionality factor that can be determined by the equivalence of macroscopic and microscopic plastic work.

The rate of growth of the void is decomposed by Gurson (1977b) into the contribution due to nucleation of new voids and the contribution due to growth of existing voids

$$\dot{f} = (\dot{f})_{\text{nucleation}} + (\dot{f})_{\text{growth}} \tag{3.3}$$

The change in porosity due to void growth, by mass conservation and plastic incompressibility of the matrix, can be expressed as a function of the volumetric component of the macroscopic plastic strain rate

$$(\dot{f})_{growth} = (1 - f)\dot{\varepsilon}_{pkk} \tag{3.4}$$

Gurson's criterion was derived from a single spherical void, and therefore the interaction between voids and coalescence was neglected by the model. Such interaction was first studied numerically by Neddleman (1972) and Tvergaard (1981a) using a doubly periodic square array of circular cylindrical holes in an elastic-plastic material. It was then included into Gurson's model in a rather phenomenological manner by Tvergaard (1981a) and Tvergaard and Needleman (1984). A complete presentation of the model, usually called the GTN model, can be found in Tvergaard (1990). The modified yield

condition is

$$\Phi(\sigma_{ij}, \sigma_Y, f) = \left(\frac{\sigma_e}{\sigma_Y}\right)^2 + 2q_1 f^* \cosh\left(\frac{3q_2}{2}\frac{\sigma_m}{\sigma_Y}\right) - [1 + (q_1 f^*)^2] = 0 \tag{3.5}$$

It is of note that the model reduces to the original Gurson model when $q_1 = q_2 = 1$ and $f^*(f) = f$. The constants $q_1$ and $q_2$ were introduced in order to give a better approximation to experimental results or numerical computations of periodic distribution of voids. The values $q_1 = 1.5$ and $q_2 = 1.0$ are often used, although many different values can be found in the literature. As already indicated by the authors (Tvergaard, 1981a), these parameters seem to be material dependent. Faleskog et al. (1998) related them to the plastic hardening exponent and the ratio of yield stress over the Young's modulus.

The function $f^*(f)$ was introduced by Tvergaard and Needleman (1984) in order to account for the effect of coalescence. According to Eq. 3.1 (see also Fig. 3.1), the material loses its load carrying capacity when the void volume fraction reaches the value of unity, which is unrealistic. Experimental observations (Brown and Embury, 1973, Goods and Brown, 1979) show that coalescence occurs approximately when the spacing between voids is approximately equal to their size at a void volume fraction of the order of $f = 0.15$, which is far below unity. The function $f^*(f)$ was chosen to be equal to the void volume fraction until a critical void volume fraction $f_c$ is reached, after which the damage process is accelerated.

$$f^*(f) = \begin{cases} f, & \text{for} f \leq f_c, \\ f_c - \frac{f_U^* - f_c}{f_F - f_c}(f - f_c), & \text{for} f > f_c, \end{cases}$$

$f_F$ is the void volume fraction at fracture and $f_U^* = f^*(f_F) = 1/q_1$. Values of $f_c = 0.15$ and $f_F = 0.25$ were chosen by the authors based on comparison with experiments (Brown and Embury, 1973). The value of $f_c$ can also be determined from unit cell calculations (Zhang et al., 2000).

The GTN model has been proven to be very successful in many applications, although it suffers from several limitations, as can be seen from the fact that the parameters involved in the model do not have a fixed value. These limitations include, among others, the lack of representation of strain hardening, kinematic hardening, strain rate sensitivity, plastic anisotropy, void shape effects or evolution of damage under shear. This has motivated

further improvements of the model, detailed in the following subsections.

### 3.1.1 Strain hardening and kinematic hardening

Good prediction of plastic instabilities cannot be achieved with classic $J2$ flow theory due to the low curvature of the yield surface (Hutchinson and Tvergaard, 1981). This is especially true for materials with high strain hardening. Better approximations can be achieved by considering kinematic hardening into the model, which increases the curvature of the flow potential surface and accelerates the occurrence of failure (Tvergaard, 1978).

In the case of porous ductile materials, Mear and Hutchinson (1985) developed a dilatant plasticity model that has as two limiting cases Gurson's isotropic hardening model and a pure kinematic hardening model, both coinciding for proportional loading histories[2]. Mear and Hutchinson performed numerical flow localization experiments using their model and obtained, similarly to nonporous materials, a high sensitivity of the strains at localization with the curvature of the yield surface.

Their model was subsequently extended by Tvergaard (1987) to account for void nucleation, and by Becker and Needleman (1986) to introduce strain rate dependency.

Other extensions that include kinematic hardening in addition to strain hardening to the porous media have been proposed by Leblond et al. (1995). FE calculations show that kinematic hardening accelerates the occurrence of failure.

### 3.1.2 Strain rate sensitivity

The micromechanics underlying the GTN model assume that the matrix containing the voids in a porous material is rigid perfectly plastic, without accounting for rate dependency of the material behavior. Similar to Rice and Tracey (1969), Budiansky et al. (1982) performed micromechanical studies of an initial spherical void in an infinite medium of isotropic incompressible viscous material with an arbitrary hardening exponent under remote axisymmetric loading. The void growth rate obtained reduces to the formula provided by Rice and Tracey (1969) for the case of rigid perfectly plastic solid and high triaxiality. Based on these results, Duva and Hutchinson (1984) formulated a potential

[2]Proportional stressing implies no rotation of the principal axis and proportional increase of the principal stresses.

function for a matrix material containing a dilute concentration of voids.

Other interesting approaches have been proposed by Michel and Suquet (1992) based on variational bounds applied to a viscous material matrix containing several voids. The potential resulting from their formulation has a quadratic form.

Another model that takes into account strain rate sensitivity is the one developed by Leblond et al. (1994). It has as two limiting cases the GTN model for the case of an ideal plastic behavior (strain rate hardening exponent $n = \infty$) and a quadratic form of the stress tensor in the case of a linear Newtonian viscous material ($n = 1$).

Other authors have maintained Gurson's potential and account for strain rate sensitivity by representing the inelastic part of the deformation in terms of a nonlinear viscous behavior. Pan et al. (1983) have used such an approach to study localization of the deformation, finding that rate sensitivity has a retarding effect on the localization.

### 3.1.3 Void shape anisotropy

One of the major limitations of the Gurson model is that it is based on the growth of a spherical cavity that remains spherical throughout the loading history. However, experiments show that under low values of the stress triaxiality voids tend to become elongated. Also, manufacturing processes such as rolling can lead to initially anisotropic inclusions.

Similar to the investigations of Rice and Tracey (1969) and Budiansky et al. (1982), Lee and Mear (1992) studied an ellipsoidal cavity in an infinite plastic or viscoplastic medium; and parallel to the work of Gurson, Gologanu et al. (1993, 1994) developed a macroscopic yield criterion based on an ellipsoidal void located inside a confocal matrix loaded axisymmetrically (prolate and oblate configuration). The resulting yield surface introduces an additional parameter that accounts for the void shape. An evolution law for the shape parameter is also provided.

Models proposed by Castañeda and Zaidman (1994), Kailasam and Castañeda (1998), Kailasam et al. (2000) consider 3D ellipsoidal pores (not limited to axisymmetric cavities) and pore orientation. However, the formalism employed is more suitable for linear viscous solids than for plastic solids (Besson, 2010).

### 3.1.4 Plastic anisotropy

Anisotropy in a metal can arise as a result of forming. Its influence on void growth and material failure has been observed experimentally (Hancock and Mackenzie, 1976). Also, anisotropy is expected to influence plastic localization (Steinmann et al., 1994).

Plastic anisotropy of the matrix containing the voids has an effect on the effective constitutive relation and the damage evolution law. Benzerga and Besson (2001) have derived an upper bound of the yield surface in a manner similar to Gurson. The matrix material in this case is assumed to be rigid perfectly plastic, obeying Hill's yield criterion, and the load is assumed to be triaxial and aligned with the material symmetry axis. The obtained yield surface is identical to the one developed by Gurson, with the difference that the von Mises equivalent stress in Eq. 3.1 is replaced by Hill's equivalent stress (Hill, 1948).

$$\sigma_H = \sqrt{\frac{3}{2} s : H : s} \tag{3.6}$$

where $s$ is the stress deviator and $H$ the Hill anisotropic fourth-order tensor.

The evolution law for the void volume fraction provided is similar to the one proposed by Gurson. It depends on the anisotropy of the material, although the damage parameter remains a scalar, and therefore isotropic damage is assumed.

The work of Gologanu et al. (1993) has also been recently extended to account for anisotropy by Monchiet et al. (2008).

### 3.1.5 Influence of shear on damage evolution

The single damage parameter in the GTN model is the void volume fraction. Its evolution law, neglecting nucleation, only considers the volumetric component of the strain. Therefore, no damage evolution is predicted by the model in the case of pure shear, under zero stress triaxiality. This is in contrast to experiments (Barsoum and Faleskog, 2007a) where fracture is shown to be susceptible to voids at low stress triaxiality. Bao and Wierzbicki (2004) have also shown a non-monotonic behavior of the effective plastic strain at fracture as a function of stress triaxiality. On the numerical and theoretical side, micromechanical studies (Zhang et al., 2001, Kim et al., 2004, Barsoum and Faleskog, 2007b, Gao and

Kim, 2006) have confirmed the insufficiency of the stress triaxiality to study the damage evolution. Most of these analyses use the Lode parameter[3] as a second measure of stress.

In order to overcome this limitation of the GTN model, Xue (2007) proposed a new damage plasticity model. It is a completely phenomenological model in which the evolution law of the damage variable depends both on the hydrostatic pressure and the Lode parameter. The fracture envelope resulting from the model is "blossom" shaped and contains four material parameters that need to be calibrated with experimental observations.

More recently, Nahshon and Hutchinson (2008) have proposed a modification of the Gurson model that accounts for damage in shear dominated states. The yield surface remains unchanged, but the damage parameter (effective void volume fraction) evolves according to the volumetric component of the plastic strain rate plus an additional term that allows the damage to increase in cases of pure shear, leaving it unchanged for axisymmetric stress states. The model introduces a new parameter that sets the rate of damage development in shear. The measure of stress used by the authors is $\omega(\sigma) = 1 - \left(\frac{27 J_3}{2\sigma_e^3}\right)^2$

At low stress triaxiality, the evolution of the voids also depends on their origin. If voids are nucleated from inclusions, those inclusions could prevent the radial contraction of the void at low values of the stress triaxiality. This effect is usually not considered in the analyses.

### 3.1.6 Inertia effects

All the previously mentioned micromechanical models neglect inertia at the microscale. However, they have been shown to be non negligible in high strain rate processes. Pioneering studies were done by Carrol and Holt (1972) who considered the dynamic evolution of a void in a bounded matrix of plastic material. These results were extended by Cortes (1992a,b) and Tong and Ravichandran (1993) to account for hardening and strain rate sensitivity. On the other hand, Ortiz and Molinari (1992) considered a void in an infinite media and demonstrated the importance of inertia in void growth, especially in the long-term behavior. Based on this work, a variational constitutive model for porous viscoplastic media was derived by Weinberg et al. (2006).

[3]The Lode parameter is defined as $L = \frac{2\sigma_{II} - \sigma_I - \sigma_{III}}{\sigma_I - \sigma_{III}} = \frac{3(\sigma_I I - \sigma_m)}{\sigma_I - \sigma_{III}}$. $|L| = 1$ in axisymmetric stress states ($\sigma_I \geq \sigma_{II} = \sigma_{III}$ or $\sigma_I = \sigma_I I \geq \sigma_{III}$) and $L = 0$ for a pure shear superposed to a hydrostatic stress state ($\sigma_I = \sigma_m + \tau$, $\sigma_{II} = \sigma_m$, $\sigma_{III} = \sigma_m - \tau$).

More recent analysis (Molinari and Mercier, 2001) have also shown the instantaneous impact of microinertia in the macroscopic stresses, when the voided domain is treated as homogeneous. This model was applied to the case of a plate impact test (Czarnota et al., 2008) where comparison of the numerical results with the experiments indicated that micro-inertia was one of the key features for the accuracy of their finite element simulation.

## 3.2 Micromechanical model for void growth

Analytical consideration of damage for materials that exhibit hardening, strain rate sensitivity or plastic anisotropy, under general loading histories is inviable. It is therefore desirable to have a framework where arbitrary constitutive laws and loading conditions can be considered, as well as other effects such as temperature or surface energies. The goal of this work lies on the development of a numerical, physically sound and mathematically consistent constitutive framework for porous materials that is able to account for such general conditions.

A self-consistent two level finite element model is derived from a variational perspective, and a time discretization scheme together with a special finite element construction adapted to the problem is proposed. The continuous derivation of the formulation is treated in Section 3.3, whereas the time and space discretization are treated in Section 3.4 and 3.5, respectively.

This section is concerned with the choice of the appropriate representative volume element (RVE) that is used to describe the behavior of the porous material and allows the decoupling of the macroscopic and the microscopic scale. A domain can be considered an RVE if it is large enough compared to the size of the heterogeneities, but with a characteristic length smaller than the macroscopic length scale. For the following developments, the smaller length scale inside the RVE is also required to be sufficiently large for the theory of continuum mechanics to apply. The representative volume element considered, in view of its application to the characterization of porous materials, is a hollow sphere where the matrix is treated as a homogeneous continua.

The hollow sphere has been chosen as a simplification of a space-filling construction of packed hollow spheres. In Figure 3.2 a two-dimensional schematic representation is shown as well as a three-dimensional illustration of the construction. The existence of this construction is a direct result of the Vitali covering lemma (Gordon, 1994).

In a self-consistent multiscale model, certain macroscopic quantities are provided to the microscale, usually through the boundary of the RVE, and an appropriate averaging technique is defined allowing the recovery of the effective or macroscopic properties, including the imposed quantities.

So as to appropriately define the choice of the boundary conditions, a summary of the

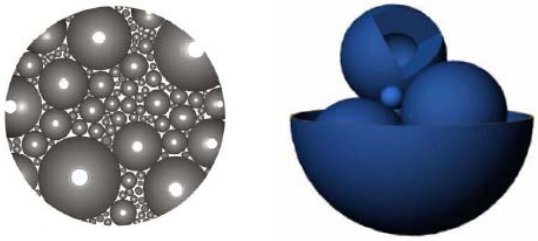

Figure 3.2: Space filling construction.

notation that is used throughout this chapter is given. Of particular interest in this work is the finite deformation case. The analysis is based on the Lagrangian formulation of the field equations with the initial unstressed state taken as reference. The material points of the microstructure are labeled $X$, and the reference configuration is identified with $B_0 \subset \mathbb{R}^3$. The superscript $M$ is employed to identify the macroscopic fields in contrast to the microscopic quantities, for which no superscript is used. By this notation, the macroscopic material points in the reference configuration $B_0^M$ are then denoted by $X^M$. The motion of the RVE is described by the deformation mapping $\mathbf{x} = \boldsymbol{\varphi}(\mathbf{X}, t)$, where $\mathbf{x}$ is the location of particle $\mathbf{X}$ at time t. The material velocity and acceleration fields are $\dot{\boldsymbol{\varphi}}$ and $\ddot{\boldsymbol{\varphi}}$, respectively, and the deformation gradient is denoted by $\mathbf{F} = \nabla\boldsymbol{\varphi}$, where $\nabla$ represents the material gradient. The motion of the body is required to satisfy linear momentum balance

$$\rho_0\ddot{\boldsymbol{\varphi}} - \nabla \cdot \mathbf{P} = \rho_0\mathbf{B}, \qquad \text{in} B_0 \tag{3.7}$$

where $\rho_0(\mathbf{X})$ is the mass density per unit undeformed volume, $\mathbf{B}$ are the body forces per unit mass and $\mathbf{P}$ is the first-Piola Kirchhoff stress tensor. The solution in equilibrium is also required to satisfy the boundary conditions

$$\begin{aligned} \boldsymbol{\varphi} &= \bar{\boldsymbol{\varphi}}, \qquad \text{on } \partial B_{0,1} \\ \mathbf{P} \cdot \mathbf{N} &= \bar{\mathbf{T}}, \qquad \text{on } \partial B_{0,2} \end{aligned} \tag{3.8}$$

where $\bar{\boldsymbol{\varphi}}$ and $\bar{\mathbf{T}}$ are the prescribed deformation mapping and the prescribed tractions respectively, and $\mathbf{N}$ is the outward normal to the domain. As usual, it is required that

$\partial B_0 = \partial B_{0,1} \cup \partial B_{0,2}$, and $\partial B_{0,1} \cap \partial B_{0,2} = \emptyset$.

In the literature three types of boundary conditions have been seen to be useful (see for instance, Besson et al. (2010)) and are here summarized

- Kinematic uniform boundary conditions (Hill, 1972, Ogden, 1974): $\mathbf{x} = \mathbf{F}^M \mathbf{X}$, $\mathbf{X}$ on $\partial B_0$, where $\mathbf{F}^M$ is the macroscopic deformation gradient, and therefore, independent of $\mathbf{X}$.

- Static uniform boundary conditions (Ogden, 1974): $\mathbf{PN} = \mathbf{P}^M \mathbf{N}$, $\mathbf{X}$ on $\partial B_0$.

- Periodic boundary conditions (Kwon et al., 2008). Examples relevant to the present study are Abeyaratne and Triantafyllidis (1984) and Bolzon and Vitaliani (1993).

In view of the desire to formulate the multiscale problem in the finite kinematic framework and with dynamic considerations, the first type of boundary condition is considered. A complete dual formulation under finite strains offers difficulties in general due to the lack of global convexity. The existence of a complementary energy, dual of the strain energy density, based on local convexity is discussed by Ogden (1974), Hill and Rice (1973) and Castañeda (1991). Therefore, the present work deals exclusively with kinematic uniform boundary conditions. However, as is proven in the next section, consistency between the two scales is achieved by essential boundary conditions that are dependent not only on the macroscopic deformation gradient, but also on the macroscopic displacement field.

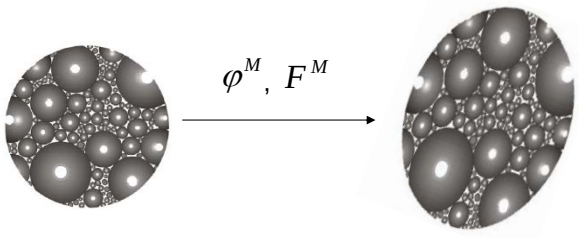


Figure 3.3: Deformation of the representative volume element according to the macroscopic deformation mapping $\varphi^M$ and the macroscopic deformation gradient $F^M$.

Under static conditions, and the simplifying assumption that all the spheres in the space-filling packing of a given macroscopic material point have the same void volume fraction, the problem can be reduced to the analysis of a single sphere due to scale invariance and the symmetries of the hollow sphere. By contrast, the dynamic case

lacks scale invariance and the response of each hollow sphere depends on its size, which necessitates consideration of the entire range of sizes present in the material. The same would occur if one were to introduce length scales in the problem by consideration of surface energies. In the computations, though, a single hollow sphere will be treated for each macroscopic quadrature point. The resulting boundary value problem is represented in Figure 3.4. On the left, the undeformed hollow sphere is represented, with inner radius $a$ and outer radius $b$. On the right, the deformed configuration together with the boundary conditions are shown. Stress-free boundary conditions are assumed for the inner radius.

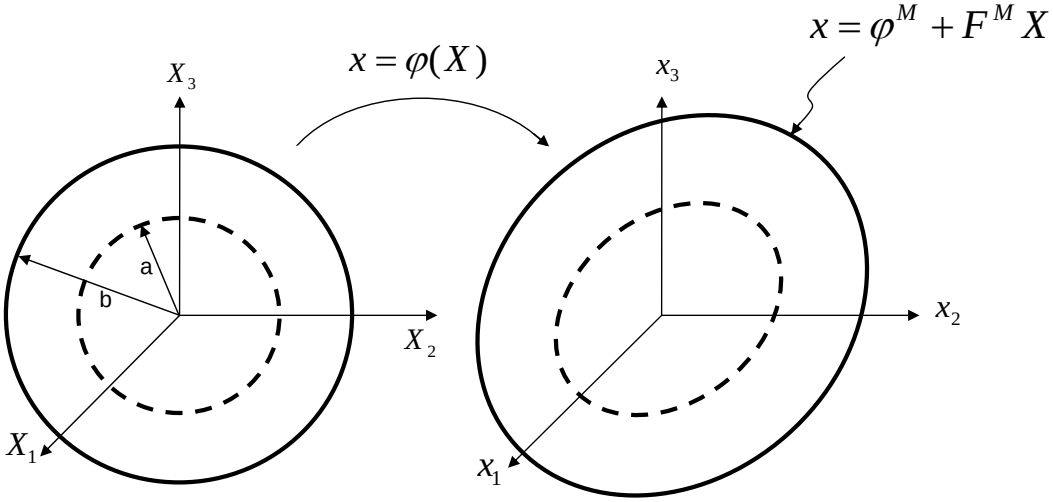


Figure 3.4: Boundary value problem over a hollow sphere of inner radius $a$ and outer radius $b$.

## 3.3 Effective constitutive behavior

This section is concerned with the definition of the macro-constitutive law from the response of a representative volume element under appropriate boundary conditions. This RVE is assumed to be composed of several homogeneous phases which are perfectly bonded. Some of this phases can be vacuous material as is the case of the hollow sphere introduced in the previous section. It is further assumed that the surface effects are negligible, so that the bulk macroscopic behavior depends exclusively on the bulk response of the different constituents. Extensions can be made to account for surface energies, although such treatment is not considered in the present work.

The boundary conditions required for a full consistent model will be shown to be

$$\boldsymbol{\varphi}(\mathbf{X}) = \boldsymbol{\varphi}^M + \nabla^M \boldsymbol{\varphi}^M \mathbf{X}, \qquad \text{on } \partial B_0 \tag{3.9}$$

The first term, consisting of the macroscopic displacement, is not included in standard boundary conditions. Under static loading with no body forces, it represents a rigid translation that is constant in time. Therefore, it can be disregarded recovering the standard geometric boundary conditions

$$\boldsymbol{\varphi}(\mathbf{X}) = \nabla^M \boldsymbol{\varphi}^M \mathbf{X}, \qquad \text{on } \partial B_0 \tag{3.10}$$

In the presence of body forces, the macroscopic displacement is the dual variable of the macroscopic body forces. Therefore, in order to recover all macro-variables from the formulation, the RVE needs to be informed about the macroscopic translation $\boldsymbol{\varphi}^M$. Moreover, even if the macroscopic stress is the only field of interest, it is physically meaningful to inform the RVE with the temporal evolution of the macroscopic displacement field, the rotations already being included in the deformation gradient. Two equivalent options can be followed, either considering a displacement of the microscopic reference frame, which therefore becomes non-inertial under general loading; or informing the RVE through the boundary conditions. The later will be pursued for the analytical derivations. However, from a numerical point of view, it might be favorable to have a non inertial representation of the equations if the material is undergoing large displacements.

It is worth mentioning that the origin of the material reference frame of the RVE needs

to be positioned such that

$$\int_{B_0} X_J \, dX = 0 \tag{3.11}$$

For the case of a hollow sphere, $B_0$ is the domain enclosed by the outer surface, and therefore includes the interior cavity. The results here obtained are general and apply to any domain subjected to the defined boundary conditions. The force and displacement fields are assumed to be continuous in the interior of the RVE.

The theoretical basis for the results here presented lies in the work of R. Hill and other authors that have subsequently contributed to the field (Hill, 1963, 1967, 1972, Ogden, 1974, Hill, 1984, Nemat-Nasser, 1999, Molinari and Mercier, 2001). Hill (1972) made the following interesting observation:

> "Experimental determinations of mechanical behavior rest ultimately on measured loads or mean displacement over pairs of opposite faces of a representative cube. Macro-variables intended for constitutive laws should thus be capable of definition in terms of surface data alone, either directly or indirectly. It is not necessary, by any means, that macro-variables so defined would be unweighted volume averages of their microscopic counterparts. However, variables that do have this special property are naturally the easiest to handle analytically in the transition between levels."

One such variable, whose average depends uniquely on the values at the surface, is the deformation gradient. Under the kinematic boundary conditions defined by Eq. 3.10 (Hill, 1972) the following result holds

$$\mathbf{F}^M = \frac{1}{|B_0|} \int_{B_0} \mathbf{F} \, dX = \frac{1}{|B_0|} \int_{\partial B_0} \mathbf{x} \otimes \mathbf{N} \, dX \tag{3.12}$$

making it a suitable variable to set the boundary conditions of the RVE.

The correspondence between the macroscopic deformation gradient and the average of the corresponding microscopic quantity is also valid for the proposed boundary conditions.

By repeated use of the divergence theorem

$$\begin{aligned}\frac{1}{|B_0|}\int_{B_0}\varphi_{i,J}\,dX &= \frac{1}{|B_0|}\int_{\partial B_0}\varphi_i N_J\,dX \\ &= \left[\frac{1}{|B_0|}\int_{\partial B_0} N_J\,dX\right]\varphi_i^M + \left[\frac{1}{|B_0|}\int_{\partial B_0} X_P N_J\,dX\right]\varphi_{i,P}^M = \varphi_{i,J}^M\end{aligned} \tag{3.13}$$

where $|B_0|$ is the volume of the RVE. This result is also applicable to the case where $B_0$ contains smooth holes. The deformation mapping can be extended to the interior of the voids by use of the extension lemmas of Cioranescu and Paulin (1979).

Based on the results of (Hill, 1972, Hill and Rice, 1973), Ogden (1974) identified a conceptually essential result for the approach that will be followed here. If the constituents of the RVE are elastic materials with a well defined strain energy density, then the average of the strain energy over the RVE is a function only of the average deformation gradient, and the effective stresses derive from such energy density. In view of the potential structure of the homogenized macroscopic media, also pointed out by Castañeda (1991), a variational perspective will be used, providing a suitable framework for extending the averaging results to dynamic conditions. When inertia effects are accounted for, the volume average of the Lagrangian density will be taken as an effective Lagrangian density for the homogeneous solid, from which the macroscopic balance equations can be obtained by recourse of the principle of stationary action. Under the assumption of separation of length and time scales, the effective Lagrangian density, defined in this case as the spacetime average of the corresponding mircoscopic quantity, will be shown to be a function of the averaged four-dimensional deformation gradient and act, analogously to the static case, as a potential for the energy-momentum tensor. These energetic relations between the micro and macro scale will be shown to be compatible with the definition of the macroscopic stress tensor and deformation gradient as surface integrals over the boundary of the RVE, as suggested by R. Hill. Furthermore, by this definition of the macroscopic Lagrangian density, the symmetries of the microscopic system and the corresponding conserved quantities during the motion are preserved through the homogenization process, providing a strong physical motivation for the proposed model. Consideration of variational structures of models with two different length scales haven been used previously under static condi-

tions within the formal theory of homogenization (Sanchez-Palencia, 1980, Müller, 1987, Terada and Kikuchi, 2001) and also in the context of RVE's where a finite microscale is assumed (Castañeda, 1991). However, the averaging technique here presented for finite kinematics together with the proposed boundary conditions for the RVE is new to the best of the author's knowledge.

It will be assumed throughout this section that the constituents of the RVE are hyperelastic and therefore posses a strain energy density $W = W(\mathbf{F})$ from which the first Piola-Kirchhoff stress tensor can be derived (see for example, Marsden and Hughes (1993))

$$\mathbf{P} = \frac{\partial W}{\partial \mathbf{F}} \tag{3.14}$$

It will further be assumed that the undeformed configuration is stress free, i.e., $W_{,\mathbf{F}}(\mathbf{I}) = 0$. Consideration of more general materials for the different phases of the RVE can be included in the variational structure via the Lagrange-d'Alembert principle (Marsden and S.Ratiu, 1999). The application of this principle in the field of continuum mechanics, and particularly for materials with viscosity and other internal processes, is described in Zielonka (2006). The approach that is followed in this work is that of Radovitzky and Ortiz (1999) in which incremental energy densities can be defined at each time step that are able to account for viscous and plastic effects. This is explained in further detail in Section 3.4.

### 3.3.1 Static case without body forces

Under static conditions, the solution in equilibrium satisfies the principle of minimum potential energy (Marsden and Hughes, 1993). In the absence of body forces, the microscopic potential energy $\Pi$ reads

$$\Pi[\boldsymbol{\varphi}(\cdot)] = \int_{B_0} W(\nabla\boldsymbol{\varphi}, \mathbf{X})\, dX \tag{3.15}$$

where the first Piola-Kirchhoff stress tensor obeys $\mathbf{P} = \frac{\partial W}{\partial \mathbf{F}}$, and the deformation mapping $\boldsymbol{\varphi}$ is required to satisfy the geometric boundary conditions on $\partial B_0$ (Eq. 3.9).

The macroscopic strain energy density is defined as the average of the corresponding microscopic quantity at equilibrium $W^*(\nabla\boldsymbol{\varphi}, \mathbf{X})$ with the boundary conditions defined by

Eq. 3.9.

$$W^M(\mathbf{F}^M, \mathbf{X}^M) = \frac{1}{|B_0|}\int_{B_0} W^*(\nabla\boldsymbol{\varphi}, \mathbf{X})\, dX \tag{3.16}$$

In the following derivations the superscript $^*$ will be omitted, although it will always be assumed that the macroscopic Lagrangian density (strain energy density in this case) is the volumetric average of the corresponding micro-variable when in equilibrium with the corresponding boundary conditions. Therefore $W^*(\nabla\boldsymbol{\varphi}, \mathbf{X})$ can be seen as a function of $\mathbf{F}^M$.

Taking variations of $W^M(\mathbf{F}^M, \mathbf{X}^M)$ with respect to $\mathbf{F}^M$ gives

$$\begin{aligned} |B_0|\delta W^M(\mathbf{F}^M) &= \int_{B_0} P_{iJ}\delta\varphi_{i,J}\, dX \\ &= \int_{\partial B_0} P_{iJ}N_J\delta\varphi_i\, dX \\ &= \left[\int_{\partial B_0} P_{iJ}N_J\, dX\right]\delta\varphi_i^M + \left[\int_{\partial B_0} P_{iJ}N_J X_P\, dX\right]\delta\varphi_{i,P}^M \\ &= \left[\int_{B_0} P_{iJ}\, dX\right]\delta\varphi_{i,J}^M \end{aligned} \tag{3.17}$$

$$\frac{\partial W^M}{\partial \varphi_{i,J}^M} = \frac{1}{|B_0|}\int_{B_0} P_{iJ}\, dX \tag{3.18}$$

The macroscopic potential energy can therefore be written as

$$\Pi^M[\boldsymbol{\varphi}^M(\cdot)] = \int_{B_0^M} W^M(\nabla^M\boldsymbol{\varphi}^M, \mathbf{X})\, dX^M - \int_{\partial B_{0,2}^M} \bar{\mathbf{T}}^M \cdot \boldsymbol{\varphi}^M\, dX^M \tag{3.19}$$

where $\bar{\mathbf{T}}^M$ are the tractions imposed on the boundary of the macroscopic domain.

By making the macroscopic potential energy stationary, the macroscopic equilibrium

equations and boundary conditions are recovered. If sufficient differentiability

$$\begin{aligned}
\delta\Pi^M &= \int_{B_0^M} \frac{\partial W^M}{\partial \varphi^M_{i,J}} \delta\varphi^M_{i,J}\, dX^M - \int_{\partial B^M_{0,2}} \bar{T}^M_i \delta\varphi^M_i\, dX^M \\
&= \int_{B_0^M} \left[\frac{1}{|B_0|}\int_{B_0} P_{iJ}\, dX\right] \delta\varphi^M_{i,J}\, dX^M - \int_{\partial B^M_{0,2}} \bar{T}^M_i \delta\varphi^M_i\, dX^M \\
&= -\int_{B_0^M} \left[\frac{1}{|B_0|}\int_{B_0} P_{iJ}\, dX\right]_{,J} \delta\varphi^M_i\, dX^M \\
&\quad + \int_{\partial B^M_{0,2}} \left[\left(\frac{1}{|B_0|}\int_{B_0} P_{iJ}\, dX\right) N^M_J - \bar{T}^M_i\right] \delta\varphi^M_i\, dX^M
\end{aligned} \tag{3.20}$$

$$\left[\frac{1}{|B_0|}\int_{B_0} P_{iJ}\, dX\right]_{,J} = 0, \qquad \text{in } B_0^M \tag{3.21a}$$

$$\left[\frac{1}{|B_0|}\int_{B_0} P_{iJ}\, dX\right] N^M_J = \bar{T}^M_i, \qquad \text{on } \partial B^M_{0,2} \tag{3.21b}$$

where the divergence of the averaged microscopic stress tensor is performed with respect to the macroscopic coordinates.

A consistent definition of the macroscopic stress tensor is therefore

$$\mathbf{P}^M = \frac{1}{|B_0|}\int_{B_0} \mathbf{P}\, dX \tag{3.22}$$

recovering the results of Hill (1972).

### 3.3.2 Static case with body forces

When body forces $\mathbf{B}$ are included, the microscopic potential energy has the following expression

$$\Pi[\boldsymbol{\varphi}(\cdot)] = \int_{B_0} \left(W(\boldsymbol{\varphi}, \mathbf{X}) - \rho_0 \mathbf{B}\cdot\boldsymbol{\varphi}\right) dX \tag{3.23}$$

Equivalently to the previous case, the macroscopic potential energy is defined as

$$\Pi^M[\boldsymbol{\varphi}^M(\cdot)] = \int_{B_0^M} \left[\frac{1}{|B_0|}\Pi[\boldsymbol{\varphi}]\right] dX^M - \int_{\partial B^M_{0,2}} \bar{\mathbf{T}}^M \cdot \boldsymbol{\varphi}^M\, dX^M \tag{3.24}$$

where, again, the micro-variables are in equilibrium under the appropriate boundary conditions.

Taking variations of $\Pi[\boldsymbol{\varphi}]$ with respect to $\boldsymbol{\varphi}^M$ leads to

$$\begin{aligned}
\delta\Pi[\boldsymbol{\varphi}] &= \int_{B_0} \left(P_{iJ}\delta\varphi_{i,J} - \rho_0 B_i \delta\varphi_i\right)\, dX \\
&= \int_{B_0} \left(-P_{iJ,J} - \rho_0 B_i\right)\delta\varphi_i\, dX + \int_{\partial B_0} P_{iJ}N_J\delta\varphi_i\, dX \\
&= \left[\int_{\partial B_0} P_{iJ}N_J\, dX\right]\delta\varphi_i^M + \left[\int_{\partial B_0} P_{iJ}N_J X_P\, dX\right]\delta\varphi_{i,P}^M \\
&= \left[-\int_{B_0} \rho_0 B_i\, dX\right]\delta\varphi_i^M + \left[\int_{B_0} \left(P_{iJ} + P_{iP,P}X_J\right)\, dX\right]\delta\varphi_{i,J}^M \\
&= \left[-\int_{B_0} \rho_0 B_i\, dX\right]\delta\varphi_i^M + \left[\int_{B_0} \left(P_{iJ} - \rho_0 B_i X_J\right)\, dX\right]\delta\varphi_{i,J}^M
\end{aligned} \tag{3.25}$$

$$\frac{\partial\Pi}{\partial\varphi_i^M} = -\int_{B_0} \rho_0 B_i\, dX \tag{3.26a}$$

$$\frac{\partial\Pi}{\partial\varphi_{i,J}^M} = \int_{B_0} \left(P_{iJ} - \rho_0 B_i X_J\right)\, dX \tag{3.26b}$$

By rendering the macroscopic potential energy stationary

$$\begin{aligned}
\delta\Pi^M &= \int_{B_0^M} \frac{1}{|B_0|}\left(\frac{\partial\Pi}{\partial\varphi_i^M}\delta\varphi_i^M + \frac{\partial\Pi}{\partial\varphi_{i,J}^M}\delta\varphi_{i,J}^M\right)\, dX^M - \int_{\partial B_{0,2}^M} \bar{T}_i^M\delta\varphi_i^M\, dX^M \\
&= \int_{B_0^M} \left[\frac{1}{|B_0|}\frac{\partial\Pi}{\partial\varphi_i^M} - \left(\frac{1}{|B_0|}\frac{\partial\Pi}{\partial\varphi_{i,J}^M}\right)_{,J}\right]\delta\varphi_i^M\, dX^M \\
&\quad + \int_{\partial B_{0,2}^M} \left[\frac{1}{|B_0|}\frac{\partial\Pi}{\partial\varphi_{i,J}^M}N_J^M - \bar{T}_i^M\right]\delta\varphi_i^M\, dX^M
\end{aligned} \tag{3.27}$$

the following Euler-Lagrange equations are obtained

$$\left[\frac{1}{|B_0|}\int_{B_0} \rho_0 B_i\, dX\right] + \left[\frac{1}{|B_0|}\int_{B_0} \left(P_{iJ} - \rho_0 B_i X_J\right)\, dX\right]_{,J} = 0, \qquad \text{in } B_0^M \tag{3.28a}$$

$$\left[\frac{1}{|B_0|}\int_{B_0} \left(P_{iJ} - \rho_0 B_i X_J\right)\, dX\right] N_J^M = \bar{T}_i^M, \qquad \text{on } \partial B_{0,2}^M \tag{3.28b}$$

where the divergence operation is performed with respect to the macroscopic coordinates.

The macroscopic body follows the standard equilibrium equations, where the macro-

scopic stresses and body forces are defined as

$$\mathbf{P}^M = \frac{1}{|B_0|}\int_{B_0} (\mathbf{P} - \rho_0 \mathbf{B} \otimes \mathbf{X})\, dX \tag{3.29a}$$

$$\rho_0^M \mathbf{B}^M = \frac{1}{|B_0|}\int_{B_0} \rho_0 \mathbf{B}\, dX \tag{3.29b}$$

For the particular case of a hollow sphere as choice of RVE, if the body forces and density are constant over the matrix, the macroscopic stresses can be simplified to

$$\mathbf{P}^M = \frac{1}{|B_0|}\int_{B_0} \mathbf{P}\, dX \tag{3.30}$$

and the macroscopic body forces are immediately defined as

$$\rho_0^M \mathbf{B}^M = (1-f)\rho_0 \mathbf{B} \tag{3.31}$$

where $f$ is the void volume fraction.

### 3.3.3 Dynamic case without separation of time scales

First, the more general case in which only separation of length scales is assumed will be analyzed. Under these conditions it is expected a contribution of the inertia forces in the macroscopic definition of stresses resulting from the mass movement within the RVE.

The underlying variational principle in dynamics is Hamilton's principle of stationary action (Marsden and Hughes, 1993). The action takes the form

$$\mathcal{A}[\boldsymbol{\varphi}(\cdot,\cdot)] = \int_{t_1}^{t_2} L(\boldsymbol{\varphi}, \dot{\boldsymbol{\varphi}}, t)\, dt \tag{3.32}$$

where $L(\boldsymbol{\varphi}, \dot{\boldsymbol{\varphi}}, t)$ is the Lagrangian of the body, defined as the difference between the kinetic energy of the body $T[\dot{\boldsymbol{\varphi}}]$ and the potential energy $\Pi[\boldsymbol{\varphi}]$, here defined

$$\begin{aligned} T[\dot{\boldsymbol{\varphi}}(\cdot,t)] &= \int_{B_0} \frac{1}{2}\rho_0 |\dot{\boldsymbol{\varphi}}|^2\, dX \\ \Pi[\boldsymbol{\varphi}(\cdot,t),t] &= \int_{B_0} (W(\nabla\boldsymbol{\varphi}, \mathbf{X}) - \rho_0 \mathbf{B}(t)\cdot\boldsymbol{\varphi})\, dX\, dt - \int_{\partial B_{0,2}} \bar{\mathbf{T}}\cdot\boldsymbol{\varphi}\, dX\, dt \end{aligned} \tag{3.33}$$

Hamilton's principle postulates that the motion $\boldsymbol{\varphi}(\mathbf{X}, t)$, which is required to satisfy the essential boundary conditions on $\partial B_{0,1}$ and is presumed known at times $t_1$ and $t_2$, renders the action stationary. Stationarity demands

$$\frac{d}{d\epsilon}\mathcal{A}[\boldsymbol{\varphi} + \epsilon\boldsymbol{\eta}]\Big|_{\epsilon=0} = 0 \tag{3.34}$$

for all admissible virtual displacements $\boldsymbol{\eta}$, satisfying $\boldsymbol{\eta}(t_1, \mathbf{X}) = \boldsymbol{\eta}(t_2, \mathbf{X}) = 0$ and

$$\boldsymbol{\eta}(t, \mathbf{X}) = \mathbf{0}, \qquad \text{in } \partial B_{0,1} \tag{3.35}$$

For the boundary value problem considered at the microscopic level, where no tractions are imposed on the boundary, a Lagrangian density can be defined

$$L[\boldsymbol{\varphi}, \mathbf{X}, t] = \frac{1}{2}\rho_0|\dot{\boldsymbol{\varphi}}|^2 - W(\nabla\boldsymbol{\varphi}, \mathbf{X}) + \rho_0\mathbf{B}(t)\cdot\boldsymbol{\varphi} \tag{3.36}$$

Under the proposed definition of the macro-Lagrangian density as the volumetric average of the micro-Lagrangian density, the microscopic and the macroscopic action have the following expressions

$$\mathcal{A}[\boldsymbol{\varphi}(\cdot,\cdot)] = \int_{t_1}^{t_2}\int_{B_0} L[\boldsymbol{\varphi}, \mathbf{X}, t]\, dX\, dt \tag{3.37a}$$

$$\mathcal{A}^M[\boldsymbol{\varphi}^M(\cdot,\cdot)] = \int_{t_1}^{t_2}\int_{B_0^M} \frac{1}{|B_0|}\left[\int_{B_0} L[\boldsymbol{\varphi}, \mathbf{X}, t]\, dX\right] dX^M\, dt \tag{3.37b}$$

$$+ \int_{t_1}^{t_2}\int_{\partial B_{0,2}^M} \bar{T}^M\cdot\boldsymbol{\varphi}^M\, dX^M\, dt \tag{3.37c}$$

Variation of the microscopic action with respect to the macroscopic deformation map-

ping gives

$$
\begin{aligned}
\delta\mathcal{A} &= \int_{t_1}^{t_2}\int_{B_0} \left(\rho_0\dot{\varphi}_i\delta\dot{\varphi}_i - P_{iJ}\delta\varphi_{i,J} + \rho_0 B_i\delta\varphi_i\right)\, dX\, dt \\
&= \int_{t_1}^{t_2}\int_{B_0} \rho_0\dot{\varphi}_i\delta\dot{\varphi}_i\, dX\, dt + \int_{t_1}^{t_2}\int_{B_0} (P_{iJ,J} + \rho_0 B_i)\delta\varphi_i\, dX\, dt \\
&\quad - \int_{t_1}^{t_2}\int_{\partial B_0} P_{iJ}N_J\delta\varphi_i\, dX\, dt \\
&= \int_{t_1}^{t_2}\int_{B_0} \rho_0(\dot{\varphi}_i\delta\dot{\varphi}_i + \ddot{\varphi}_i\delta\varphi_i)\, dX\, dt - \left[\int_{t_1}^{t_2}\int_{\partial B_0} P_{iJ}N_J\, dX\, dt\right]\delta\varphi_i^M \\
&\quad - \left[\int_{t_1}^{t_2}\int_{\partial B_0} P_{iP}N_P X_J\, dX\, dt\right]\delta\varphi_{i,J}^M \qquad (3.38) \\
&= \int_{B_0} \rho_0(\dot{\varphi}_i\delta\varphi_i)\Big|_{t_1}^{t_2} dX - \left[\int_{t_1}^{t_2}\int_{\partial B_0} (\rho_0\ddot{\varphi}_i - \rho_0 B_i)\, dX\, dt\right]\delta\varphi_i^M \\
&\quad - \left[\int_{t_1}^{t_2}\int_{\partial B_0} P_{iP}N_P X_J\, dX\, dt\right]\delta\varphi_{i,J}^M \\
&= -\left[\int_{t_1}^{t_2}\int_{\partial B_0} (\rho_0\ddot{\varphi}_i - \rho_0 B_i)\, dX\, dt\right]\delta\varphi_i^M \\
&\quad - \left[\int_{t_1}^{t_2}\int_{\partial B_0} \left(P_{iJ} + \rho_0\ddot{\varphi}_i X_J - \rho_0 B_i X_J\right)\, dX\, dt\right]\delta\varphi_{i,J}^M
\end{aligned}
$$

It has been assumed for simplicity that each phase within the RVE has a density which is constant in time.

Stationarity of the macro-action results in

$$\begin{aligned}
\delta\mathcal{A}^M = &-\int_{t_1}^{t_2}\int_{B_0^M}\left[\frac{1}{|B_0|}\int_{B_0}(\rho_0\ddot{\varphi}_i-\rho_0 B_i)\,dX\right]\delta\varphi_i^M\,dX^M\,dt\\
&-\int_{t_1}^{t_2}\int_{B_0^M}\left[\frac{1}{|B_0|}\int_{B_0}(P_{iJ}+\rho_0\ddot{\varphi}_i X_J-\rho_0 B_i X_J)\,dX\right]\delta\varphi_{i,J}^M\,dX^M\,dt\\
&+\int_{t_1}^{t_2}\int_{\partial B_{0,2}^M}\bar{T}_i^M\varphi_i^M\,dX^M\,dt\\
=&-\int_{t_1}^{t_2}\int_{B_0^M}\left[\frac{1}{|B_0|}\int_{B_0}(\rho_0\ddot{\varphi}_i-\rho_0 B_i)\,dX\right]\delta\varphi_i^M\,dX^M\,dt\\
&+\int_{t_1}^{t_2}\int_{B_0^M}\left[\frac{1}{|B_0|}\int_{B_0}(P_{iJ}+\rho_0\ddot{\varphi}_i X_J-\rho_0 B_i X_J)\,dX\right]_{,J}\delta\varphi_i^M\,dX^M\,dt\\
&+\int_{t_1}^{t_2}\int_{\partial B_{0,2}^M}\left[\bar{T}_i^M-\left(\frac{1}{|B_0|}\int_{B_0}(P_{iJ}+\rho_0\ddot{\varphi}_i X_J-\rho_0 B_i X_J)\,dX\right)N_J^M\right]\varphi_i^M\,dX^M\,dt
\end{aligned}\tag{3.39}$$

leading to the following balance equations

$$\begin{aligned}
\left[\frac{1}{|B_0|}\int_{B_0}\rho_0\ddot{\varphi}_i\,dX\right]-\left[\frac{1}{|B_0|}\int_{B_0}(P_{iJ}+\rho_0\ddot{\varphi}_i X_J-\rho_0 B_i X_J)\,dX\right]_{,J}\\
=\left[\frac{1}{|B_0|}\int_{B_0}\rho_0 B_i\,dX\right],\qquad\text{in } [t_1,t_2]\times B_0^M
\end{aligned}\tag{3.40}$$

$$\left[\frac{1}{|B_0|}\int_{B_0}(P_{iJ}+\rho_0\ddot{\varphi}_i X_J-\rho_0 B_i X_J)\,dX\right]N_J^M=\bar{T}_i^M,\qquad\text{on } [t_1,t_2]\times\partial B_{0,2}^M \tag{3.41}$$

It is notable that the standard equilibrium equations have been recovered at the macroscopic level. This is not always the case when averaging is performed on a representative volume element.

The macroscopic stresses and body forces can be identified with

$$\mathbf{P}^M=\frac{1}{|B_0|}\int_{B_0}(\mathbf{P}+\rho_0\ddot{\boldsymbol{\varphi}}\otimes\mathbf{X}-\rho_0\mathbf{B}\otimes\mathbf{X})\,dX \tag{3.42}$$

$$\rho_0^M \mathbf{B}^M = \frac{1}{|B_0|} \int_{B_0} \rho_0 \mathbf{B}\, dX \tag{3.43}$$

which reduce for the particular case of the hollow sphere of homogeneous material with constant body forces to

$$\mathbf{P}^M = \frac{1}{|B_0|} \int_{B_0} (\mathbf{P} + \rho_0 \ddot{\boldsymbol{\varphi}} \otimes \mathbf{X})\, dX \tag{3.44}$$

$$\rho_0^M \mathbf{B}^M = \rho_0 (1 - f) \mathbf{B} \tag{3.45}$$

where $f$ is the void volume fraction.

This later definition of macroscopic stresses coincides with the one obtained by Molinari and Mercier (2001) by recourse to the principle of virtual work. The value of the microscopic fields, though, are obtained from a different boundary value problem. In the proposed formulation, the macroscopic displacements are passed through the boundary of the representative volume element, in addition to the macroscopic deformation gradient. This allows the microstructure to experience the macroscopic acceleration, which might influence the microstructure evolution and therefore the final value of the macroscopic stresses. Wright and Ramesh (2008) reviewed the work of Molinari and Mercier (2001) with explicit use of composition of velocities stating therefore the non inertial character of the reference frame associated to the RVE.

These results were obtained under the assumption of separation of length scales, but no a priori assumption on the separation of time scales. Under these conditions, no averaging equivalence exists between the microscopic and macroscopic linear momentum and the following macroscopic equilibrium equation

$$\rho_0^M \ddot{\boldsymbol{\varphi}}^M - \nabla^M \cdot \mathbf{P}^M = \rho_0^M \mathbf{B}^M \tag{3.46}$$

is an approximation. However, it can be regarded as exact, if the macroscopic body forces

contain an additional term resulting from the microinertia

$$\rho_0^M \mathbf{B}^M = \frac{1}{|B_0|} \int_{B_0} \rho_0 \left( \mathbf{B} + \ddot{\boldsymbol{\varphi}} - \ddot{\boldsymbol{\varphi}}^M \right) \, dX \tag{3.47}$$

In the following it will be seen that Eq. 3.46 is recovered exactly in the event of separation of length and time scales.

### 3.3.4 Dynamic case with separation of time and length scales

When separation of time scales holds in addition to separation of length scales, the macroscopic quantities can be defined as an average over a four-dimensional representative volume element, where time is included. Some conditions in which this situation is encountered are shown in Section 3.6.6.

Instead of proceeding with the derivations in the usual three-dimensional space with time as a separate dimension, a four-dimensional perspective is adopted. In order to do so, the equations of elastodynamics are first rewritten in a spacetime framework following closely the Continuum Mechanics Course Notes of Ortiz (2010). As will be seen, there is an astonishing resemblance with the three-dimensional static equations. By this observation, it is predictable that a fully consistent multiscale dynamic model can be obtained when applying affine spacetime boundary conditions to the four-dimensional representative volume element (RVE4).

#### 3.3.4.1 The spacetime formulation of nonlinear elastodynamics

Within the Lagrangian description of the motion of a body, time will be regarded as an additional variable. The reference configuration in this four-dimensional space is identified with $\Omega_0 = [t_1, t_2] \times B_0 \subset \mathbb{R}^4$. The boundary of such a domain has the structure $\Gamma_0 = \partial\Omega_0 = ([t_1, t_2] \times \partial B_0) \cup (\{t_1\} \times B_0) \cup (\{t_2\} \times B_0)$, where the four-dimensional unit normal

$\mathtt{N}$ is defined as

$$\mathtt{N} = \{0, \mathbf{N}\}, \qquad \text{on } [t_1, t_2] \times \partial B_0 \tag{3.48a}$$

$$\mathtt{N} = \{-1, \mathbf{0}\}, \qquad \text{on } \{t_1\} \times B_0 \tag{3.48b}$$

$$\mathtt{N} = \{1, \mathbf{0}\}, \qquad \text{on } \{t_2\} \times B_0 \tag{3.48c}$$

with $\mathbf{N}$ being the outward normal to $\partial B_0$. The boundary $\partial\Omega_0$ of $\Omega_0$ is partitioned into $\partial\Omega_{0,1}$ and $\partial\Omega_{0,2}$ where essential and natural boundary conditions are, respectively, imposed. As usual, we require $\partial\Omega_0 = \partial\Omega_{0,1} \cup \partial\Omega_{0,2}$, and $\partial\Omega_{0,1} \cap \partial\Omega_{0,2} = \emptyset$.

Material points will be labeled as

$$\mathtt{X} = \{t, \mathbf{X}\} \tag{3.49}$$

and the corresponding Eulerian position four-vector $\mathtt{x}$ and deformation mapping $\mathtt{y}$ are defined as

$$\mathtt{x} = \{t, \mathbf{x}\} = \mathtt{y}(\mathtt{X}) = \{t, \varphi(\mathbf{X})\} \tag{3.50}$$

The spacetime Lagrangian velocity then follows as

$$\mathtt{V} = \frac{\partial \mathtt{y}}{\partial t} = \{1, \mathbf{V}\} \tag{3.51}$$

The spacetime deformation mapping is then

$$\mathtt{F} = \mathtt{Grad}\ \mathtt{y} = \left(\begin{array}{c|c} 1 & \mathbf{0} \\ \hline \mathbf{V} & \mathbf{F} \end{array}\right)$$

and its inverse follows as

$$\mathtt{F}^{-1} = \left(\begin{array}{c|c} 1 & \mathbf{0} \\ \hline -\boldsymbol{\varphi}^*\mathbf{V} & \mathbf{F}^{-1} \end{array}\right)$$

where $\boldsymbol{\varphi}^*\mathbf{V} = \mathbf{F}^{-1}\mathbf{V}$ is the pullback of the Lagrangian velocity field. Its spacetime analog

is

$$\mathtt{y}^{*}\mathtt{V} = \mathtt{F}^{-1}\mathtt{V} = \{1, \mathbf{0}\} \tag{3.52}$$

The generalization of the stress tensor in the spacetime framework is the energy-momentum four tensor

$$\mathtt{S} = \rho_0 \mathtt{V} \otimes \mathtt{y}^{*}\mathtt{V} - \mathtt{P} = \left(\begin{array}{c|c} \rho_0 & \mathbf{0} \\ \hline \rho_0 \mathbf{V} & -\mathbf{P} \end{array}\right)$$

where

$$\mathtt{P} = \left(\begin{array}{c|c} 0 & \mathbf{0} \\ \hline \mathbf{0} & \mathbf{P} \end{array}\right)$$

is the spacetime extension of the first Piola-Kirchhoff stress tensor.

The Lagrangian body force four-vector per unit mass is

$$\mathtt{B} = \{0, \mathbf{B}\} \tag{3.53}$$

and the four-vector traction applied on $\partial\Omega_{0,2}$ has the structure

$$\bar{\mathtt{T}} = \{0, \bar{\mathbf{T}}\}, \qquad \text{on } [t_1, t_2] \times \partial B_0 \tag{3.54a}$$

$$\bar{\mathtt{T}} = \rho_0 \{1, \bar{\mathbf{V}}_1\}, \qquad \text{on } \{t_1\} \times B_0 \tag{3.54b}$$

$$\bar{\mathtt{T}} = \rho_0 \{-1, -\bar{\mathbf{V}}_2\}, \qquad \text{on } \{t_2\} \times B_0 \tag{3.54c}$$

In this notation, the mass and linear momentum conservation laws and the boundary conditions can be written in the following compact form

$$\mathtt{Div}\ \mathtt{S} = \rho_0 \mathtt{B}, \qquad \text{in } \Omega_0 \tag{3.55a}$$

$$\mathtt{SN} = -\bar{\mathtt{T}}, \qquad \text{on } \partial\Omega_{0,2} \tag{3.55b}$$

The time component leads to mass conservation

$$\frac{\partial \rho_0}{\partial t} = 0, \qquad \text{in } \Omega_0 \tag{3.56a}$$

$$0 = 0, \qquad \text{on } [t_1, t_2] \times \partial B_0 \tag{3.56b}$$

$$-\rho_0 + \rho_0 = 0, \qquad \text{on } \{t_1\} \times B_0 \tag{3.56c}$$

$$\rho_0 - \rho_0 = 0, \qquad \text{on } \{t_2\} \times B_0 \tag{3.56d}$$

$$\tag{3.56e}$$

and the spatial components to the corresponding linear momentum conservation equations

$$\frac{\partial}{\partial t}(\rho_0 \mathbf{V}) - \mathrm{Div}\mathbf{P} = \rho_0 \mathbf{B}, \qquad \text{in } \Omega_0 \tag{3.57a}$$

$$\mathbf{P}\mathbf{N} = \bar{\mathbf{T}}, \qquad \text{on } [t_1, t_2] \times \partial B_0 \tag{3.57b}$$

$$-\rho_0 \mathbf{V} + \rho_0 \bar{\mathbf{V}}_1 = 0, \qquad \text{on } \{t_1\} \times B_0 \tag{3.57c}$$

$$\rho_0 \mathbf{V} - \rho_0 \bar{\mathbf{V}}_2 = 0, \qquad \text{on } \{t_2\} \times B_0 \tag{3.57d}$$

$$\tag{3.57e}$$

Extensions of this formulation to account for other effects such as non Euclidean domains, variable local time scale or mass erosion and accretion are possible, although they have not been pursued here.

**Principle of stationary action.** Under dynamic conditions, the motion of the solid obeys the principle of stationary action. The action takes the form

$$\mathcal{A}[\boldsymbol{\varphi}(\cdot,\cdot)] = \int_{t_1}^{t_2} \int_{B_0} (\frac{1}{2}\rho_0 |\dot{\boldsymbol{\varphi}}|^2 - W(\nabla \boldsymbol{\varphi}, \mathbf{X}) + \rho_0 \mathbf{B} \cdot \boldsymbol{\varphi})\, dX\, dt + \int_{t_1}^{t_2} \int_{\partial B_{0,2}} \bar{\mathbf{T}} \cdot \boldsymbol{\varphi}\, dX\, dt \tag{3.58}$$

when $\boldsymbol{\varphi}$ is presumed to be known at times $t_1$ and $t_2$ and satisfies the essential boundary conditions.

If instead of the deformation mapping $\boldsymbol{\varphi}$, the initial and final velocity fields are pre-

scribed at times $t_1$ and $t_2$ to $\mathbf{V}(t_1, \mathbf{X}) = \bar{\mathbf{V}}_1(\mathbf{X})$ and $\mathbf{V}(t_2, \mathbf{X}) = \bar{\mathbf{V}}_2(\mathbf{X})$, then the action takes the form

$$\begin{aligned}\mathcal{A}[\boldsymbol{\varphi}(\cdot,\cdot)] = \int_{t_1}^{t_2}\int_{B_0}(\frac{1}{2}\rho_0|\dot{\boldsymbol{\varphi}}|^2 - W(\nabla\boldsymbol{\varphi}, \mathbf{X}) + \rho_0\mathbf{B}\cdot\boldsymbol{\varphi})\,dX\,dt + \int_{t_1}^{t_2}\int_{\partial B_{0,2}}\bar{\mathbf{T}}\cdot\boldsymbol{\varphi}\,dX\,dt \\ + \int_{B_0}\rho_0\left[\bar{\mathbf{V}}_1(\mathbf{X})\cdot\boldsymbol{\varphi}(t_1,\mathbf{X}) - \bar{\mathbf{V}}_2(\mathbf{X})\cdot\boldsymbol{\varphi}(t_2,\mathbf{X})\right]\,dX\end{aligned} \tag{3.59}$$

Both of this cases can be considered in a joint manner in the spacetime formalism, through the observation that initial and final linear momentum can be treated as tractions in the four-dimensional domain.

$$\mathcal{A}[\mathtt{y}(\cdot)] = \int_{\Omega_0}\left(\frac{1}{2}\rho_0(|\dot{\mathtt{y}}|^2 - 1) - W(\mathbf{F}, \mathtt{X}) + \rho_0\mathtt{B}\cdot\mathtt{y}\right)\,d\mathtt{X} + \int_{\partial\Omega_{0,2}}\bar{\mathtt{T}}\cdot\mathtt{y}\,d\mathtt{X} \tag{3.60}$$

Disregarding the traction boundary conditions, the Lagrangian density reads $L[\mathtt{y}, \mathtt{X}] = \frac{1}{2}\rho_0(|\dot{\mathtt{y}}|^2 - 1) - W(\mathbf{F}, \mathtt{X}) + \rho_0\mathtt{B}\cdot\mathtt{y}$, and the energy-momentum tensor satisfies

$$\mathtt{S} = \frac{\partial L}{\partial \mathtt{F}} \tag{3.61}$$

From these relations it is therefore clear that the energy-momentum tensor generalizes the concept of stress as to account for inertia.

#### 3.3.4.2 Spacetime averaging

In this section, a four-dimensional averaging is performed over a representative spacetime domain, under the assumption that separation of time scales holds in addition to separation of length scales. The representative volume element in the four-dimensional space (RV4) for the example of the hollow sphere is shown in Fig. 3.5. Again, the results obtained are completely general and independent of the RVE used.

In analogy to the static case, essential spacetime affine boundary conditions are considered

$$\mathtt{y} = \mathtt{y}^M + \mathtt{Grad}^M\mathtt{y}^M\mathtt{X},\ \text{on}\ \partial\Omega_0 \tag{3.62}$$

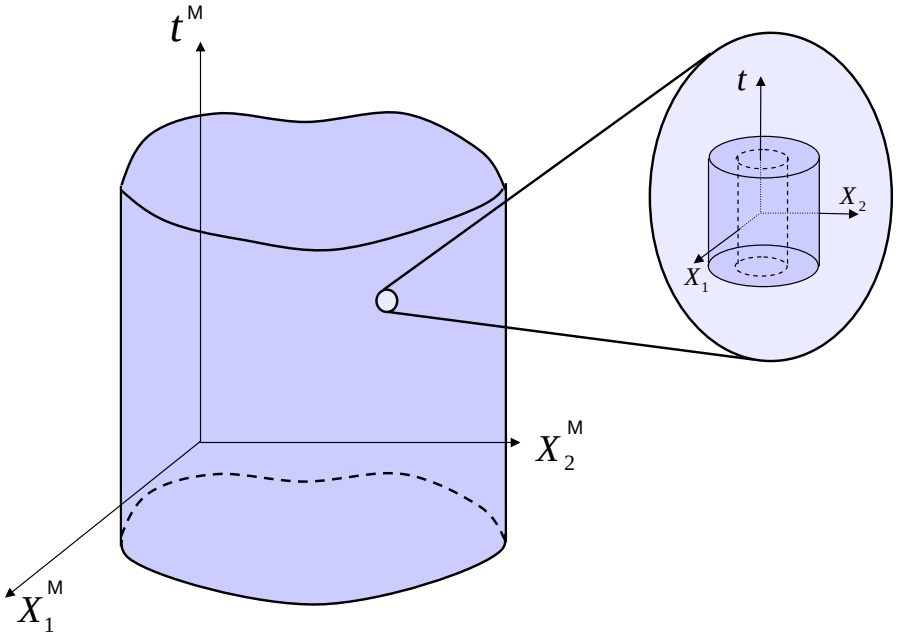


Figure 3.5: Representative spacetime domain at the macroscopic and microscopic level.

where $\Omega_0 = [-\tau/2, \tau/2] \times B_0$ and $B_0$ is the entire volume enclosed by the outer surface of the RVE. Equivalently,

$$\mathrm{y} = \begin{pmatrix} t^M \\ \hline \mathbf{X}^M \end{pmatrix} + \left(\begin{array}{c|c} 1 & \mathbf{0} \\ \hline \mathbf{V}^M & \mathbf{F}^M \end{array}\right) \begin{pmatrix} t \\ \hline \mathbf{X} \end{pmatrix} = \begin{pmatrix} t^M + t \\ \hline \mathbf{X}^M + \mathbf{V}^M t + \mathbf{F}^M \mathbf{X} \end{pmatrix}$$

Affine boundary conditions in the four-dimensional space also require that the origin of the spacetime material reference frame is positioned such that

$$\int_{\Omega_0} \mathtt{X}\, d\mathtt{X} = 0 \tag{3.63}$$

Satisfaction of this relation is essential for the full consistency of the considered two-scale model. Under these conditions, by repeated use of the divergence theorem, the spacetime gradient of the four-vector deformation gradient is equal to the macroscopic

spacetime deformation gradient.

$$\begin{aligned}\frac{1}{|\Omega_0|}\int_{\Omega_0} \mathtt{y}_{\alpha,B}\, d\mathtt{X} &= \frac{1}{|\Omega_0|}\int_{\partial\Omega_0} \mathtt{y}_\alpha \mathtt{N}_B\, d\mathtt{X} \\ &= \left[\frac{1}{|\Omega_0|}\int_{\partial\Omega_0} \mathtt{N}_B\, d\mathtt{X}\right] \mathtt{y}^M_\alpha + \left[\frac{1}{|\Omega_0|}\int_{\partial\Omega_0} \mathtt{X}_P \mathtt{N}_B\, d\mathtt{X}\right] \mathtt{y}^M_{\alpha,P} = \mathtt{y}^M_{\alpha,B}\end{aligned} \tag{3.64}$$

Therefore, the proposed four-dimensional boundary conditions seem suitable to establish the connection between micro and macro-variables in this spacetime framework.

In view of the static results we expect the macroscopic action $\mathcal{A}^M$ to be defined as

$$\mathcal{A}^M[\mathtt{y}^M(\cdot)] = \int_{\Omega_0^M} \frac{1}{|\Omega_0|}\mathcal{A}\, d\mathtt{X}^M + \int_{\partial\Omega^M_{0,2}} \bar{\mathtt{T}}^M \cdot \mathtt{y}^M\, d\mathtt{X}^M \tag{3.65}$$

where $\Omega_0^M = [t_1^M, t_2^M] \times B_0^M$ and the microscopic action is

$$\mathcal{A}[\mathtt{y}(\cdot)] = \int_{\Omega_0} L\, d\mathtt{X} \tag{3.66}$$

where $L$ is the Lagrangian density.

Taking variations of the microscopic action with respect to the macroscopic field

$$\begin{aligned}\delta\mathcal{A} &= \int_{\Omega_0} \left(\mathtt{S}_{\alpha B}\delta\mathtt{y}_{\alpha,B} + \rho_0 \mathtt{B}_\alpha \delta\mathtt{y}_\alpha\right)\, d\mathtt{X} \\ &= \int_{\Omega_0} \left(-\mathtt{S}_{\alpha B,B} + \rho_0\mathtt{B}_\alpha\right)\delta\mathtt{y}_\alpha\, d\mathtt{X} + \int_{\Omega_0} \left(\mathtt{S}_{\alpha B}\delta\mathtt{y}_\alpha\right)_{,B}\, d\mathtt{X} \\ &= \int_{\partial\Omega_0} \mathtt{S}_{\alpha B}\mathtt{N}_B\delta\mathtt{y}_\alpha\, d\mathtt{X} \\ &= \left[\int_{\partial\Omega_0} \mathtt{S}_{\alpha B}\mathtt{N}_B\, d\mathtt{X}\right]\delta\mathtt{y}^M_\alpha + \left[\int_{\partial\Omega_0} \mathtt{S}_{\alpha B}\mathtt{N}_B\mathtt{X}_P\, d\mathtt{X}\right]\delta\mathtt{y}^M_{\alpha,P} \\ &= \left[\int_{\Omega_0} \mathtt{S}_{\alpha B,B}\, d\mathtt{X}\right]\delta\mathtt{y}^M_\alpha + \left[\int_{\partial\Omega_0} \mathtt{T}_\alpha \mathtt{X}_P\, d\mathtt{X}\right]\delta\mathtt{y}^M_{\alpha,P} \\ &= \left[\int_{\Omega_0} \rho_0\mathtt{B}_\alpha\, d\mathtt{X}\right]\delta\mathtt{y}^M_\alpha + \left[\int_{\Omega_0} \left(\mathtt{S}_{\alpha B} + \mathtt{S}_{\alpha P,P}\mathtt{X}_B\right)\, d\mathtt{X}\right]\delta\mathtt{y}^M_{\alpha,P} \\ &= \left[\int_{\Omega_0} \rho_0\mathtt{B}_\alpha\, d\mathtt{X}\right]\delta\mathtt{y}^M_\alpha + \left[\int_{\Omega_0} \left(\mathtt{S}_{\alpha B} + \rho_0\mathtt{B}_\alpha\mathtt{X}_B\right)\, d\mathtt{X}\right]\delta\mathtt{y}^M_{\alpha,P}\end{aligned} \tag{3.67}$$

$$\frac{\partial \mathcal{A}}{\partial \mathtt{y}^M_\alpha} = \int_{\Omega_0} \rho_0 \mathtt{B}_\alpha \, d\mathtt{X} \tag{3.68a}$$

$$\frac{\partial \mathcal{A}}{\partial \mathtt{y}^M_{\alpha,B}} = \int_{\Omega_0} \left( \mathtt{S}_{\alpha B} + \rho_0 \mathtt{B}_\alpha \mathtt{X}_B \right) \, d\mathtt{X} \tag{3.68b}$$

$$\tag{3.68c}$$

By rendering the macroscopic action stationary

$$\begin{aligned} \delta \mathcal{A}^M &= \int_{\Omega_0^M} \frac{1}{|\Omega_0|} \left( \frac{\partial \mathcal{A}}{\partial \mathtt{y}^M_\alpha} \delta \mathtt{y}^M_\alpha + \frac{\partial \mathcal{A}}{\partial \mathtt{y}^M_{\alpha,B}} \delta \mathtt{y}^M_{\alpha,B} \right) d\mathtt{X}^M \\ &\quad + \int_{\partial \Omega^M_{0,2}} \bar{\mathtt{T}}^M_\alpha \delta \mathtt{y}^M_\alpha \, d\mathtt{X}^M \\ &= \int_{\Omega_0^M} \left[ \left( \frac{1}{|\Omega_0|} \frac{\partial \mathcal{A}}{\partial \mathtt{y}^M_\alpha} \right) - \left( \frac{1}{|\Omega_0|} \frac{\partial \mathcal{A}}{\partial \mathtt{y}^M_{\alpha,B}} \right)_{,B} \right] \delta \mathtt{y}^M_\alpha \, d\mathtt{X}^M \\ &\quad + \int_{\partial \Omega^M_{0,2}} \left[ \left( \frac{1}{|\Omega_0|} \frac{\partial \mathcal{A}}{\partial \mathtt{y}^M_{\alpha,B}} \right) \mathtt{N}^M_B + \bar{\mathtt{T}}^M_\alpha \right] \delta \mathtt{y}^M_\alpha \, d\mathtt{X}^M \end{aligned} \tag{3.69}$$

the macroscopic equilibrium equations and boundary conditions are derived

$$\left( \frac{1}{|\Omega_0|} \frac{\partial \mathcal{A}}{\partial \mathtt{y}^M_{\alpha,B}} \right)_{,B} = \left( \frac{1}{|\Omega_0|} \frac{\partial \mathcal{A}}{\partial \mathtt{y}^M_\alpha} \right), \text{ in } \Omega^M_0 \tag{3.70a}$$

$$\left( \frac{1}{|\Omega_0|} \frac{\partial \mathcal{A}}{\partial \mathtt{y}^M_{\alpha,B}} \right) \mathtt{N}^M_B = -\bar{\mathtt{T}}^M_\alpha, \text{ on } \partial \Omega_{0,2} \tag{3.70b}$$

In order to identify the suitable definition of the macro-variables in the more conventional three-dimensional space, the previous equations will be rewritten as

$$\mathtt{S} + \rho_0 \mathtt{B} \otimes \mathtt{X} = \left( \begin{array}{c|c} \rho_0 & \mathbf{0} \\ \hline \rho_0 \mathbf{V} + \rho_0 \mathbf{B} t & -\mathbf{P} + \rho_0 \mathbf{B} \otimes \mathbf{X} \end{array} \right)$$

The equilibrium equations and boundary conditions read

$$\begin{aligned}
&\tfrac{d}{dt^M}\left[\tfrac{1}{\tau}\tfrac{1}{|B_0|}\int_{-\tau/2}^{\tau/2}\int_{B_0}\left(\rho_0 V_i+\rho_0 B_i t\right)\,dX\,dt\right]-\left[\tfrac{1}{\tau}\tfrac{1}{|B_0|}\int_{-\tau/2}^{\tau/2}\int_{B_0}\left(P_{iJ}-\rho_0 B_i X_J\right)\,dX\,dt\right]_{,J}=\\
&\qquad\left[\tfrac{1}{\tau}\tfrac{1}{|B_0|}\int_{-\tau/2}^{\tau/2}\int_{B_0}\rho_0 B_i\,dX\,dt\right], \qquad \text{in } [t_1^M,t_2^M]\times B_0^M\\
&\tfrac{1}{\tau}\tfrac{1}{|B_0|}\int_{-\tau/2}^{\tau/2}\int_{B_0}\rho_0\,dX\,dt=\rho_0^M, \qquad \text{on } (\{t_1^M\}\cup\{t_2^M\})\times B_0^M\\
&\left[\tfrac{1}{\tau}\tfrac{1}{|B_0|}\int_{-\tau/2}^{\tau/2}\int_{B_0}(\rho_0 V_i+\rho_0 B_i t)\,dX\,dt\right]\Big|_{t^M=t_1^M}=\rho_0^M\bar{V}_i^{1M}, \qquad \text{on } \{t_1^M\}\times B_0^M\\
&\left[\tfrac{1}{\tau}\tfrac{1}{|B_0|}\int_{-\tau/2}^{\tau/2}\int_{B_0}(\rho_0 V_i+\rho_0 B_i t)\,dX\,dt\right]\Big|_{t^M=t_2^M}=\rho_0^M\bar{V}_i^{2M}, \qquad \text{on } \{t_2^M\}\times B_0^M\\
&\left[\tfrac{1}{\tau}\tfrac{1}{|B_0|}\int_{-\tau/2}^{\tau/2}\int_{B_0}\left(P_{iJ}-\rho_0 B_i X_J\right)dX dt\right]N_J^M=\bar{T}_i^M, \qquad \text{on } [t_1^M,t_2^M]\times\partial B_{0,2}
\end{aligned}$$

Under constant body forces in time , the equations simplify to

$$\begin{aligned}
&\tfrac{d}{dt^M}\left(\rho_0^M\mathbf{V}^M\right)-\nabla^M\mathbf{P}^M=\rho_0^M\mathbf{B}^M &&, \text{ in } [t_1^M,t_2^M]\times B_0^M\\
&\tfrac{1}{|B_0|}\int_{B_0}\rho_0\,dX=\rho_0^M &&, \text{ on } (\{t_1^M\}\cup\{t_2^M\})\times B_0^M\\
&\rho_0^M\mathbf{V}^M(t^M=t_1^M)=\rho_0^M\bar{\mathbf{V}}^{1M} &&, \text{ on } \{t_1^M\}\times B_0^M\\
&\rho_0^M\mathbf{V}^M(t^M=t_2^M)=\rho_0^M\bar{\mathbf{V}}^{2M} &&, \text{ on } \{t_2^M\}\times B_0^M\\
&\mathbf{P}^M N_J^M=\bar{\mathbf{T}}^M &&, \text{ on } [t_1^M,t_2^M]\times\partial B_{0,2}
\end{aligned}$$

where the macroscopic stress tensor and macroscopic body forces are identified with

$$\mathbf{P}^M=\frac{1}{|\Omega_0|}\int_{\Omega_0}\left(\mathbf{P}-\rho_0\mathbf{B}\otimes\mathbf{X}\right)\,dX\,dt \tag{3.71}$$

$$\rho_0^M\mathbf{B}^M=\frac{1}{|\Omega_0|}\int_{\Omega_0}\rho_0\mathbf{B}\,dX\,dt \tag{3.72}$$

and the following relation has been used

$$\begin{aligned}
\frac{1}{|\Omega_0|}\int_{\Omega_0}\rho_0 V_i\,dXdt&=\frac{1}{|\Omega_0|}\int_{B_0}\int_{-\tau/2}^{\tau/2}\rho_0\varphi_{i,t}\,dX\,dt\\
&=\frac{1}{|\Omega_0|}\int_{B_0}\rho_0 V_i^M\tau\,dX\,dt=\rho_0^M V_i^M
\end{aligned} \tag{3.73}$$

These expressions can be simplified for the particular case of the hollow sphere of homogeneous material with constant body forces to

$$\mathbf{P}^M=\frac{1}{|\Omega_0|}\int_{\Omega_0}\mathbf{P}\,dX\,dt \tag{3.74}$$

$$\rho_0^M \mathbf{B}^M = \rho_0(1-f)\mathbf{B} \tag{3.75}$$

where $f$ is the void volume fraction.

An interesting conclusion that is obtained from these derivations is the fact that the instantaneous effect of the microscopic accelerations cancels out when averaged over time, in the event of separation of timescales.

## 3.4 Time discretization

In order to solve numerically the initial boundary value problem resulting from the multi-scale dynamic evolution of porous materials, the approach of Radovitzky and Ortiz (1999) is followed. The methodology consists of a two stage discretization. First the discretization in time is performed, under which an equivalent incremental static problem can be defined, and then the discretization in space is carried out. This initial time discretization allows the consideration of a wide variety of materials by use of an incremental energy density. Internal variables $\mathbf{Z}$ are used to describe the inelastic processes (Lubliner, 1973), such as viscoelasticity or plasticity, and the kinetic relations that provide the evolution law of such internal variables are assumed to derive from a potential. With these considerations, the incremental energy density at time $t_{n+1}$ is defined as

$$W(\mathbf{F}^{n+1};\mathbf{F}^n,\mathbf{Z}^n) = \min_{\mathbf{Z}^{n+1}} \left[ A(\mathbf{F}^{n+1},\mathbf{Z}^{n+1}) - A(\mathbf{F}^n,\mathbf{Z}^n) + \Delta t \psi^* \left( \frac{\mathbf{Z}^{n+1}-\mathbf{Z}^n}{\Delta t}, \mathbf{Z}^n \right) \right] + \Delta t \phi \left( \frac{\mathbf{F}^{n+1}-\mathbf{F}^n}{\Delta t}; \mathbf{F}^n \right) \tag{3.76}$$

where $A(\mathbf{F},\mathbf{Z})$ is the Helmholtz free energy density, $\phi(\dot{\mathbf{F}},\mathbf{F})$ is the potential from which the viscosity stresses derive ($\mathbf{P}^v = \phi_{,\dot{\mathbf{F}}}$), and $\psi^*$ is the Legendre transform of the inelastic potential $\psi$, which provides the flow rule and rate equations attendant to the plastic process follow. In the case of hyperelastic materials $A = W(\mathbf{F})$ and the incremental energy density reduces to

$$W(\mathbf{F}^{n+1};\mathbf{F}^n) = A(\mathbf{F}^{n+1}) - A(\mathbf{F}^n) \tag{3.77}$$

By this procedure, the results obtained in the previous section for hyperelastic materials are readily applicable under discrete time to materials exhibiting internal processes such as viscoplastic materials.

In this section, the more general case in which no assumption is made on the micro and macro time scales is considered, the other case being analogous. Therefore, time is a common variable to the microstructure and the macroscopic material, and the temporal discretization is the same for both scales. The spatial discretization is discussed in Section

3.5.

The time discretization used is based in the theory of variational time integrators (see for example Lew et al. (2004)). The main idea behind this theory is the approximation of the action integral as a sum of discrete Lagrangians

$$\mathcal{A} = \int_{t_1}^{t_2} \mathcal{L}\, dt \approx \sum_{n=0}^{N-1} \mathcal{L}_n \tag{3.78}$$

from which the equations discretized in time are directly obtained. This type of time integrators has demonstrated great accuracy and superior conservation properties in comparison with standard time integration schemes.

For definiteness, Newmark's algorithm is used to obtain the solution at times $t_0, ..., t_n, t_{n+1} = t_n + \Delta t, ...$ (Newmark, 1959). This scheme derives from a discrete Lagrangian for the Newmark parameter $\gamma = \frac{1}{2}$ and any $\beta$ (Kane et al., 2000).

$$\begin{aligned}
\boldsymbol{\varphi}^{n+1} &= \boldsymbol{\varphi}^n + \Delta t \dot{\boldsymbol{\varphi}}^n + \Delta t^2 \left[(1/2 - \beta)\ddot{\boldsymbol{\varphi}}^n + \beta \ddot{\boldsymbol{\varphi}}^{n+1}\right] \\
\dot{\boldsymbol{\varphi}}^{n+1} &= \dot{\boldsymbol{\varphi}}^n + \Delta t \left[(1-\gamma)\ddot{\boldsymbol{\varphi}}^n + \gamma \ddot{\boldsymbol{\varphi}}^{n+1}\right] \\
\rho_0 \ddot{\boldsymbol{\varphi}}^{n+1} - \nabla \cdot \mathbf{P}^{n+1} &= \rho_0 \mathbf{B}^{n+1}
\end{aligned} \tag{3.79}$$

For the particular case where $\beta = 0$, the method becomes explicit. Both the explicit case and the implicit are treated in the following subsections.

### 3.4.1 Implicit dynamics

Equations 3.79 can be rearranged to obtain the following static problem

$$\frac{\rho_0}{\beta \Delta t^2} \boldsymbol{\varphi}^{n+1} - \nabla \cdot \mathbf{P}^{n+1} = \rho_0 \bar{\mathbf{B}}^{n+1} \tag{3.80}$$

where $\bar{\mathbf{B}}$ is the effective body force field.

$$\bar{\mathbf{B}}^{n+1} = \mathbf{B}^{n+1} + \frac{1}{\beta \Delta t^2}[\boldsymbol{\varphi}^n + \Delta t \dot{\boldsymbol{\varphi}}^n + (1/2 - \beta)\Delta t^2 \ddot{\boldsymbol{\varphi}}^n] \tag{3.81}$$

Radovitzky and Ortiz (1999) reformulated this static problem, resulting from the time discretization via Newmark's algorithm, as the minimum of the following potential energy:

$$\begin{aligned}\Pi[\boldsymbol{\varphi}^{n+1}(\cdot)] = &\int_{B_0} \left[\frac{1}{2}\frac{\rho_0}{\beta\Delta t^2}|\boldsymbol{\varphi}^{n+1}|^2 + W(\nabla\boldsymbol{\varphi}^{n+1})\right] dV_0 \\ &- \int_{B_0} \rho_0 \bar{\mathbf{B}}^{n+1}\cdot\boldsymbol{\varphi}^{n+1}\, dX - \int_{\partial B_{02}} \bar{T}^{n+1}\cdot\boldsymbol{\varphi}^{n+1}\, dX\end{aligned} \tag{3.82}$$

provided the constitutive update of the internal variables, if present, posseses a potential structure.

Based on this variational structure, spatial averaging of the microscopic potential energy at equilibrium can be performed to obtain the macroscopic potential at the same time step. It is of note that essential boundary conditions are assumed on the external surface of our representative volume element, and therefore the last term attendant to the imposed tractions is not present at micro level. The macroscopic potential energy then follows as

$$\Pi^M[\boldsymbol{\varphi}^{M,n+1}(\cdot)] = \int_{B_0^M} \frac{1}{|B_0|}\Pi[\boldsymbol{\varphi}]\, dX^M - \int_{\partial B_{02}^M} \bar{T}^{M,n+1}\cdot\boldsymbol{\varphi}^{M,n+1}\, dX^M \tag{3.83}$$

Following the same strategy as in the continuous setting, the variations of the microscopic potential energy with respect to the macroscopic quantities are computed

$$\begin{aligned}\delta\Pi &= \int_{B_0}\left[\frac{\rho_0}{\beta\Delta t^2}\boldsymbol{\varphi}^{n+1}\cdot\delta\boldsymbol{\varphi}^{n+1} + \mathbf{P}^{n+1} : \delta\nabla\boldsymbol{\varphi}^{n+1} - \rho_0\bar{\mathbf{B}}^{n+1}\cdot\delta\boldsymbol{\varphi}^{n+1}\right] dX \\ &= \int_{B_0}\left[\frac{\rho_0}{\beta\Delta t^2}\boldsymbol{\varphi}^{n+1} - \nabla\cdot\mathbf{P}^{n+1} - \rho_0\bar{\mathbf{B}}^{n+1}\right]\cdot\delta\boldsymbol{\varphi}^{n+1}\, dX \\ &\quad + \int_{\partial B_0}\mathbf{T}^{n+1}\cdot\delta\boldsymbol{\varphi}^{n+1}\, dX \\ &= \left[\int_{\partial B_0}\mathbf{T}^{n+1}\, dX\right]\cdot\delta\boldsymbol{\varphi}^{M,n+1} + \left[\int_{\partial B_0}\mathbf{T}^{n+1}\otimes X\, dX\right] : \delta\nabla^M\boldsymbol{\varphi}^{M,n+1} \\ &= \left[\int_{B_0}\nabla\cdot\mathbf{P}^{n+1}\, dX\right]\cdot\delta\boldsymbol{\varphi}^{M,n+1} + \left[\int_{B_0}\mathbf{P}^{n+1} + \nabla\cdot\mathbf{P}^{n+1}\otimes X\, dX\right] : \delta\nabla^M\boldsymbol{\varphi}^{M,n+1}\end{aligned} \tag{3.84}$$

$$\frac{\partial\Pi}{\partial\boldsymbol{\varphi}^{M,n+1}} = \int_{B_0}\frac{\rho_0}{\beta\Delta t^2}\boldsymbol{\varphi}^{n+1}\, dX - \int_{B_0}\rho_0\bar{\mathbf{B}}^{n+1}\, dX \tag{3.85}$$

$$\begin{aligned}\frac{\partial \Pi}{\partial \nabla^M \boldsymbol{\varphi}^{M,n+1}} &= \int_{B_0} \left[ \mathbf{P}^{n+1} + \left( \frac{\rho_0}{\beta \Delta t^2} \boldsymbol{\varphi}^{n+1} - \rho_0 \bar{\mathbf{B}}^{n+1} \right) \otimes X \right] dX \\ &= \int_{B_0} \left[ \mathbf{P}^{n+1} + \left( \rho_0 \ddot{\boldsymbol{\varphi}}^{n+1} - \rho_0 \mathbf{B}^{n+1} \right) \otimes X \right] dX \end{aligned} \tag{3.86}$$

By taking variations of the macroscopic potential energy

$$\begin{aligned}\delta \Pi^M = &\int_{B_0^M} \left[ \left( \frac{1}{|B_0|} \frac{\partial \Pi}{\partial \boldsymbol{\varphi}^{M,n+1}} \right) - \nabla^M \cdot \left( \frac{1}{|B_0|} \frac{\partial \Pi}{\partial \nabla^M \boldsymbol{\varphi}^{M,n+1}} \right) \right] \cdot \delta \boldsymbol{\varphi}^{M,n+1} \, dX^M \\ &- \int_{\partial B_0^M 2} \left[ \bar{T}^{M,n+1} - \left( \frac{1}{|B_0|} \frac{\partial \Pi}{\partial \nabla^M \delta \boldsymbol{\varphi}^{M,n+1}} \right) \cdot \mathbf{N}^M \right] \cdot \delta \boldsymbol{\varphi}^{M,n+1} \, dX^M \end{aligned} \tag{3.87}$$

the corresponding balance equations and boundary conditions can be obtained

$$\begin{aligned}&\frac{1}{\beta \Delta t^2} \left[ \frac{1}{|B_0|} \int_{B_0} \rho_0 \boldsymbol{\varphi}^{n+1} \, dX \right] - \nabla^M \cdot \left[ \frac{1}{|B_0|} \int_{B_0} \left[ \mathbf{P}^{n+1} + \left( \rho_0 \ddot{\boldsymbol{\varphi}}^{n+1} - \rho_0 \mathbf{B}^{n+1} \right) \otimes \mathbf{X} \right] dX \right] \\ &\quad = \left[ \frac{1}{|B_0|} \int_{B_0} \rho_0 \bar{\mathbf{B}}^{n+1} \, dX \right], \qquad \text{in } B_0^M \end{aligned} \tag{3.88}$$

$$\left[ \frac{1}{|B_0|} \int_{B_0} \left( \mathbf{P}^{n+1} + \rho_0 (\ddot{\boldsymbol{\varphi}}^{n+1} - \mathbf{B}^{n+1}) \otimes \mathbf{X} \right) dX \right] \cdot \mathbf{N}^M = \bar{\mathbf{T}}^{M,n+1}, \qquad \text{on } \partial B_{0,2}^M \tag{3.89}$$

The macroscopic stresses can be identified as

$$\mathbf{P}^{M,n+1} = \frac{1}{|B_0|} \int_{B_0} \left( \mathbf{P}^{n+1} + \rho_0 (\ddot{\boldsymbol{\varphi}}^{n+1} - \mathbf{B}^{n+1}) \otimes \mathbf{X} \right) dX \tag{3.90}$$

which for the case of the hollow sphere of homogeneous material under constant body forces reduces to

$$\mathbf{P}^{M,n+1} = \frac{1}{|B_0|} \int_{B_0} (\mathbf{P}^{n+1} + \rho_0 \ddot{\boldsymbol{\varphi}}^{n+1} \otimes \mathbf{X}) \, dX \tag{3.91}$$

The expected result in the discrete setting is therefore recovered.

### 3.4.2 Explicit dynamics

For the case in which $\beta = 0$, the explicit discretized equilibrium equations become

$$\frac{2\rho_0}{\Delta t^2}\left(\boldsymbol{\varphi}^{n+1} - \boldsymbol{\varphi}^{n+1,\text{pre}}\right) - \nabla \cdot \mathbf{P}^n - \rho_0 \mathbf{B}^n = 0 \tag{3.92}$$

where $\boldsymbol{\varphi}^{n+1,\text{pre}} = \boldsymbol{\varphi}^n + \Delta t \dot{\boldsymbol{\varphi}}^n$. The equations can also be written in variational form, as the stationary point of the following potential energy

$$\Pi[\boldsymbol{\varphi}^{n+1}(\cdot)] = \int_{B_0} \left[\rho_0 \frac{|\boldsymbol{\varphi}^{n+1} - \boldsymbol{\varphi}^{n+1,\text{pre}}|^2}{\Delta t^2} + \mathbf{P}^n : \nabla \boldsymbol{\varphi}^{n+1} - \rho_0 \mathbf{B}^n \cdot \boldsymbol{\varphi}^{n+1}\right] dX \tag{3.93}$$

Similarly to the static continuous derivations, the macroscopic potential energy reads

$$\Pi^M[\boldsymbol{\varphi}^{M,n+1}(\cdot)] = \int_{B_0^M} \frac{1}{|B_0|}\Pi[\boldsymbol{\varphi}]\, dX^M - \int_{\partial B_{02}^M} \bar{T}^{M,n+1} \cdot \boldsymbol{\varphi}^{M,n+1}\, dX^M \tag{3.94}$$

By taking variations of the microscopic potential energy with respect to the macroscopic quantities

$$\begin{aligned}
\delta\Pi &= \int_{B_0} \left[2\rho_0 \frac{\boldsymbol{\varphi}^{n+1} - \boldsymbol{\varphi}^{n+1,\text{pre}}}{\Delta t^2} \cdot \delta\boldsymbol{\varphi}^{n+1} + \mathbf{P}^n : \delta\nabla\boldsymbol{\varphi}^{n+1} - \rho_0 \bar{\mathbf{B}}^n \cdot \delta\boldsymbol{\varphi}^{n+1}\right] dX \\
&= \int_{B_0} \left[2\rho_0 \frac{\boldsymbol{\varphi}^{n+1} - \boldsymbol{\varphi}^{n+1,\text{pre}}}{\Delta t^2} - \nabla \cdot \mathbf{P}^n - \rho_0 \bar{\mathbf{B}}^n\right] \cdot \delta\boldsymbol{\varphi}^{n+1}\, dX \\
&\quad + \int_{\partial B_0} \mathbf{T}^n \cdot \delta\boldsymbol{\varphi}^{n+1}\, dX \\
&= \left[\int_{\partial B_0} \mathbf{T}^n\, dX\right] \cdot \delta\boldsymbol{\varphi}^{M,n+1} + \left[\int_{\partial B_0} \mathbf{T}^n \otimes X\, dX\right] : \delta\nabla^M \boldsymbol{\varphi}^{M,n+1} \\
&= \left[\int_{B_0} \nabla \cdot \mathbf{P}^n\, dX\right] \cdot \delta\boldsymbol{\varphi}^{M,n+1} + \left[\int_{B_0} \mathbf{P}^n + \nabla \cdot \mathbf{P}^n \otimes X\, dX\right] : \delta\nabla^M \boldsymbol{\varphi}^{M,n+1}
\end{aligned} \tag{3.95}$$

the following relations are obtained

$$\frac{\partial \Pi}{\partial \boldsymbol{\varphi}^{M,n+1}} = \int_{B_0} 2\rho_0 \frac{\boldsymbol{\varphi}^{n+1} - \boldsymbol{\varphi}^{n+1,\text{pre}}}{\Delta t^2}\, dX - \int_{B_0} \rho_0 \bar{\mathbf{B}}^n\, dX \tag{3.96}$$

$$\frac{\partial \Pi}{\partial \nabla^M \boldsymbol{\varphi}^{M,n+1}} = \int_{B_0} \left[\mathbf{P}^n + \rho_0 \left(2\frac{\boldsymbol{\varphi}^{n+1} - \boldsymbol{\varphi}^{n+1,\text{pre}}}{\Delta t^2} - \bar{\mathbf{B}}^n\right) \otimes \mathbf{X}\right] dX \tag{3.97}$$

Rendering the macroscopic potential energy stationary results in the Euler-Lagrange equations of the motion of the macroscopic body

$$\begin{aligned}
&\left[\frac{1}{|B_0|}\int_{B_0} 2\rho_0 \frac{\boldsymbol{\varphi}^{n+1}-\boldsymbol{\varphi}^{n+1,\mathrm{pre}}}{\Delta t^2}\, dX\right] - \\
&\quad \nabla^M \cdot \left\{ \frac{1}{|B_0|}\int_{B_0} \left[\mathbf{P}^n + \rho_0 \left(2\frac{\boldsymbol{\varphi}^{n+1}-\boldsymbol{\varphi}^{n+1,\mathrm{pre}}}{\Delta t^2} - \bar{\mathbf{B}}^n\right)\otimes \mathbf{X}\right] dX \right\} \\
&\quad = \left[\frac{1}{|B_0|}\int_{B_0} \rho_0 \bar{\mathbf{B}}^n\, dX\right], \qquad \text{in } B_0^M
\end{aligned} \tag{3.98}$$

$$\left[\frac{1}{|B_0|}\int_{B_0} \left(\mathbf{P}^n + \rho_0 \left(2\frac{\boldsymbol{\varphi}^{n+1}-\boldsymbol{\varphi}^{n+1,\mathrm{pre}}}{\Delta t^2} - \bar{\mathbf{B}}^n\right)\otimes \mathbf{X}\right) dX\right]\cdot \mathbf{N}^M = \bar{\mathbf{T}}^{M,n+1}, \qquad \text{on } \partial B_{0,2}^M \tag{3.99}$$

The macroscopic stresses can be identified as

$$\mathbf{P}^{M,n+1} = \frac{1}{|B_0|}\int_{B_0} \left[\mathbf{P}^n + \rho_0 \left(2\frac{\boldsymbol{\varphi}^{n+1}-\boldsymbol{\varphi}^{n+1,\mathrm{pre}}}{\Delta t^2} - \bar{\mathbf{B}}^n\right)\otimes \mathbf{X}\right] dX \tag{3.100}$$

recovering again the expected result.

## 3.5 Spatial discretization of the hollow sphere

The solution of a boundary value problem defined on a hollow sphere cannot be obtained in a closed analytical form except in very simplified situations. The central objective of this section is to develop an efficient method of discretization adapted to the analysis of hollow spheres enabling consideration of general materials and loading conditions.

To resolve the fields in space, a Ritz-Galerkin method is adopted (Brenner and Scott, 2000). The specific approximation space that is employed relies on the use of local spherical coordinates. Piecewise polynomials are used for the interpolation of the radial dependence of the fields and real spherical harmonics for the angular dependence (Sansone, 1959). The final position in cartesian coordinates of a material point of coordinates $(R, \Theta, \Phi)$ is approximated by

$$x_i(R,\Theta,\Phi) = \sum_a x_{ia} N_a(R,\Theta,\Phi) = \sum_{r=0}^{N_r} \sum_{l=0}^{N_l} \sum_{m=-l}^{l} x_{irlm} R_r(R) Y_{lm}(\Theta,\Phi) \tag{3.101}$$

where $N_a$ is the shape function corresponding to coefficient $a$, and $x_a$ is the value of such coefficient. By the multiplicative decomposition of the shape function according to the method of separation of variables, the final discretization of the sphere results in an ensemble of spherical shell layers. The position of each layer is readily determined by the $\delta$-Kronecker property of the radial shape functions, while inside each individual layer, the coefficients $x_a$ do not represent the displacement of any particular material point. Each coefficient $x_a$ is identified with a triplet of integers $[r, l, m]$. The first integer is indicative of the spherical shell while the other two define the shape function $Y_{lm}$ (real spherical harmonics) over the surface of the layer.

A similar interpolation can be used for the displacement field in linearized kinematics, which will be carried out for numerical verification purposes. The derivations here presented are limited though to the finite strain formulation, which is the case of interest.

The real spherical harmonics have the following expression (Sansone, 1959)

$$Y_{lm}(\Theta,\Phi) = \begin{cases} N_{l0} P_l^0(\cos\Theta) & m = 0 \\ \sqrt{2} N_{lm} P_l^m(\cos\Theta)\cos(m\Phi) & m > 0 \\ \sqrt{2} N_{l|m|} P_l^{|m|}(\cos\Theta)\sin(|m|\Phi) & m < 0 \end{cases}$$

where $P_l^m$ are the associated Legendre functions and

$$N_{lm} = \sqrt{\frac{(2l+1)}{4\pi}\frac{(l-m)!}{(l+m)!}} \tag{3.102}$$

Real spherical harmonics constitute a complete orthogonal basis of the Hilbert space of square-integrable functions on the sphere (Sansone, 1959), which is an essential property for the formulation

$$\int_{\Theta=0}^{\pi}\int_{\Phi=0}^{2\pi} Y_{lm}Y_{l'm'}\sin\Theta d\Theta d\Phi = \delta_{ll'}\delta_{mm'} \tag{3.103}$$

In addition, finite rotations are exactly represented within the interpolation, which results in material-frame indifference and preserves the symmetry groups of the material. By contrast, a conventional finite-element discretization breaks material symmetries in general. This result is based on the following rotation property of the spherical harmonics (Byerly, 1893, Su and Coppens, 1994)

$$Y_{lm}(\Theta',\Phi') = \sum_{m'=-l}^{l} Y_{lm'}(\Theta,\Phi)D_{m'm}(\alpha,\beta,\gamma) \tag{3.104}$$

where $D_{m'm}$ is a matrix that depends on the rotation, represented for example by means of the Euler angles $\alpha$, $\beta$ and $\gamma$.

In Fig. 3.6, different final configurations that can be obtained with the spherical harmonics representation are shown. The deformation mapping results in a translation of the undeformed configuration for degree $l = 0$ and in an affine transformation for degree $l = 1$. Higher values of the degree lead to less intuitive deformations.

The number of degrees of freedom of the proposed discretization, as a function of the number of layers in the radial direction $N_r$ and the order of the expansion in the spherical harmonics $N_l$, is shown in Fig. 3.7

Typical meshes that are used in the computations involve an expansion of the spherical harmonics of degree 1 or 3, which allow representation of the deformation within each layer with only 4 and 7 nodes, respectively. Similar numbers of degrees of freedom for more standard finite elements would lead to a discrete representation of the deformed spherical surface by a tetrahedron or a cube.

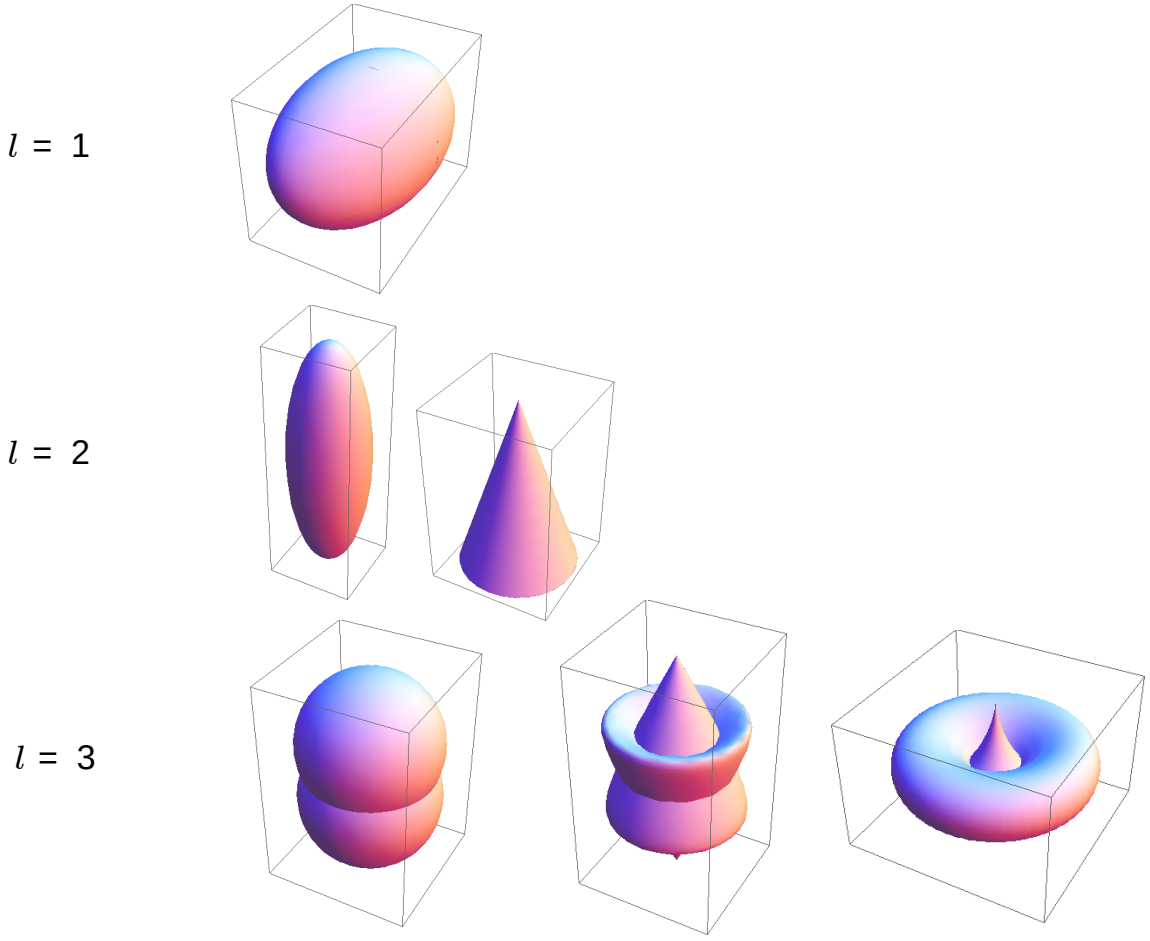


Figure 3.6: Examples of deformed shapes that can be obtained through a spherical harmonic expansion of the displacement field until degree $l$.

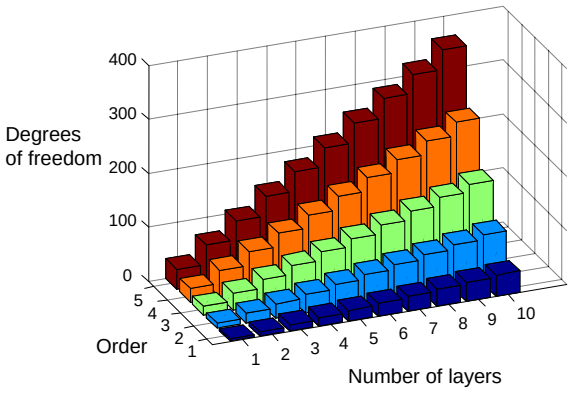


Figure 3.7: Number of degrees of freedom of the finite element formulation of the hollow sphere as a function of the number of layers in the radial direction and the order of the expansion in spherical harmonics.

### 3.5.1 Boundary conditions

The spherical harmonics do not have the Kronecker-$\delta$ property. However, an explicit analytical expression of the coefficients of the external layer as a function of the macroscopic deformation mapping $\boldsymbol{\varphi}^M$ and deformation gradient $\mathbf{F}^M$ is derived. As can be seen, affine boundary conditions, which are the ones of interest (see Eq. 3.9), can be represented exactly by using coefficients solely related to the spherical harmonics of degree 0 and 1. These expressions are here provided

$$x_{irlm} = \begin{cases} \sqrt{4\pi}\varphi_i^M & [r,l,m] = [N_r,0,0] \\ -\sqrt{\frac{4\pi}{3}}b\ F_{i2}^M & [r,l,m] = [N_r,1,-1] \\ \sqrt{\frac{4\pi}{3}}b\ F_{i3}^M & [r,l,m] = [N_r,1,0] \\ -\sqrt{\frac{4\pi}{3}}b\ F_{i1}^M & [r,l,m] = [N_r,1,1] \\ 0 & \text{otherwise} \end{cases}$$

By uniqueness of the values of the coefficients, a forward proof suffices to show that the above values of the coefficients recover the boundary conditions exactly. The derivation makes use of the Kronecker-$\delta$ property of the radial shape functions and the orthogonality of the spherical harmonics.

$$\begin{aligned} x_i(b,\Theta,\Phi) &= x_{iN_r00}Y_{00} + x_{iN_r1-1}Y_{1-1} + x_{iN_r10}Y_{10} + x_{iN_r11}Y_{11} \\ &= \varphi_i^M P_0^0(\cos\Theta) - bF_{i2}^M P_1^1(\cos\Theta)\sin\Phi + bF_{i3}^M P_1^0(\cos\Theta) - bF_{i1}^M P_1^1(\cos\Theta)\cos\Phi \\ &= \varphi_i^M + F_{i2}^M b\sin\Theta\sin\Phi + F_{i3}^M b\cos\Theta + F_{i1}^M b\sin\Theta\cos\Phi \\ &= \varphi_i^M + F_{ij}^M X_j(b,\Theta,\Phi) \end{aligned} \tag{3.105}$$

### 3.5.2 Quadrature rule

In order to perform numerical evaluations over the hollow sphere, a special quadrature rule that provides exact integration of the stiffness matrix, the mass matrix and the void volume fraction has been developed. The proposed integration scheme consists of the cartesian product of three quadrature rules, one for each of the three directions in spherical coordinates.

- For the radial direction ($R$), the usual Gauss Legendre quadrature rule is used to integrate polynomials exactly (Stroud, 1974).

- For the azimuthal direction ($\Phi$), equally spaced quadrature points with even weights are employed. This quadrature rule is exact for trigonometric polynomials in the interval $[0,\, 2\pi]$, due to the discrete orthogonality of the exponentials (Stroud, 1974).

$$\int_0^{2\pi} e^{im\Phi} d\Phi = \frac{2\pi}{n} \sum_{k=0}^{n-1} e^{\frac{2\pi i k m}{n}}, \quad |m| < n \tag{3.106}$$

- For the polar angle ($\Theta$), a Gauss Legendre quadrature rule under the transformation $x = \cos\theta$ is used. This quadrature rule cannot integrate exactly all associated Legendre functions in the polar direction over the interval $[0,\, \pi]$. However, the cartesian product of the three quadrature rules gives exact integration of the stiffness matrix, mass matrix and void volume fraction. The proof is based on the observation that when integration along the polar coordinate is not exact, integration over the azimuthal direction results in a zero value. The details of the proof can be found in appendices A, B and C.1.

The number of quadrature points needed along each coordinate for exact integration of the stiffness matrix is

$$\begin{aligned} N_{qr} &= 2N_r \\ N_{q\Theta} &= N_l + 2 \\ N_{q\Phi} &= 2N_l + 3 \end{aligned} \tag{3.107}$$

where the use of piecewise linear shape functions for the radial direction has been assumed. $N_r$ is the number of elements in the radial direction and $N_l$ the highest degree of the

spherical harmonics employed in the expansion. If polynomials of degree $d$ were to be used in the radial direction, a total number of quadrature points $N_{qr} \geq N_r \frac{d+1}{2}$ would be required for exact integration.

On the other hand, exact integration of the mass matrix requires

$$\begin{aligned} N_{qr} &= 3N_r \\ N_{q\Theta} &= N_l + 1 \\ N_{q\Phi} &= 2N_l + 1 \end{aligned} \tag{3.108}$$

and exact integration of the void volume fraction demands

$$\begin{aligned} N_{q\Theta} &\geq \frac{3N_l}{2} \\ N_{q\Phi} &= 3N_l + 1 \end{aligned} \tag{3.109}$$

### 3.5.3 Elastic moduli

If an implicit method is used for the time discretization or if a static problem is to be solved, it is then desirable to have an expression of the macro-tangent moduli in order to use non-linear solvers such as Newton-Raphson. In the following, an exact formula of the tangent moduli is provided for the static case under no body forces. It is of note that Newton-Raphson can be used with an approximate tangent moduli, and therefore the obtained result is also of practical use under dynamic conditions. The derivation uses a similar strategy than the one employed by Ortiz and Stainier (1999).

In the discrete setting, the micro-energy is a function of a priori unknown coefficients $Q$ belonging to the interior of the RVE and the macro-deformation gradient $\mathbf{F}^M$ through the boundary conditions. Under sufficient differentiability, the degrees of freedom in equilibrium $Q^*$ satisfy

$$\frac{\partial W}{\partial \mathbf{Q}}(\mathbf{Q}^*, \mathbf{F}^M) = 0 \tag{3.110}$$

Therefore, the desired tangent moduli can be obtained as follows

$$\begin{aligned}\frac{d^2W^M}{d\mathbf{F}^M d\mathbf{F}^M} &= \frac{1}{|B_0|}\int_{B_0}\frac{d^2W}{d\mathbf{F}^M d\mathbf{F}^M}\,dX \\ &= \frac{1}{|B_0|}\int_{B_0}\frac{d}{d\mathbf{F}^M}\left[\frac{\partial W}{\partial \mathbf{Q}}\frac{\partial \mathbf{Q}^*}{\partial \mathbf{F}^M}+\frac{\partial W}{\partial \mathbf{F}^M}\right]dX \\ &= \frac{1}{|B_0|}\int_{B_0}\frac{d}{d\mathbf{F}^M}\left(\frac{\partial W}{\partial \mathbf{F}^M}\right)dX \\ &= \left[\frac{1}{|B_0|}\int_{B_0}\frac{\partial^2 W}{\partial \mathbf{Q}\partial \mathbf{F}^M}\,dX\right]\frac{\partial \mathbf{Q}^*}{\partial \mathbf{F}^M}+\left[\frac{1}{|B_0|}\int_{B_0}\frac{\partial^2 W}{\partial \mathbf{F}^M\partial \mathbf{F}^M}\,dX\right]\end{aligned} \tag{3.111}$$

By differentiating Eq. 3.110, the value of $\frac{\partial \mathbf{Q}^*}{\partial \mathbf{F}^M}$ can be obtained

$$\left[\frac{1}{|B_0|}\int_{B_0}\frac{\partial^2 W}{\partial \mathbf{Q}\partial \mathbf{Q}}\,dX\right]\frac{\partial \mathbf{Q}^*}{\partial \mathbf{F}^M}+\left[\frac{1}{|B_0|}\int_{B_0}\frac{\partial^2 W}{\partial \mathbf{F}^M\partial \mathbf{Q}}\,dX\right]=0 \tag{3.112}$$

leading to the desired final expression

$$\begin{aligned}\frac{d^2W^M}{d\mathbf{F}^M d\mathbf{F}^M} &= \left[\frac{1}{|B_0|}\int_{B_0}\frac{\partial^2 W}{\partial \mathbf{F}^M\partial \mathbf{F}^M}\,dX\right] \\ &-\left[\frac{1}{|B_0|}\int_{B_0}\frac{\partial^2 W}{\partial \mathbf{Q}\partial \mathbf{F}^M}\,dX\right]\left[\frac{1}{|B_0|}\int_{B_0}\frac{\partial^2 W}{\partial \mathbf{Q}\partial \mathbf{Q}}\,dX\right]^{-1}\left[\frac{1}{|B_0|}\int_{B_0}\frac{\partial^2 W}{\partial \mathbf{F}^M\partial \mathbf{Q}}\,dX\right]\end{aligned} \tag{3.113}$$

The required second derivatives can be obtained from the micro-tangent moduli

$$\begin{aligned}\frac{\partial^2 W}{\partial F^M_{iJ}\partial F^M_{kL}} &= \frac{\partial^2 W}{\partial F_{mM}\partial F_{nN}}\frac{\partial F_{mM}}{\partial F^M_{iJ}}\frac{\partial F_{nN}}{\partial F^M_{kL}} \\ \frac{\partial^2 W}{\partial Q_{ia}\partial F^M_{kL}} &= \frac{\partial^2 W}{\partial F_{mM}\partial F_{nN}}\frac{\partial F_{mM}}{\partial Q_{ia}}\frac{\partial F_{nN}}{\partial F^M_{kL}}\end{aligned} \tag{3.114}$$

where the subindex $a$ is associated with the coefficient $x_a$, $\frac{\partial F_{iJ}}{\partial Q_{ja}} = \delta_{ij}N_{a,J}$ and $\frac{\partial F_{iJ}}{\partial F^M_{kL}}$ can readily be derived from the boundary conditions (Eq. 3.5.1).

## 3.6 Verification

This section examines the convergence of the macroscopic energy derived from the hollow sphere model presented in the foregoing. Three cases for which an analytic solution is found are analyzed as well as three more general ones. In all the calculations shown, linear interpolation is used in the radial direction. The expected rate of convergence in such direction is then expected to be quadratic. It is noteworthy that the rate of convergence of the spherical harmonics is extremely fast, and that the global convergence rate of the method is controlled by the radial interpolation. Therefore, only convergence with respect to the number or radial elements is represented in the following. This suggests that using spectral interpolation in the radial direction might result in a super-convergent method. However, this enhancement is not pursued here due to the lack of the Kronecker-$\delta$ property of such shape functions and the desire to use the model for the volumetric expansion of porous plastic materials.

### 3.6.1 Static volumetric deformation of a porous Hookean material

The first case to be investigated is the volumetric deformation of a hollow sphere of Hookean isotropic material under static conditions. The analytic solution is first obtained and the convergence results follow.

#### 3.6.1.1 Analytic solution

By symmetry, the displacement field is of the form

$$\begin{aligned} u_1 &= f(R)X_1 \\ u_2 &= f(R)X_2 \\ u_3 &= f(R)X_3 \end{aligned} \tag{3.115}$$

where $R^2 = X_1^2 + X_2^2 + X_3^2$. This implies that the solution can be represented exactly with an expansion in spherical harmonics up to degree 1.

The equilibrium equations under static loading with no body forces are $\sigma_{ij,j} = 0$, where

$$\begin{aligned}\sigma_{ij} &= \lambda\varepsilon_{kk}\delta_{ij} + 2\mu\varepsilon_{ij} \\ \varepsilon_{ij} &= \frac{1}{2}(u_{i,j} + u_{j,i})\end{aligned} \tag{3.116}$$

for the material chosen. Under the kinematic assumption 3.115, the equilibrium equations reduce to

$$4f'(R) + f''(R)R = 0 \tag{3.117}$$

which has a general solution of the form

$$f(R) = A - \frac{1}{BR^3} \tag{3.118}$$

The constants $A$ and $B$ can be obtained by imposing stress free boundary conditions on the inner surface ($R = a$) and $u_R(R = b) = \bar{\epsilon}b$ on the outer surface

$$\begin{aligned}B &= \frac{1}{a^3\bar{\epsilon}}\left[1 - \frac{a^3}{b^3} - 3\frac{\lambda + 2\mu}{3\lambda + 2\mu}\right] \\ A &= \bar{\epsilon} + \frac{1}{Bb^3}\end{aligned} \tag{3.119}$$

The microscopic energy density can then be computed exactly by

$$W = \frac{1}{2}\lambda(Tr(\varepsilon))^2 + \mu\varepsilon_{ij}\varepsilon_{ij} = \frac{\lambda}{2}\left[3f(R) + f'(R)R\right]^2 + \mu\left[3f^2(R) + 2f(R)f'(R)R + f'^2(R)R^2\right] \tag{3.120}$$

and the corresponding macroscopic quantity by

$$W^M = \frac{1}{|B_0|}\int_{B_0} W\, dX = \left(1 - \frac{a^3}{b^3}\right)\left[9\frac{\lambda}{2}A^2 + 3\mu\left(A^2 + \frac{2}{B^2a^3b^3}\right)\right] \tag{3.121}$$

#### 3.6.1.2 Convergence analysis

In Fig. 3.8 the error of the macroscopic energy with respect to the analytic value just derived is represented against the number of nodes in the radial direction. The numerical values are computed using an expansion of degree 1 of the spherical harmonics, which was previously shown to be sufficient to represent exactly the volumetric deformation.

The linear fit to the points in the asymptotic regime indicates the expected quadratic convergence rate in the energy.

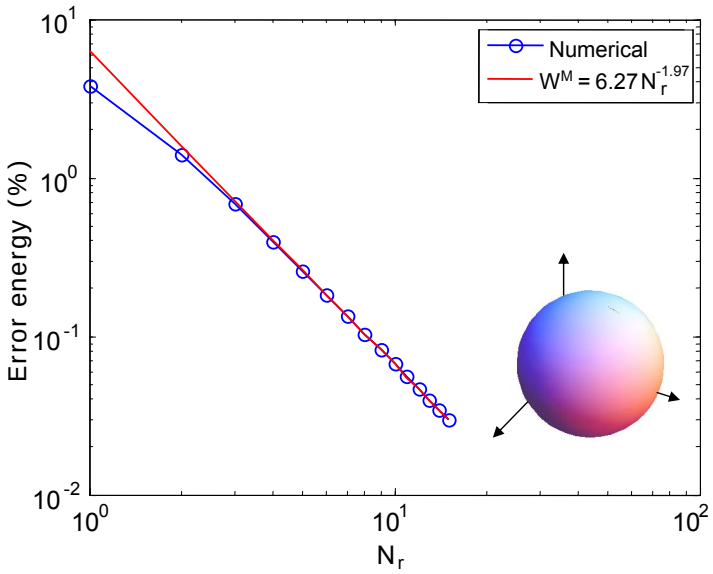


Figure 3.8: Error in the energy as a function of the number of elements in the radial direction. Parameters $a = 1, b = 2, \lambda = 1, \mu = 1, N_l = 1, \varepsilon_{11} = \varepsilon_{22} = \varepsilon_{33} = 0.05$

### 3.6.2 Static axisymmetric deformation of a porous Hookean material

The second case to be analyzed is the axisymmetric deformation of a hollow sphere of Hookean isotropic material, for which an analytic solution was also found.

#### 3.6.2.1 Analytic solution

Taking $X_3$ to be the axis of symmetry, the displacement field is expected to be of the form

$$\begin{aligned} u_R &= f(R)\cos^2\Theta + g(R)\sin^2\Theta \\ u_\Theta &= h(R)\sin\Theta\cos\Theta \\ u_\Phi &= 0 \end{aligned} \tag{3.122}$$

which in cartesian coordinates reads

$$\begin{aligned} u_1 &= \left[\frac{f(R)+h(R)}{R}\cos^2\Theta + \frac{g(R)}{R}\sin^2\Theta\right] X_1 \\ u_2 &= \left[\frac{f(R)+h(R)}{R}\cos^2\Theta + \frac{g(R)}{R}\sin^2\Theta\right] X_2 \\ u_3 &= \left[\frac{f(R)}{R}\cos^2\Theta + \frac{g(R)-h(R)}{R}\sin^2\Theta\right] X_3 \end{aligned} \tag{3.123}$$

The solution therefore only involves an expansion in spherical harmonics up to degree 3.

The linear independent equilibrium equations in spherical coordinates are

$$\begin{aligned} &\frac{\partial\sigma_{RR}}{\partial R} + \frac{1}{R}\frac{\partial\sigma_{R\Theta}}{\partial\Theta} + \frac{\cot\Theta}{R}\sigma_{R\Theta} + \frac{1}{R}(2\sigma_{RR} - \sigma_{\Theta\Theta} - \sigma_{\Phi\Phi}) = 0 \\ &\frac{\partial\sigma_{R\Theta}}{\partial R} + \frac{1}{R}\frac{\partial\sigma_{\Theta\Theta}}{\partial\Theta} + \frac{3}{R}\sigma_{R\Theta} + \frac{\cot\Theta}{R}(\sigma_{\Theta\Theta} - \sigma_{\Phi\Phi}) = 0 \end{aligned} \tag{3.124}$$

which provide three linearly independent equations for $f(R)$, $g(R)$ and $h(R)$

$$\begin{aligned} &\lambda\left[\frac{d^2f}{dR^2} + \frac{2}{R}\frac{df}{dR} - \frac{2}{R^2}f + \frac{2}{R}\frac{dh}{dR} - \frac{2}{R^2}h\right] + 2\mu\left[\frac{d^2f}{dR^2} + \frac{2}{R}\frac{df}{dR} + \frac{1}{R}\frac{dh}{dR} + \frac{2g-4f-3h}{R^2}\right] = 0 \\ &\lambda\left[\frac{d^2g}{dR^2} + \frac{2}{R}\frac{dg}{dR} - \frac{1}{R}\frac{dh}{dR} + \frac{h-2g}{R^2}\right] + 2\mu\left[\frac{d^2g}{dR^2} + \frac{2}{R}\frac{dg}{dR} - \frac{1}{2R}\frac{dh}{dR} + \frac{f-3g+3h/2}{R^2}\right] = 0 \\ &\frac{2\lambda}{R}\left[\frac{dg}{dR} - \frac{df}{dR} + \frac{2g-2f-3h}{R}\right] + \mu\left[\frac{d^2h}{dR^2} + \frac{2}{R}\frac{dh}{dR} + \frac{2}{R}\frac{dg}{dR} - \frac{2}{R}\frac{df}{dR} + \frac{8g-8f-12h}{R^2}\right] = 0 \end{aligned} \tag{3.125}$$

Stress free boundary conditions on the inner surface and displacement boundary conditions on the outer surface are applied

$$\begin{aligned} &\lambda\left(\frac{df}{dR} + \frac{2f+2h}{a}\right) + 2\mu\frac{df}{dR}\Big|_{R=a} = 0 \\ &\lambda\left(\frac{dg}{dR} + \frac{2g-h}{a}\right) + 2\mu\frac{dg}{dR}\Big|_{R=a} = 0 \\ &\frac{dh}{dR} + \frac{2g-2f-h}{a}\Big|_{R=a} = 0 \\ &f(b) = b\bar{\epsilon_2} \\ &g(b) = b\bar{\epsilon_1} \\ &h(b) = b(\bar{\epsilon_1} - \bar{\epsilon_2}) \end{aligned} \tag{3.126}$$

As expected, the equilibrium equations for the volumetric case are recovered when $\bar{\epsilon_1} = \bar{\epsilon_2}$. The effective energy density of the representative volume element can be computed with

$$W^M = \frac{1}{10b^3}(\lambda W_1^M + \mu W_2^M) \tag{3.127}$$

where

$$\begin{aligned} W_1^M = &\int_a^b R^2 \left[ 3\left(\frac{df}{dR} + \frac{2f}{R} + \frac{2h}{R}\right)^2 + 8\left(\frac{dg}{dR} + \frac{2g}{R} - \frac{h}{R}\right)^2 \right] dR \\ &+ \int_a^b R^2 \left[ 4\left(\frac{df}{dR} + \frac{2f}{R} + \frac{2h}{R}\right)\left(\frac{dg}{dR} + \frac{2g}{R} - \frac{h}{R}\right) \right] dR \\ W_2^M = &\int_a^b R^2 \left[ 6\left(\frac{df}{dR}\right)^2 + 16\left(\frac{dg}{dR}\right)^2 + 8\frac{df}{dR}\frac{dg}{dR} + 12\left(\frac{f+h}{R}\right)^2 + 16\left(\frac{g-h}{R}\right)^2 \right] dR \\ &+ \int_a^b R^2 \left[ 16\left(\frac{g}{R}\right)^2 + 8\frac{f+h}{R}\frac{2g-h}{R} + 2\left(\frac{dh}{dR} + \frac{2g}{R} - \frac{2f}{R} - \frac{h}{R}\right)^2 \right] dR \end{aligned} \tag{3.128}$$

#### 3.6.2.2 Convergence analysis

The convergence analysis is performed by using an expansion to degree 3 in the spherical harmonics and a varying number of nodes on the radial direction. The error in the energy with respect to the derived analytic energy, versus the number of spherical layers used in the radial discretization is represented in Fig. 3.9. The figure shows a convergence rate which is very close to quadratic.

### 3.6.3 Static volumetric deformation of a porous neo-Hookean material

The third analytically solvable problem presented here is the volumetric deformation of a hollow sphere of neo-Hookean material.

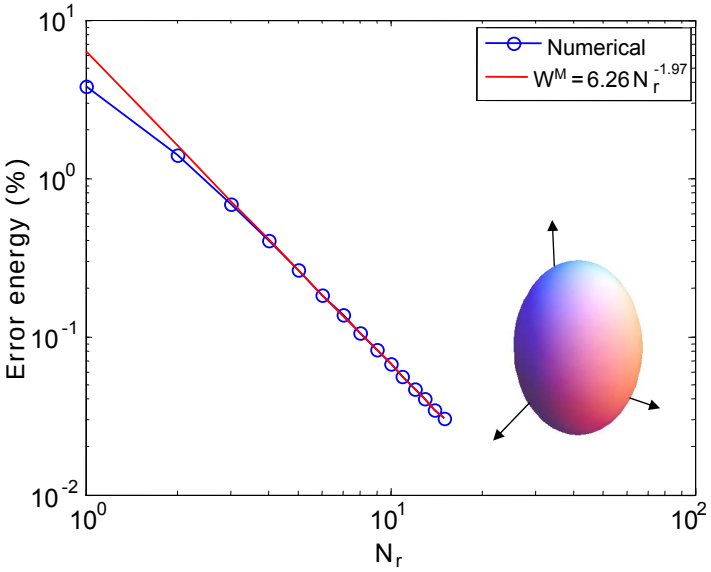


Figure 3.9: Error in the energy as a function of the number of elements in the radial direction. Parameters $a = 1, b = 2, \lambda = 1, \mu = 1, N_l = 3, \varepsilon_{11} = \varepsilon_{22} = 0.05, \varepsilon_{33} = 0.1$.

#### 3.6.3.1 Analytic solution

By symmetry, the deformation mapping is expected to be of the form

$$\begin{aligned} x_1 &= f(R)X_1 \\ x_2 &= f(R)X_2 \\ x_3 &= f(R)X_3 \end{aligned} \tag{3.129}$$

The constitutive equation used for the compressible neo-Hookean material is

$$P = (\lambda \ \log J - \mu)F^{-T} + \mu F \tag{3.130}$$

where $J = \det(F)$.

The equilibrium equation ($P_{iJ,J} = 0$) results, then, in

$$\left[(\lambda+\mu) - \lambda \ \log(f^3 + f^2 f' R)\right](4f^2 f' + 2ff'^2 R + f^2 f'' R)f^2 + \mu(f^3 + f^2 f' R)^2(4f' + f'' R) = 0 \tag{3.131}$$

Stress free boundary conditions on the inner surface and displacement boundary con-

ditions on the outer surface give

$$\begin{aligned} P_{11} &= \frac{\lambda \log[f^3(a) + f^2(a)f'(a)a] - \mu}{f^3(a) + f^2(a)f'(a)a} f^2(a) + \mu[f(a) + f'(a)a] = 0 \\ f(b) &= \bar{F} \end{aligned} \tag{3.132}$$

Once the function $f(R)$ has been computed, the macroscopic energy density is

$$W^M = \frac{1}{\frac{4}{3}\pi b^3} \int_a^b \int_0^\pi \int_0^{2\pi} W(R) R^2 \sin\Theta dR d\Theta d\Phi = \frac{3}{b^3} \int_a^b W(R) R^2 dR \tag{3.133}$$

with

$$\begin{aligned} W(R) &= \frac{1}{2}\lambda(\log J)^2 - \mu \log J + \frac{1}{2}\mu(\mathrm{Tr}C - 3) \\ &= \frac{1}{2}\lambda[\log(f^3 + f^2 f' R)]^2 - \mu \log(f^3 + f^2 f' R) + \frac{1}{2}\mu(3f^2 + f'^2 R^2 + 2ff'R - 3) \end{aligned} \tag{3.134}$$

#### 3.6.3.2 Convergence analysis

Convergence towards the analytic solution is shown in Fig. 3.10. The results indicate close to ideal convergence also for this nonlinear test case.

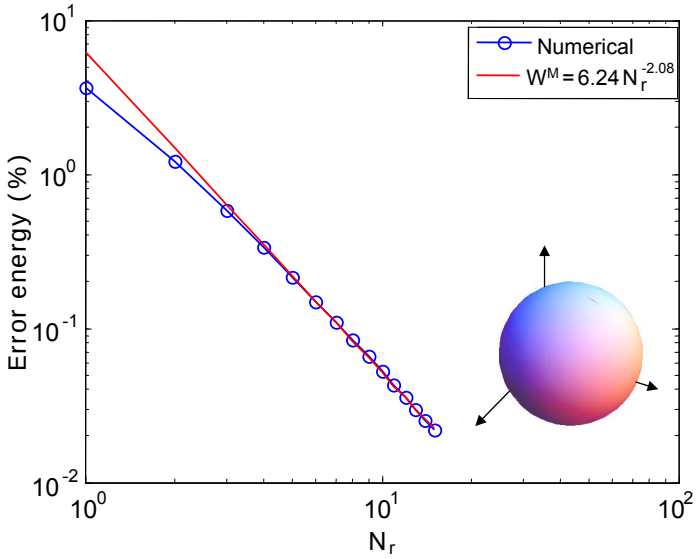


Figure 3.10: Error in the energy as a function of the number of elements in the radial direction. Parameters $a = 1, b = 2, \lambda = 1, \mu = 1, N_l = 1, F_{11} = F_{22} = F_{33} = 1.2$.

### 3.6.4 Static arbitrary deformation of a porous neo-Hookean material

The next case to be investigated is the arbitrary deformation of a porous neo-Hookean material. Fig. 3.11 shows the numerical results together with the fit in the asymptotic regime. Again, close to ideal convergence is recovered. The converged energy used for the computation of the error is a result from the fit.

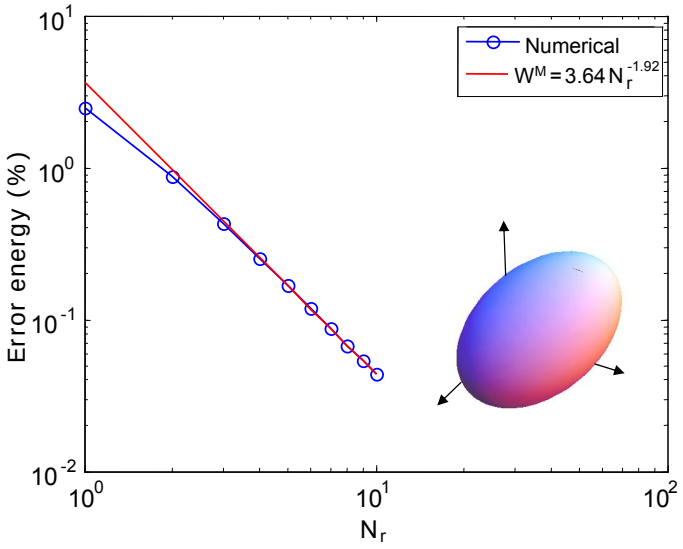


Figure 3.11: Error in the energy as a function of the number of elements in the radial direction. Parameters $a = 1, b = 2, \lambda = 1, \mu = 1, N_l = 5$, $F_{11} = 1.2, F_{12} = 0.1, F_{13} = 0.18, F_{21} = 0.2, F_{22} = 1.1, F_{23} = 0.21, F_{31} = 0.15, F_{32} = 0.3, F_{33} = 1.15$.

### 3.6.5 Static deformation of a porous J2-plastic material

The last static convergence analysis under static conditions is for a porous plastic material in the finite kinematic framework. In particular, aluminum with power law hardening and J2 isotropic plasticity law is used ($K = 67.5$ GPa, $\sigma_y = 276$ MPa, $n = 0.075$). An uniaxial deformation is applied to the hollow sphere. Fig. 3.12 shows close to quadratic convergence rate.

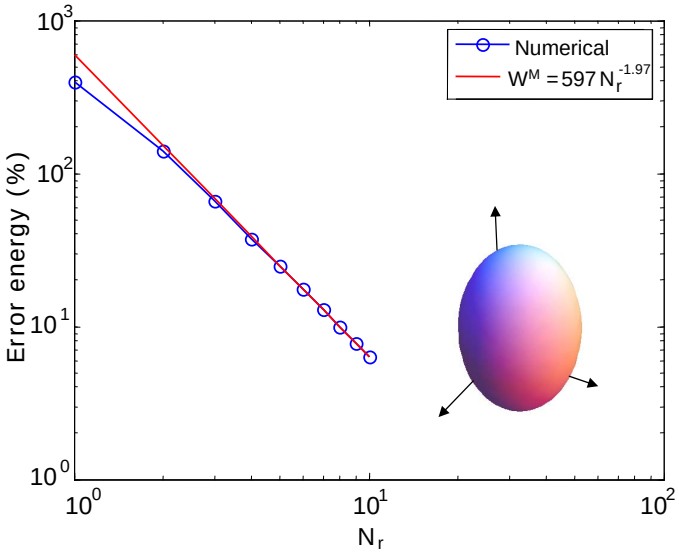


Figure 3.12: Error in the energy as a function of the number of elements in the radial direction. Parameters $a = 1, b = 2, N_l = 3$. Uniaxial deformation, $F_{11} = 1.2, F_{22} = 1.0, F_{33} = 1.0$.

### 3.6.6 Dynamic volumetric deformation of a porous neo-Hookean material. Explicit dynamics formulation.

In this section the convergence of the explicit dynamic code is examined both in time and space, without separation of temporal scales. The spherical expansion of a hollow sphere under a constant true strain rate with fixed origin is the test case considered.

In Fig. 3.13 the chosen time step is shown to provide convergent results, when compared with the solution obtained with a lower value of the time step. The time step was selected as to satisfy the CFL condition, necessary for convergence (Courant et al., 1928). In the event of volumetric deformation, the mesh size is unambiguous and given by the radial mesh size $h = \frac{b-a}{N_r}$.

The expansion is performed at a true strain rate of 650000 $s^{-1}$, and the material of choice is a neo-Hookean porous material with parameters listed in Table 3.1. It is of note that in dynamics the problem lacks scale invariance and both, the void volume fraction and the void size, are important parameters.

With a time step proportional to the CFL condition, and therefore to the mesh size, the number of elements in the radial direction is increased in order to obtain the correspondent convergence curve. Fig. 3.14 shows the expected rate of convergence.

Table 3.1: Material properties of the porous neo-Hookean material.

| $E$ (MPa) | $\nu$ | $a(\mu$ m) | $b(\mu$ m) | $\rho_0$ (kg/m$^3$) |
|---|---|---|---|---|
| 69 | 0.48 | 1 | 2 | 1104.72 |

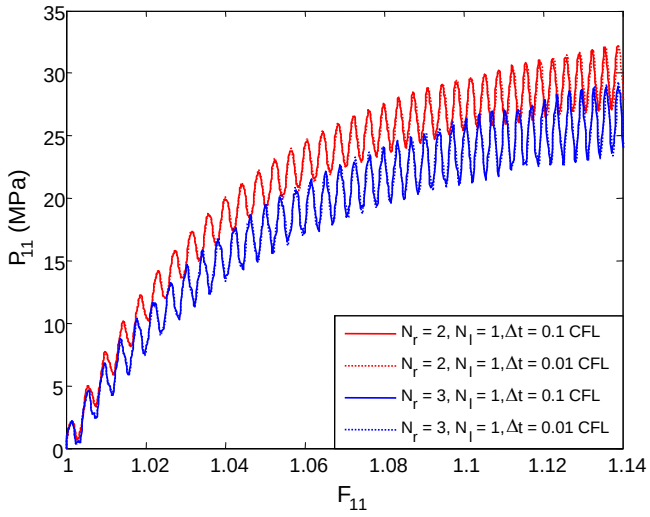


Figure 3.13: Stress-strain curve for a porous neo-Hookean material (Table 3.1) subjected to volumetric deformation. Comparison of two mesh sizes and two time steps.

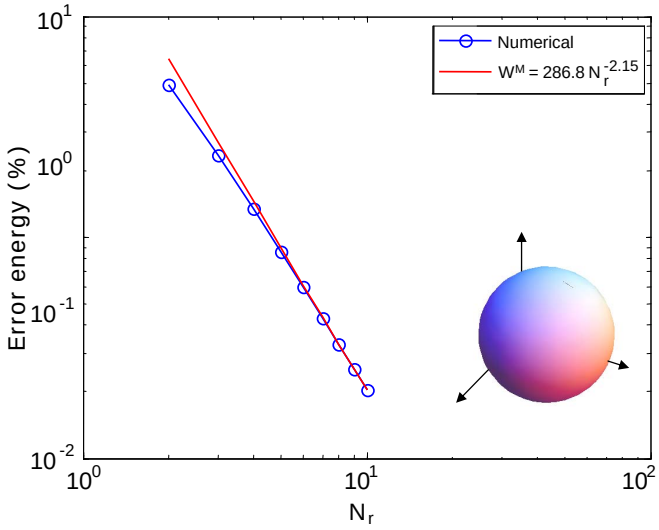


Figure 3.14: Error in the energy as a function of the number of elements in the radial direction. Spherical expansion, $F_{11} = F_{22} = F_{33} = 1.1$.

Due to the fact that the expansion is performed at constant true strain rate, the radial acceleration of the outer nodes is zero. Therefore, the acceleration of the inner material points is expected to oscillate around zero leading to a stress-strain curve that oscillates with respect to the static solution. Fig. 3.15 shows the material behavior for three different strain rates compared to the static definition of macroscopic stress. The oscillations have an amplitude that decreases, as expected, when the applied velocity is reduced. The material is assumed to be fully elastic, and therefore the oscillations do not decay with respect to time.

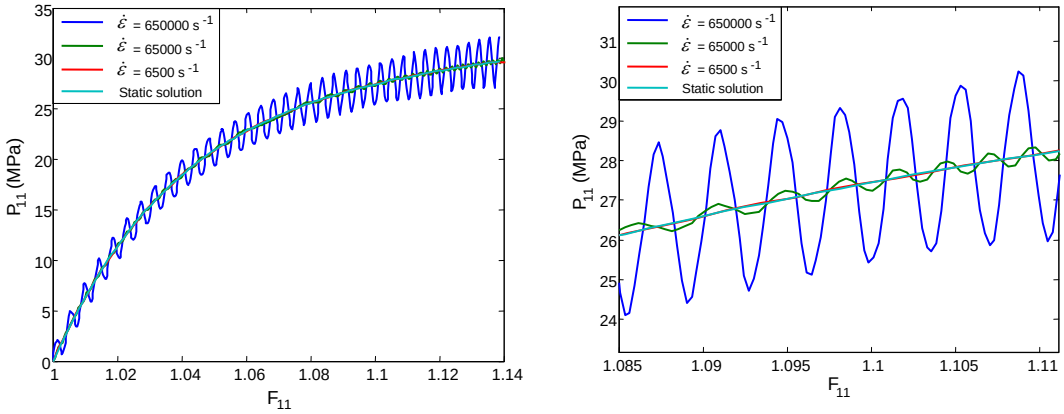


Figure 3.15: Material response under spherical expansion at constant strain rate. Comparison to static solution.

## 3.7 Material point calculations

In this section the influence of porosity in several materials under various types of loading is analyzed.

### 3.7.1 Static

First the static problem, which is characterized by scale invariance, will be considered. Therefore, the void volume fraction is the only quantity needed to identify the geometry of the problem.

#### 3.7.1.1 Elastic material

The process of sudden formation of voids, called cavitation, in rubber and elastomers has been the source of many studies. Experimentally Gent and Lindley (1958) observed the existence of a critical value of the hydrostatic tension above which cavitation occurs. The observed instability is attributed to the growth of preexistent defects in the material and is here shown numerically with the hollow sphere model. As a common hyperelastic model for rubber-like materials, a neo-Hookean material is used for the matrix of the hollow sphere. The following strain energy density for the compressible extension is used

$$W = \frac{\lambda}{2}(\log J)^2 - \mu \log J + \frac{1}{2}\mu(Tr(C) - 3) \tag{3.135}$$

leading to the following relation between the first Piola Kirchhoff stress tensor and the deformation gradient

$$\mathbf{P} = (\lambda \log J - \mu)\, \mathbf{F}^{-T} + \mu \mathbf{F} \tag{3.136}$$

The value of $\frac{\lambda}{\mu} = 24$ is chosen, which corresponds to an almost incompressible material with Poisson's ratio of $\nu = 0.48$.

The porous material response under varying initial void volume fraction is explored for several cases of monotonic loading: volumetric deformation, uniaxial strain, uniaxial stress and simple shear. It is of note that cavitation is not only dependent on the hydrostatic component of the load but it depends on the entire state of applied load (Chang et al.,

1993).

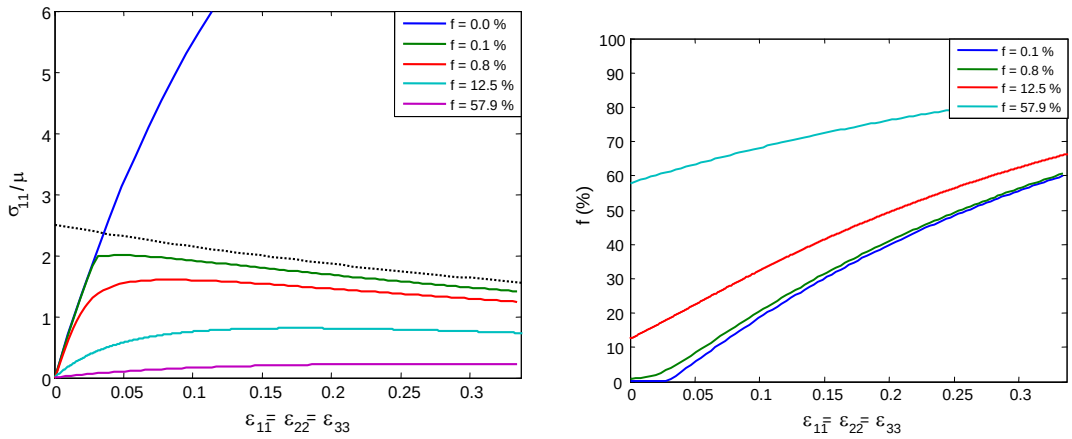


(a) (b)

Figure 3.16: Volumetric expansion response for different void volume fractions. The numerical solutions are obtained with $N_r = 10$ and $N_l = 1$. (a) Evolution of the pressure. (b) Evolution of the void volume fraction.

The results for the volumetric expansion are presented in Fig. 3.16. The true stress is represented versus the true strain. Computations are done though in the finite kinematic framework. As can be observed, the response of the material differs remarkably if one allows for the material to cavitate or not. The blue curve labeled as $f = 0.0\%$ represents the constitutive law for the non-porous neo-Hookean material considered (Eq. 3.7.1.1). The remaining continous curves correspond to the numerical solutions of the hollow sphere domain with non-vanishing initial void fraction, indicated in the legend. As expected, the material softens as the initial void volume fraction increases. A less intutitive fact is the existence of the critical pressure, reported experimentally, that the material can sustain. If this value is surpassed, the cavity would simply burst. In reality, cracks develop at the inner surface when the maximum extensibility of the rubber is attained (Gent, 1990). This phenonmenom becomes abrupt as the void volume fraction tends to zero (see Fig. 3.16(b)), and has mathematically been explained via a bifurcation model (Ball, 1982, Williams and Schapery, 1965, Chou-Wang and Horgan, 1989, Henao, 2009, Lopez-Pamies, 2009, Henao and Mora-Corral, 2010). See for example the review paper of Horgan and Polignone (1995). Physically, the bifurcation corresponds to a transition between the load being carried out by incompressibility (or quasi-incompressibility in our case) and the accommodation of the deformation by void growth. For an incompressible

material, the analytic solution for a finite void in an infinite medium, or equivalently, an infinitesimal void in a finite incompressible sphere (recall the scale invariance of the static problem), can easily be found (see for instance Henao (2009))

$$\frac{\sigma_{11}^M}{\mu} = \frac{2}{F_{11}^M} + \frac{1}{2(F_{11}^M)^4} \tag{3.137}$$

where $F_{11}^M = F_{22}^M = F_{33}^M$ by spherical symmetry, and $\sigma_{11}^M = \sigma_{22}^M = \sigma_{33}^M$. The well known critical value of the normalized stress $5/2$ is recovered at the origin.

The same numerical experiments for uniaxial strain, uniaxial stress and simple shear are shown in Fig. 3.17. Cavitation occurs, as expected, under uniaxial strain. The void volume fraction does not experience such a sudden increase under uniaxial stress or simple shear. However, its initial value plays a non-negligible softening role for high values of the void fraction.

#### 3.7.1.2 Plastic material

In the previous section it was highlighted that a critical pressure of value $\sigma_m^M/\mu = 5/2$, or equivalently $\sigma_m^M/E = 5/6$, would make an incompressible neo-Hookean material cavitate. A simple calculation indicates that a sphere of perfectly plastic material with an infinitesimal void would start yielding in the inner surface according to the von Mises criterion when $\sigma_m^M = \frac{2}{3}\sigma_Y$ (Lubliner, 1990). For the plastic material to cavitate elastically, the yield strength would therefore need to exceed the critical value $\sigma_Y/E = 5/4$. Engineering metals, though, have a Young's modulus that is several orders of magnitude higher than the yield strength, and therefore plasticity plays a crucial role in the growth of incipient voids. Cavitation in elastic-plastic solids has been studied by Huang et al. (1991) and Hou and Abeyaratne (1992) amongst others.

Similarly to the static case, the material response under several loading conditions is analyzed for several void volume fractions. Material properties of a typical aluminum (see Table 3.2) are used for the matrix of the hollow sphere, where $E$, $\nu$, $\sigma_Y$ and $n$ are, respectively, the Young's modulus, the Poisson's ration, the yield stress and the hardening exponent.

Fig. 3.18 shows the true stress versus true strain response under a volumetric expansion. Plasticity starts in the interior of the void and then propagates outwards. Only after

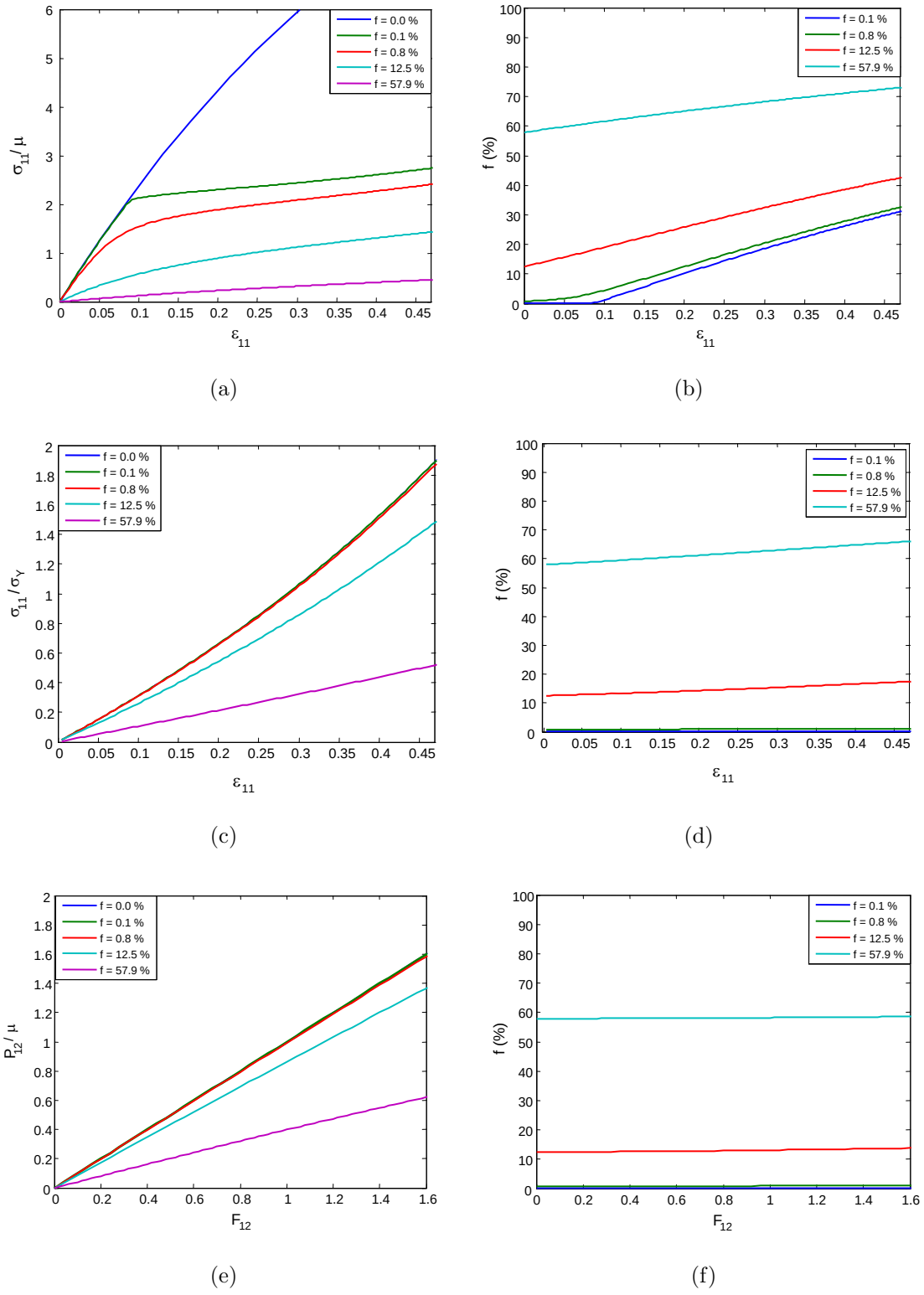


Figure 3.17: Response for different void volume fractions and different loading conditions. The numerical solutions are obtained with $N_r = 10$ and $N_l = 1$. (a) Uniaxial strain response. (b) Evolution of the void volume fraction under uniaxial strain. (c) Uniaxial stress response. (d) Evolution of the void volume fraction under uniaxial stress. (e) Simple shear response. (f) Evolution of the void volume fraction under simple shear.

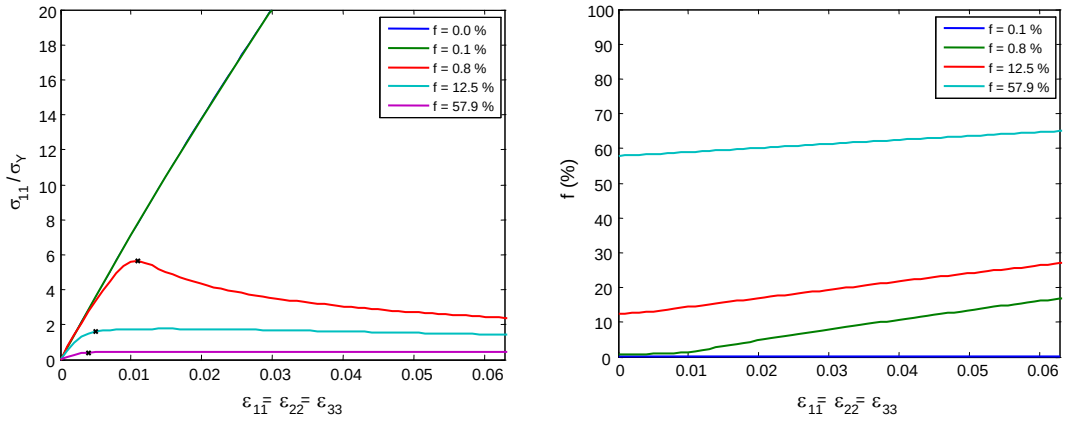


(a) (b)

Figure 3.18: Volumetric expansion response for different void volume fractions. The numerical solutions are obtained with $N_r = 10$ and $N_l = 1$. (a) Evolution of the pressure. (b) Evolution of the void volume fraction.

the hollow sphere becomes fully plastic (point indicated with an 'x' in the corresponding curves), it can expand with low stress. However, at this point, the void would be under the influence of the plastic zone of the neighboring void, and interaction between voids would become important. Such an influence cannot be captured by the present model in which a single cavity is considered, and another type of model would be more suitable to appropriately capture the last stage of growth and coalescence.

The material response under uniaxial strain, uniaxial stress and simple shear is shown in Fig. 3.19. As can be observed, the presence of voids has an important impact on the yield surface under all loading conditions. Particularly, volumetric stresses, which do not influence the yield of an undamaged material, produce yielding in the material when voids are present.

Gurson (1977a) provided an approximate analytical expression of the yield function for porous material with a rigid perfectly plastic matrix. Gurson's analytical expression is compared in the following with the yield locus determined numerically with the hollow sphere model. First, a rigid perfectly plastic material is used, and the macroscopic stresses leading to initial yield in the domain are shown in Fig. 3.20. Gurson's yield surface is represented in a continuous line, while the numerical computations of initial yield for different values of triaxiality are represented with discrete circles. The theoretical value of initial yield under volumetric deformation of the representative volume element can

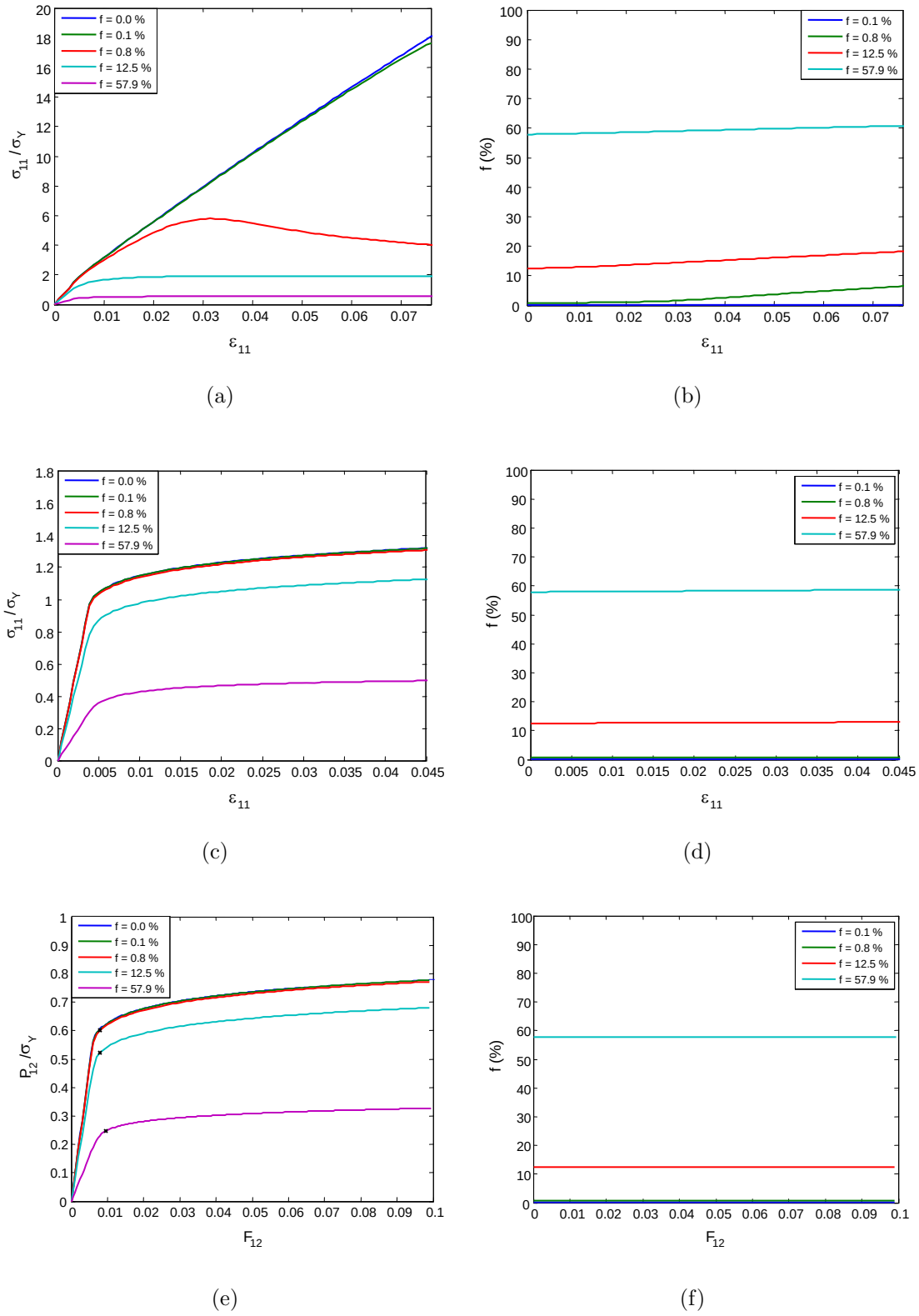


Figure 3.19: Response for different void volume fractions and different loading conditions. (a) Uniaxial strain response. (b) Evolution of the void volume fraction under uniaxial strain. (c) Uniaxial stress response. (d) Evolution of the void volume fraction under uniaxial stress. (e) Simple shear response. (f) Evolution of the void volume fraction under simple shear.

easily be computed, giving

$$\sigma_m^M = \frac{2}{3}\sigma_Y(1-f) \tag{3.138}$$

Such value has been represented with a red diamond in the figure, verifying the numerical results.

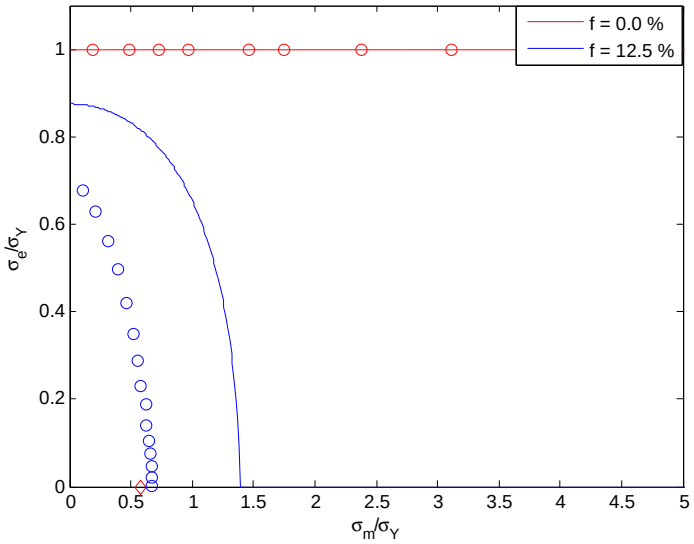


Figure 3.20: Initial yield of the representative volume element with zero and finite void volume fraction, compared to Gurson's yield surface. Parameters $a = 1, b = 2, N_r = 10, N_l = 1$. The red diamond on the x-axis indicates the analytical solution for initial yield of a rigid perfectly plastic hollow sphere.

However, Gurson assumed in his analytical derivations that the hollow sphere had fully yielded. This definition of macroscopic yield is used in the following although initial yield occurs much earlier as is seen from the previous figure. Due to the numerical instabilities arising from perfect plasticity, material properties of a typical aluminum, shown in Table 3.2, are used. In Fig. 3.21, Gurson's yield surface (continuous line) is compared with the macroscopic stresses in the event of full yielding of the hollow sphere. Due to the strain hardening, the yield stress varies through the thickness. In order to account for that effect, the macroscopic equivalent stress and pressure are normalized with the minimum ('x' symbols) and the maximum ('o' symbols) microscopic yield stress of each configuration. The colors indicate the void volume fraction in a stress-free configuration. When full yielding is attained, the void has grown with respect to its initial size. The final void

volume fraction is dependent on the axisymmetry of the deformation, and the values range for most of the performed numerical examples (for initial $f = 12.5\%$) from 13% to 17%. The two points that clearly stand out of the theoretical prediction correspond to conditions close to uniaxial strain and have a final void volume fraction of 30%. Gurson's estimate has been plotted as a dotted line for this value, showing in this case, as well, reasonable agreement with the numerical calulations.

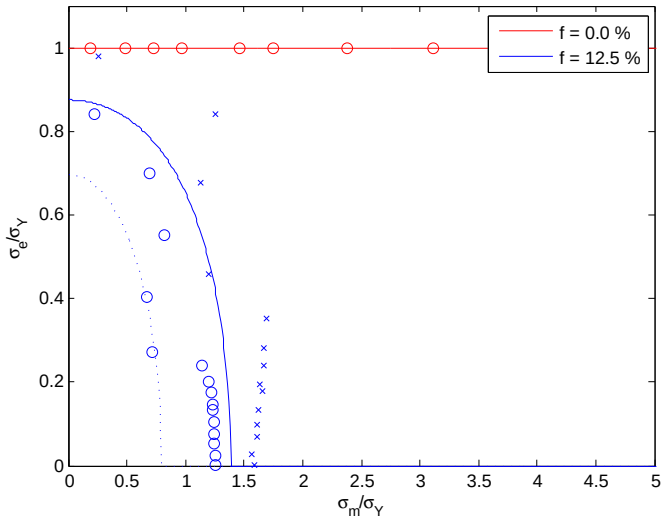


Figure 3.21: Gurson's model (continuous lines) versus numerical predictions (discrete symbols) of complete yield of the hollow sphere. Stress measures normalized with respect to the minimum ('x' symbols) and the maximum ('o' symbols) microscopic yield stress attained in the domain.

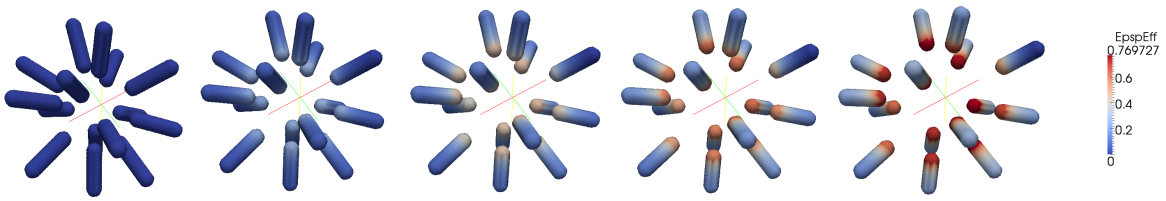


(a) (b) (c) (d) (e)

Figure 3.22: Evolution of a hollow sphere of 12.5% void volume fraction under uniaxial strain.

## 3.7.2 Dynamic

### 3.7.2.1 Explicit dynamics

As was seen in Section 3.6.6, when the material point corresponding to a hollow sphere is subjected to a volumetric deformation under a constant true strain rate, the time average of the macroscopic stresses correspond to the static definition of macro-stress. In order to view the effects of microdynamics on void growth, the hollow sphere is here deformed under constant $\ddot{\varepsilon} = 10^{12} s^{-2}$. The imposed deformation gradient on the boundary is then $F_{11} = F_{22} = F_{33} = \exp\left(\frac{1}{2} t^2 \ddot{\varepsilon}\right)$.

The material of choice is of neo-Hookean type with properties indicated in Table 3.3. The hollow sphere is expanded until $\varepsilon = 0.1$, a value that is reached in 0.3 $\mu s$. If such deformation were to be obtained at a constant strain rate, that would imply a speed of 6.7m/s, which is far below the speed of sound of the material (249 m/s).

In Fig. 3.23, the dynamic evolution is shown for varying density. For this case of an accelerating boundary, the dynamic stresses oscillate around a value that is higher than the static value. This effect is accentuated when the density is increased.

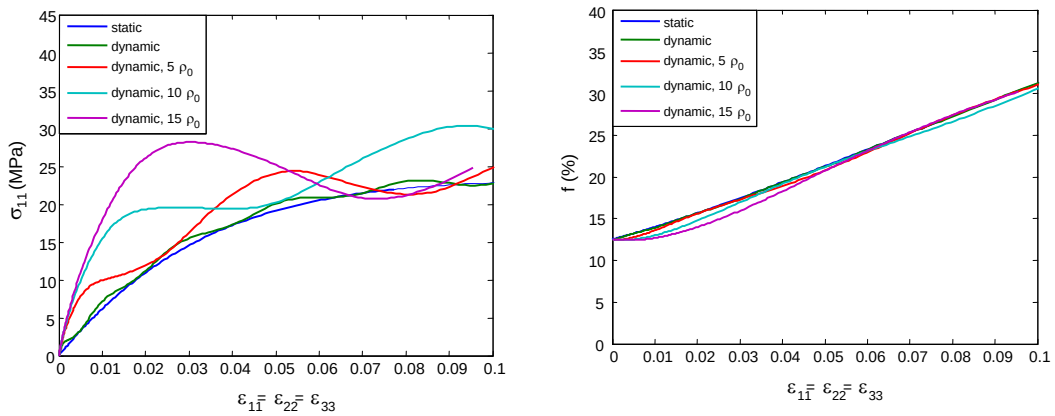


(a) (b)

Figure 3.23: Material response under spherical expansion at constant $\ddot{\varepsilon}$ with varying density. Comparison to static solution.

Not much difference can be observed in the evolution of the void volume fraction, since the deformation is the controlling parameter. Big differences are reported in the literature (Carrol and Holt, 1972, Molinari and Mercier, 2001), and are expected to be obtained, under stress controlled conditions, for which the static and dynamic deformations differ.

Table 3.2: Material properties of a typical alluminum alloy.

| $E$ (GPa) | $\nu$ | $\sigma_Y$ (MPa) | n |
|---|---|---|---|
| 68.9 | 0.33 | 276 | 0.075 |

Table 3.3: Material properties of the porous neo-Hookean material.

| $E$ (MPa) | $\nu$ | $a(\mu\text{m})$ | $a(\mu\text{m})$ | $\rho_0$ (kg/m$^3$) |
|---|---|---|---|---|
| 69 | 0.48 | 10 | 20 | 1104.72 |

## 3.8 Numerical example

In this section a full numerical simulation of the two-level porous material described throughout the chapter is implemented. In particular, the impact of a polyurea bar is chosen as a test case. Polyurea is an elastomer that is derived from the chemical reaction of an isocyanate and a synthetic resin blend, and it has shown to have great properties as a shock mitigation material. In particular, it is characterized by a high strain rate sensitivity, large maximum deformations and good adhesion properties to many materials. These characteristics make them suitable as protective coatings on structures and has motivated their experimental characterization (Chakkarapani et al., 2006, Roland and Casalini, 2007, Roland et al., 2007, Knauss and Zhao, 2007, Sarva et al., 2007).

In the first part of this section, the experiments simulated in the present study are described. This is followed by a careful material model of the polyurea used in the experiments (polyurea 1000). It is of note that depending on the actual composition, the properties of a polyurea sample can vary significantly, motivating the development of a material model, rather than making use of existent ones in the literature (Amirkhizi et al., 2006, ElSayed et al., 2009, Li and Lua, 2009). The resulting model is then validated against the experiments, showing a very good prediction, and is used as test case for the multiscale porous model.

### 3.8.1 Experiments

The experiments used in this section were performed by Mock et al. at the Naval Surface Warfare Center. They consist of the impact of a polyurea bar of initial length $L_0 = 25.7353$ mm and initial radius $R_0 = 6.29603$ mm by an anvil of high stiffness at speeds of $v = 245$ m/s and $v = 332$ m/s. The bar deforms significantly and then bounces back. Fig. 3.24 shows a sequence of captions of the deformation during the impact for the lower velocity. The recovered bars, for the two cases, with different void damage on the lower part, can be observed in Fig. 3.25.

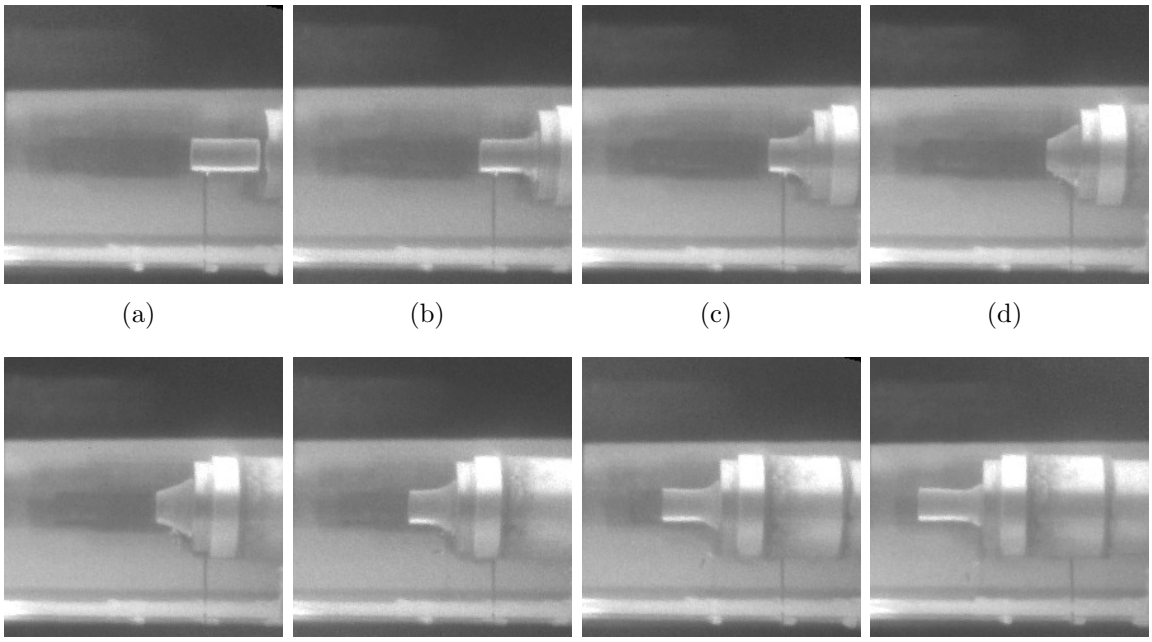

(a) (b) (c) (d)

(e) (f) (g) (h)

Figure 3.24: Taylor anvil test of polyurea rod. Experiments performed by Mock et al. at NSWC. $R_0 = 6.29603$ mm, $L_0 = 25.7353$ mm and $v = 245$ m/s.

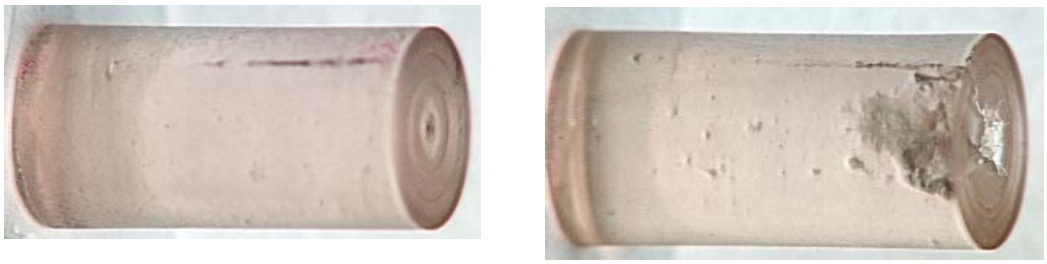

(a) (b)

Figure 3.25: Post impact images of the polyurea rod. Experiments performed by Mock et al. at NSWC. (a) $v = 245$ m/s. (b) $v = 332$ m/s.

### 3.8.2 Material modeling without porosity

The model employed for the polyurea 1000 is based on its uniaxial characterization under compression at a wide range of strain rates made by Sarva et al. (2007). The model is then generalized to multiaxial conditions by fixing a value for the Poisson's ratio. Due to its almost incompressible behavior, a value close to 0.5 is chosen.

The experiments show that polyurea stress-strain relation is strongly dependent on the strain rate, has a rubbery behavior at low strain rates and does not undergo significant plastic deformation. Based on these observations, the chosen constitutive model is composed of a hyperelastic part and several viscoelastic mechanisms. The strain energy density can then be decomposed as follows

$$W(\mathbf{C}) = W^e(\mathbf{C}) + W^v(\mathbf{C}, \boldsymbol{\varepsilon}^p) \tag{3.139}$$

where $\mathbf{C}$ is the left Cauchy-Green deformation tensor and $\varepsilon^p$ is an ensemble of internal variables characterizing the different viscoelastic mechanisms. Each of the terms of the energy density is examined independently in the following subsections.

In order to obtain the material parameters, full incompressibility of the material is first considered. This initial assumption allows the derivation of tractable analytic expressions of the uniaxial material response, providing a ground for comparison with the the experimental results. The incompressibility condition is then relaxed in order to account for small volumetric changes.

#### 3.8.2.1 Hyperelastic model at low strain rates

The stress-strain relationship from Sarva et al. (2007) at a true strain rate of $\dot{\varepsilon} = 0.0016\ s^{-1}$ is used to determine the most appropriate hyperelastic model. Due to the low value of the strain rate, the viscoelastic stresses are neglected and the response of the material is assumed to be fully elastic.

Table 3.4: Fitting parameters of the Ogden model.

| | 1 | 2 |
|---|---|---|
| $\mu_i$ (MPa) | 13.9277 | 12.9279 |
| $\alpha_i$ | 6.0351 | -3.0608 |

Several hyperelastic models are examined under the assumption of incompressibility

$$\begin{aligned}
&\text{Neo-Hookean: } W^e = \frac{\mu}{2}\left(\lambda_1^2+\lambda_2^2+\lambda_3^2-3\right)\\
&\text{Mooney-Rivlin: } W^e = \frac{\mu_1}{2}\left(\lambda_1^2+\lambda_2^2+\lambda_3^2-3\right)+\frac{\mu_2}{2}\left(\lambda_1^{-2}+\lambda_2^{-2}+\lambda_3^{-2}-3\right)\\
&\text{Ogden: } W^e = \sum_{i=1}^{M}\frac{\mu_i}{\alpha_i}\left(\lambda_1^{\alpha_i}+\lambda_2^{\alpha_i}+\lambda_3^{\alpha_i}-3\right)
\end{aligned} \tag{3.140}$$

where $W^e$ is the strain energy density, $\lambda_i$ are the principal stretches and $\mu$ and $\mu_i$ are material parameters.

The stress-strain relationships for a uniaxial compression experiment ($\lambda_1 = \lambda, \lambda_2 = \lambda_3 = \lambda^{-1/2}$) are

$$\begin{aligned}
&\text{Neo-Hookean: } P^e = \frac{\mu}{\lambda}\left(\lambda^2-\lambda^{-1}\right)\\
&\text{Mooney-Rivlin: } P^e = \mu_1\left(\lambda-\frac{1}{\lambda^2}\right)+\mu_2\left(1-\frac{1}{\lambda^3}\right)\\
&\text{Ogden: } P^e = \sum_{i=1}^{M}\frac{\mu_i}{\lambda}\left(\lambda^{\alpha_i}-\lambda^{-\alpha_i/2}\right)
\end{aligned} \tag{3.141}$$

where $P^e = P_1^e$ is the component of the first Piola-Kirchhoff stress tensor in the loading direction.

The optimal fit obtained for each of the models is shown in Fig. 3.26. In view of the results, a two-term Ogden constitutive law is chosen to represent the elastic behavior of the polyurea. The parameters resulting from the fit are listed in Table 3.4.

The corresponding elastic modulus at small strains is $E = \frac{3}{2}\left(\mu_1\alpha_1+\mu_2\alpha_2\right) = 66.73$ MPa, very close to the value of 69 MPa found by Knauss and Zhao (2007) in their experimental tests at small strains.

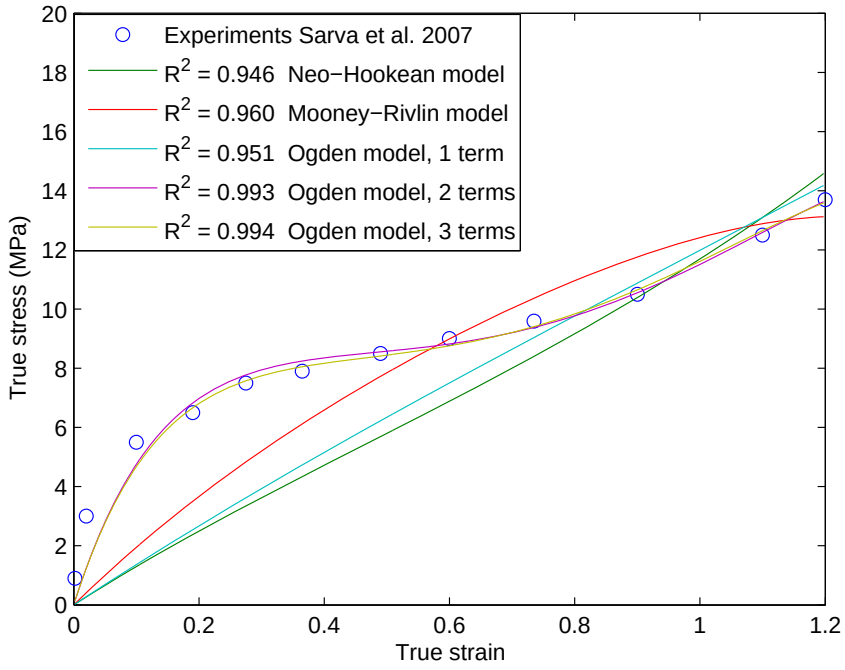


Figure 3.26: Fit of the quasi-static behavior of the polyurea ($\dot{\varepsilon} = 0.0016\ s^{-1}$) with different hyperelastic material models.

#### 3.8.2.2 Viscoelastic model for polyurea

The several viscoelastic mechanisms present in the polyurea are represented by means of a Prony series. The viscoelastic strain energy density can be written in the linearized kinematic version as

$$\tilde{W}^v(\boldsymbol{\varepsilon}, \boldsymbol{\varepsilon}^{p,\alpha}) = \sum_{\alpha=1}^{N} \mu_\alpha (\boldsymbol{\varepsilon}^{\text{dev}} - \boldsymbol{\varepsilon}^{p,\alpha}) : (\boldsymbol{\varepsilon}^{\text{dev}} - \boldsymbol{\varepsilon}^{p,\alpha}) \tag{3.142}$$

where the internal variables $\varepsilon^{p,\alpha}$ obey the following evolution law

$$\dot{\boldsymbol{\varepsilon}}^{p,\alpha} = \frac{\boldsymbol{\varepsilon}^{\text{dev}} - \boldsymbol{\varepsilon}^{p,\alpha}}{\tau^\alpha} \tag{3.143}$$

with $\tau^\alpha = \frac{\eta_\alpha}{2\mu_\alpha}$ being the relaxation times associated to each viscoelastic mechanism.

This model can be extended to large strains through the logarithmic strain relation

$\varepsilon = \frac{1}{2}\log \mathbf{C}$, leading to

$$W^v(\mathbf{C}, \boldsymbol{\varepsilon}^{p,\alpha}) = \tilde{W}^v(\frac{1}{2}\log \mathbf{C}, \boldsymbol{\varepsilon}^{p,\alpha}) = \sum_{\alpha=1}^{N} \mu_\alpha \left(\frac{1}{2}\log \mathbf{C} - \boldsymbol{\varepsilon}^{p,\alpha}\right) : \left(\frac{1}{2}\log \mathbf{C} - \boldsymbol{\varepsilon}^{p,\alpha}\right) \quad (3.144)$$

Note that in the incompressible limit

$$(\log \mathbf{C})^{\text{dev}} = \log \mathbf{C} - \frac{\text{Tr}(\log \mathbf{C})}{3} I = \log \mathbf{C} - \frac{\log(\det \mathbf{C})}{3} I = \log \mathbf{C} \quad (3.145)$$

The experiments done by Sarva et al. (2007), shown in Fig. 3.27, are performed at almost constant true strain rate (see Fig. 3.29). The material model is therefore particularized to the case of uniaxial compression at constant true strain rate ($\varepsilon(t) = \dot{\varepsilon} t$) for comparison. Under the assumption of incompressibility ($\lambda_1 = \lambda, \lambda_2 = \lambda_3 = \lambda^{-1/2}$)

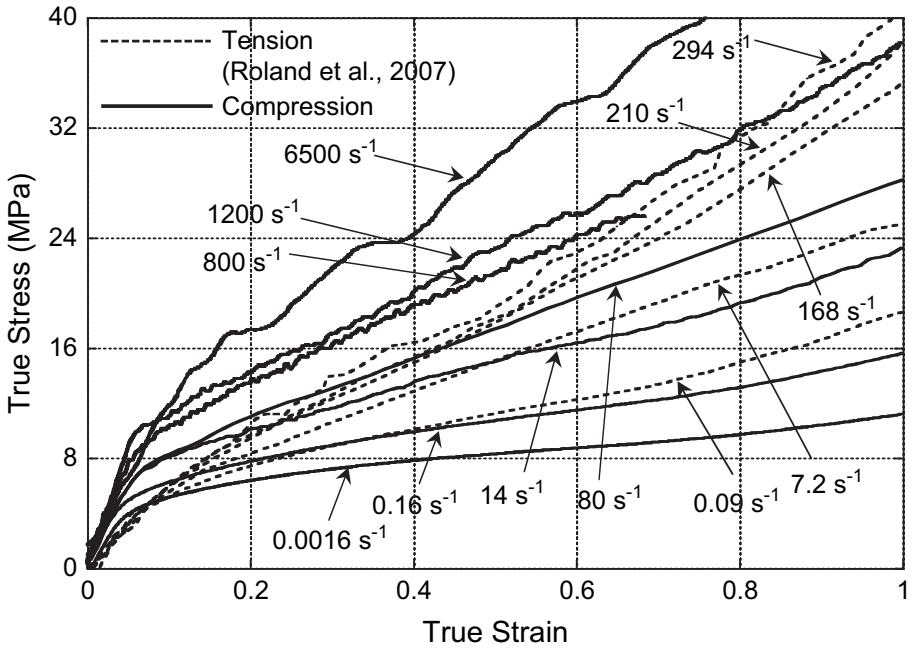


Figure 3.27: Uniaxial compression stress-strain behavior of polyurea at several true strain rates (Sarva et al., 2007).

$$W^v(\lambda) = \sum_{\alpha=1}^{N} \mu_\alpha \left[(\log \lambda - \varepsilon_{11}^{p,\alpha})^2 + 2\left(-\frac{1}{2}\log \lambda - \varepsilon_{22}^{p,\alpha}\right)^2\right] \quad (3.146)$$

and the stress in the loading direction is

$$P^v = \frac{dW^v(\lambda)}{d\lambda} = \sum_{\alpha=1}^{N} \frac{\mu_\alpha}{\lambda} \left[3\log\lambda + 2\left(\varepsilon_{22}^{p,\alpha} - \varepsilon_{11}^{p,\alpha}\right)\right] \tag{3.147}$$

where $\lambda = e^{\dot{\varepsilon}t}$.

The evolution law for the internal variables becomes, for this case of uniaxial compression,

$$\begin{aligned} \tau^\alpha \dot{\varepsilon}_{11}^{p,\alpha} &= \log\lambda - \varepsilon_{11}^{p,\alpha} \\ \tau^\alpha \dot{\varepsilon}_{22}^{p,\alpha} &= -\frac{1}{2}\log\lambda - \varepsilon_{22}^{p,\alpha} \end{aligned} \tag{3.148}$$

Defining $\varepsilon^{p,\alpha} = \varepsilon_{11}^{p,\alpha} - \varepsilon_{22}^{p,\alpha}$, these two equations can be combined, reducing the number of internal variables and kinetic relations to a single one

$$\tau^\alpha \dot{\varepsilon}^{p,\alpha} = \frac{3}{2}\log\lambda - \varepsilon^{p,\alpha} = \frac{3}{2}\dot{\varepsilon}t - \varepsilon^{p,\alpha} \tag{3.149}$$

The solution to this first order ordinary differential equation with initial conditions $\varepsilon^{p,\alpha}(t=0) = 0$ is

$$\varepsilon^{p,\alpha} = \frac{3}{2}\dot{\varepsilon}t - \frac{3}{2}\dot{\varepsilon}\tau^\alpha\left(1 - e^{-t/\tau^\alpha}\right) \tag{3.150}$$

The stretch-stress relation for the complete model then becomes

$$P = \sum_{i=1}^{M} \frac{\mu_i}{\lambda}\left(\lambda^{\alpha_i} - \lambda^{-\alpha_i/2}\right) + \sum_{\alpha=1}^{N} \frac{3\mu_\alpha}{\lambda}\dot{\varepsilon}\left(1 - e^{-t/\tau^\alpha}\right) \tag{3.151}$$

with $t = \varepsilon/\dot{\varepsilon}$. The true or Cauchy stress can easily be computed as $\sigma = \lambda P$.

This relation leads to a different curve for each true strain rate. However, they can all be reduced to a single master curve if the lower strain rate response is assumed to be fully elastic. This master curve is obtained by representing $\frac{\sigma_c}{\dot{\varepsilon}} = \frac{\sigma - \sigma_0}{\dot{\varepsilon}}$ versus $\beta = \frac{\varepsilon}{\dot{\varepsilon}}$, where $\sigma_0 = \sigma(\dot{\varepsilon} = 0.0016s^{-1})$. The result is analog to a relaxation curve with the input being a ramp function instead of a step function.

$$\frac{\sigma_c}{\dot{\varepsilon}} = \sum_{\alpha=1}^{N} 3\mu_\alpha\tau^\alpha\left(1 - e^{-\frac{\beta}{\tau^\alpha}}\right) \tag{3.152}$$

This transformation has been performed to the experimental curves in Fig. 3.28. As can be seen in this figure, the experimental points all fall into the same curve, which in logarithmic scale results in an almost straight line. This confirms the applicability of the proposed model to describe the polyurea behavior in such range of deformations. Only the initial points of each curve (corresponding to the lower strains) do not fall into the master curve. This can be explained by the fact that the true strain rate is not exactly constant. Fig. 3.29 from Sarva et al. (2007) shows that the true strain rate is initially lower, leading, according to the proposed normalization, to a higher value of the normalized true stress.

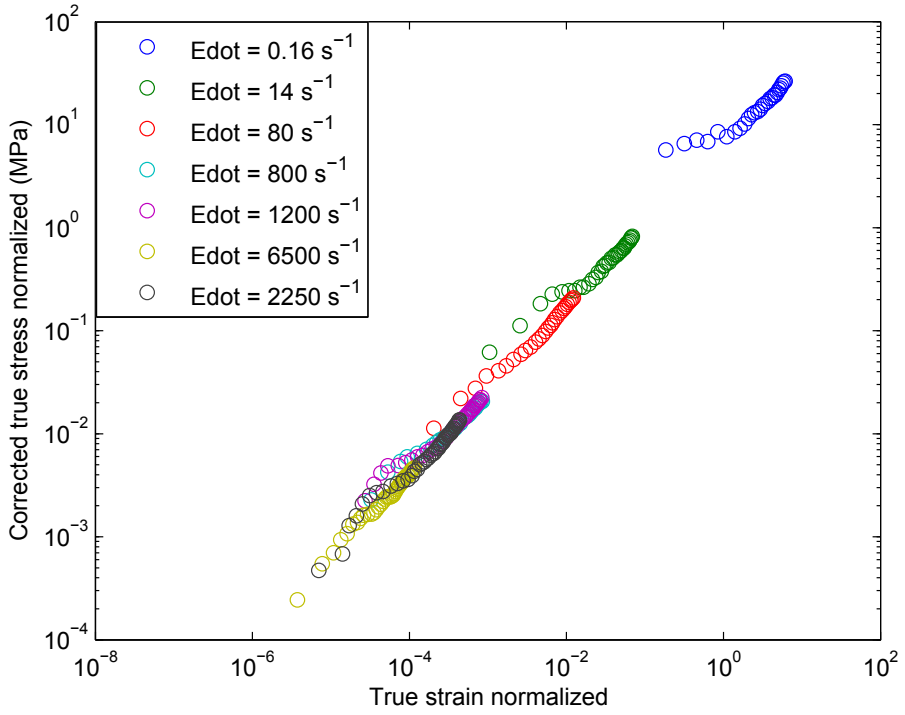


Figure 3.28: Master curve resulting from normalizing the experimental stress-strain relation of Sarva et al. (2007).

This master curve only depends on the viscoelastic parameters, and can therefore be used to obtain the desired values of the parameters. This fit has been performed by fixing the values of the relaxation times as previously done by other authors (Knauss and Zhao, 2007). The parameters obtained by this procedure are then optimized with use of the actual experimental stress-strain curves. The resulting model and its comparison to the experimental data are shown in Figs. 3.30 and 3.31.

The parameters involved in the Prony series are summarized in Table 3.5. Lower

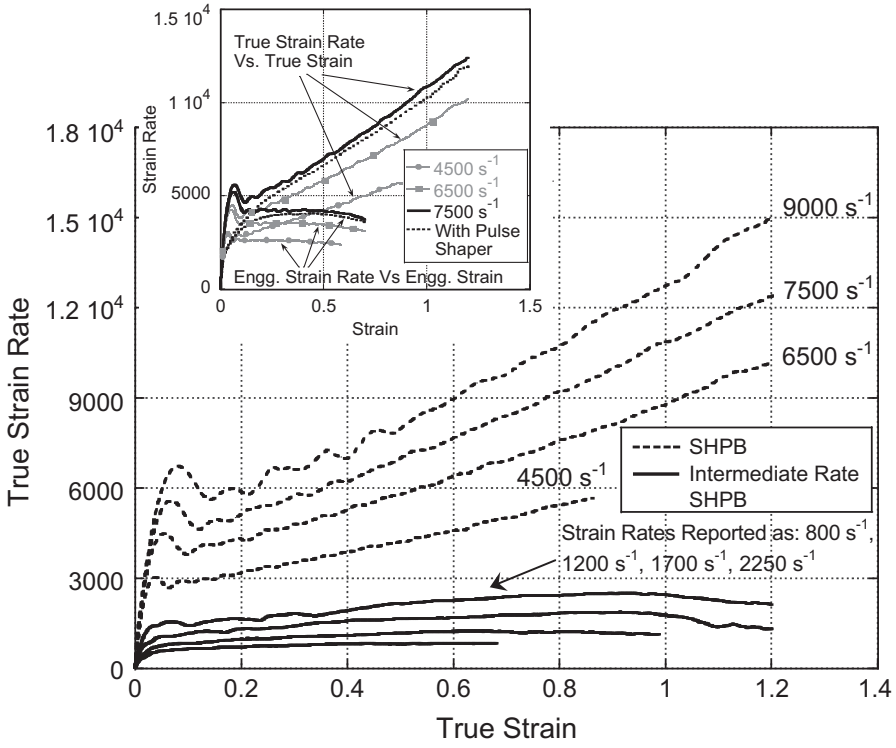


Figure 3.29: Evolution of the true strain rate in the uniaxial compression experiments performed by Sarva et al. (2007).

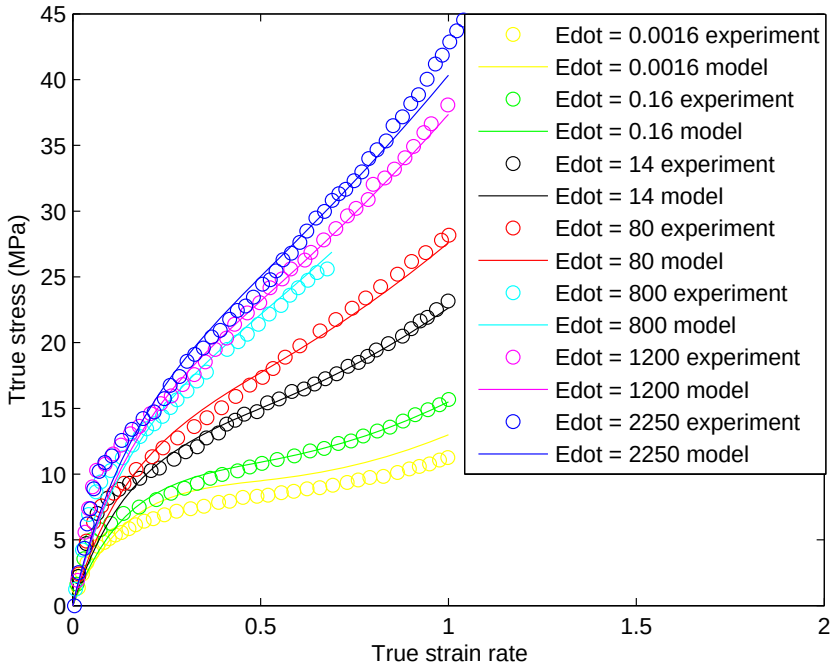


Figure 3.30: Comparison of the developed material model and the experimental results of Sarva et al. (2007) at different strain rates.

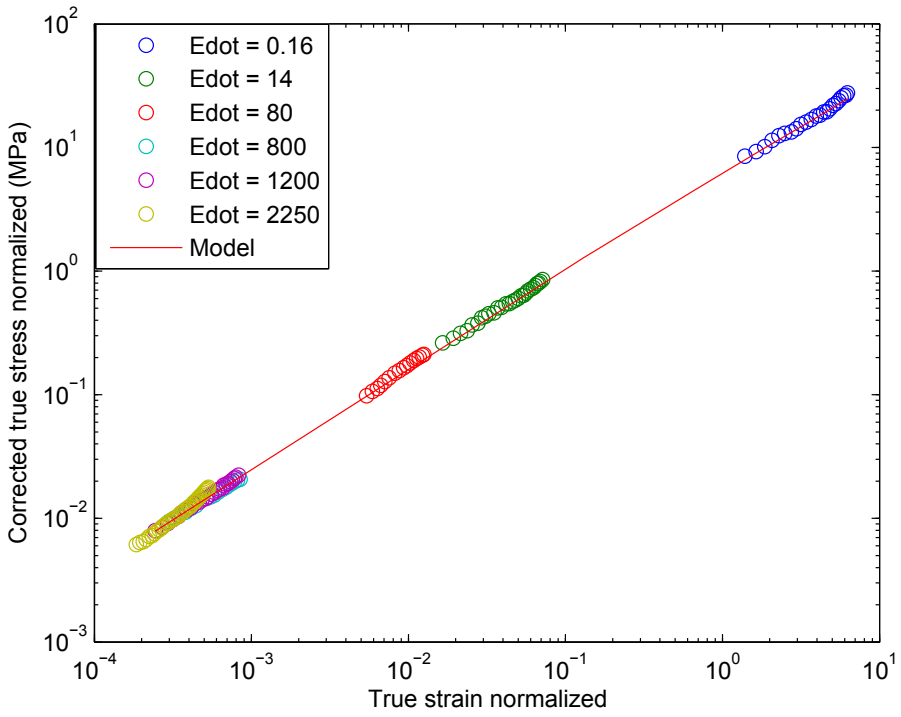


Figure 3.31: Comparison of the master curve obtained with the developed material model and the experimental results of Sarva et al. (2007) at different strain rates.

Table 3.5: Parameters involved in the viscoelastic representation of polyurea 1000.

| $3\mu_i$ (MPa) | $\alpha_i$ |
|---|---|
| 15.4933 | 1.0e-5 |
| 16.2 | 1.0e-4 |
| 7.5863 | 1.0e-3 |
| 7.5747 | 1.0e-2 |
| 4.3520 | 1.0e-1 |
| 3.3033 | 1.0 |
| 0.8980 | 10.0 |
| 0.9958 | 100.0 |
| 1.7333 | 1000.0 |

values of relaxation times did not seem to have a significant influence on the response of the material at the strain rates examined, and are taken to be equal to the values reported by Knauss and Zhao (2007). We recall that Knauss and Zhao provide the values of the Young's modulus for each relaxation time. These values are related to the shear modulus in the incompressible limit through the usual relation

$$\mu_\alpha = \frac{E_\alpha}{3} \tag{3.153}$$

as is proven in Appendix D.

Later on, the material is considered to be slightly compressible. In that case, it is proven by contradiction in Appendix E that the material cannot have a constant Poisson's ratio. The relation between the shear modulus and the Young's modulus is obtained in Appendix F, and simplifies in the case of a quasi-incompressible material to the usual relation for elastic isotropic homogeneous materials.

$$\mu_\alpha = \frac{E_\alpha}{2(1+\nu)} \tag{3.154}$$

In the following, the assumption of uniaxial compression under constant true strain rate is verified. In particular, the material response under the conditions labeled as $\dot{\varepsilon} = 6500 s^{-1}$ and $\dot{\varepsilon} = 9000 s^{-1}$ by Sarva et al. (2007) are examined (see Fig. 3.29).

From the provided true strain rate versus the true strain, one can numerically obtain the true strain evolution with respect to time. The following discretization has been employed.

$$\begin{aligned} \Delta t_{n+1} &= \frac{\varepsilon_{n+1} - \varepsilon_n}{\dot{\varepsilon}_{n+1}} \\ t_{n+1} &= t_n + \Delta t_{n+1} \end{aligned} \tag{3.155}$$

The resulting temporal evolution can be approximated by a second order polynomial in time. The results are shown in Fig. 3.32.

An analytical solution for this type of load history can also be easily obtained. In

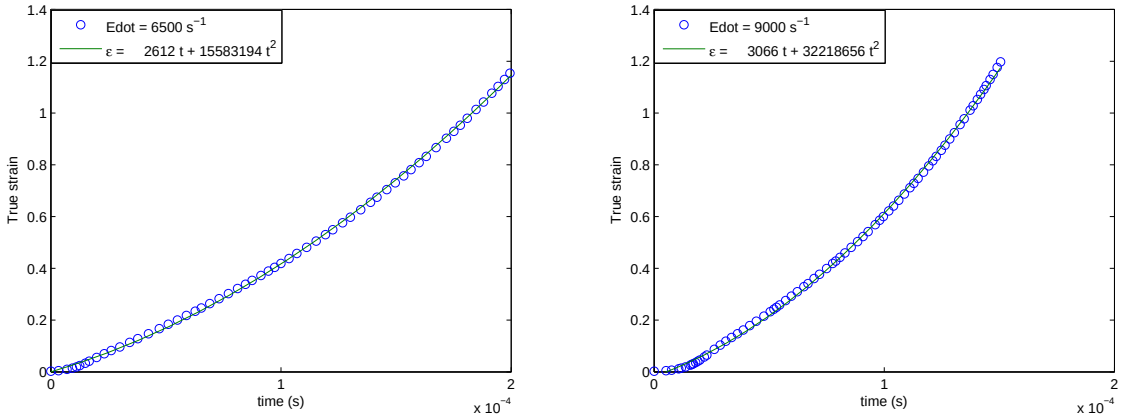


(a) (b)

Figure 3.32: Strain history obtained from the experimental true strain rate versus true strain history and fit to the curve with a quadratic polynomial. (a) $\dot{\varepsilon} = 6500s^{-1}$. (b) $\dot{\varepsilon} = 9000s^{-1}$.

particular, the evolution of the internal variables is given by

$$\tau^{\alpha}\dot{\varepsilon}^{p,\alpha} = \frac{3}{2}\varepsilon - \varepsilon^{p,\alpha} \tag{3.156}$$

with $\varepsilon(t)$ of the form $\varepsilon(t) = At + Bt^2$. The internal variables then follow the evolution law

$$\varepsilon^{p,\alpha} = -\frac{3}{2}\tau^{\alpha}(A - 2B\tau^{\alpha})\left(1 - e^{-t/\tau^{\alpha}}\right) + \frac{3}{2}(A - 2B\tau^{\alpha})t + \frac{3}{2}Bt^2 \tag{3.157}$$

and the stress in the loading direction becomes

$$\sigma = \sum_{i=1}^{2}\mu_i\left(\lambda^{\alpha_i} - \lambda^{-\alpha_i/2}\right) + \sum_{\alpha=1}^{N}3\mu_{\alpha}\tau^{\alpha}\left[(A - 2B\tau^{\alpha})\left(1 - e^{-t/\tau^{\alpha}}\right) + 2Bt\right] \tag{3.158}$$

The previously shown stress-strain curves in Fig. 3.30 and the predicted ones at higher strain rates are shown in Fig. 3.33 demonstrating a reasonably accurate prediction.

The assumption of exact constant strain rate in the model can now be verified to be a good approximation, despite a slight initial deviation of the strains. In Fig. 3.34 the model prediction under the assumption of a constant strain rate and the experimental strain history are shown, and almost identical results are obtained.

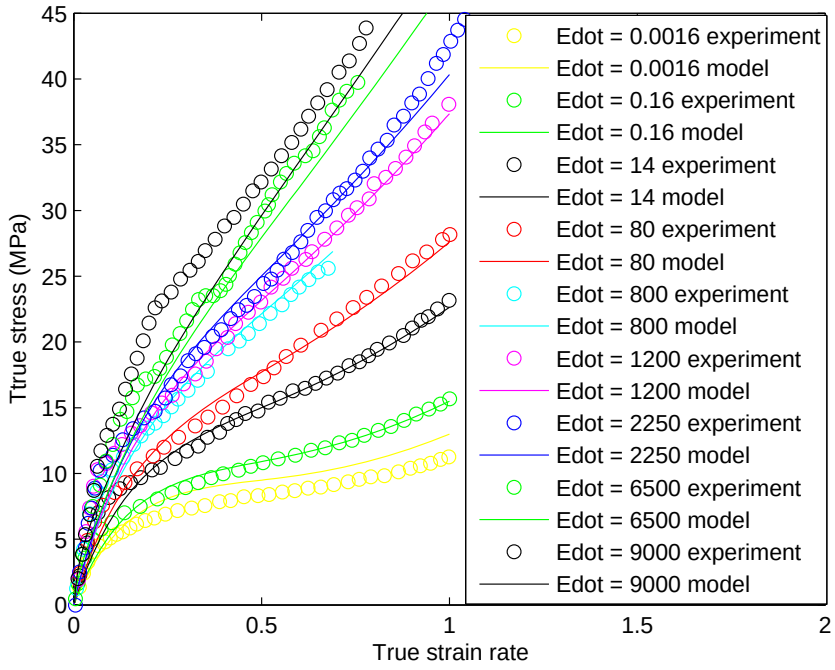


Figure 3.33: Comparison of the stress-strain response of the material model and the experiments performed by Sarva et al. (2007) at several strain rates.

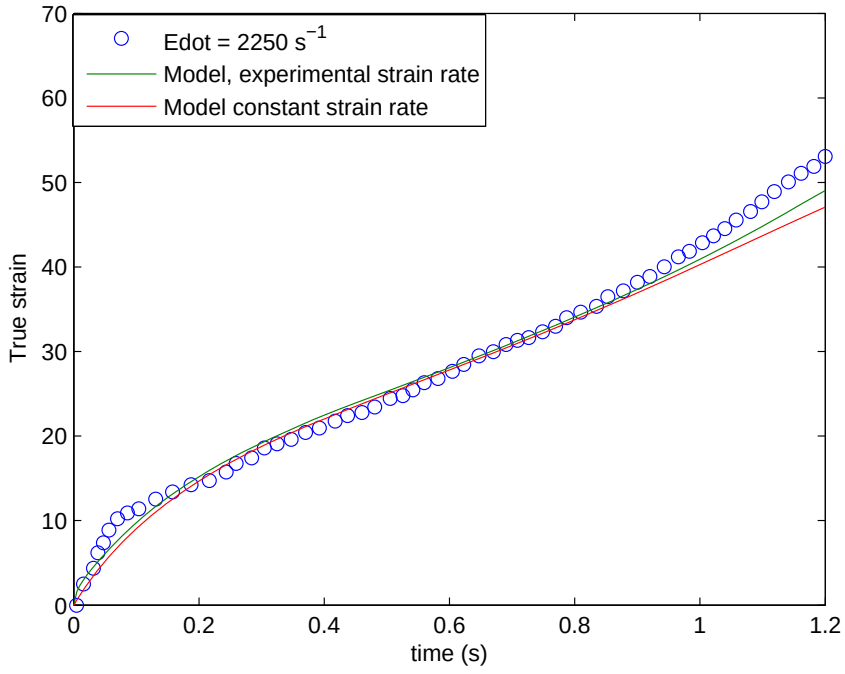


Figure 3.34: Verification of the constant strain rate assumption.

#### 3.8.2.3 Complete model for polyurea

The complete model previously derived under the assumption of incompressibility is

$$W = \sum_{i=1}^{M} \frac{\mu_i}{\alpha_i} \left(\lambda_1^{\alpha_i} + \lambda_2^{\alpha_i} + \lambda_3^{\alpha_i} - 3\right) + \sum_{\alpha=1}^{N} \mu_\alpha \left(\frac{1}{2}\log \mathbf{C} - \boldsymbol{\varepsilon}^{p,\alpha}\right) : \left(\frac{1}{2}\log \mathbf{C} - \boldsymbol{\varepsilon}^{p,\alpha}\right) \quad (3.159)$$

with the parameters summarized in Tables 3.4 and 3.5.

This model is extended to the compressible range with a Blatz-Ko equation of state, which is widely used for compressible rubbery materials (Blatz and Ko, 1962). The strain energy density results in

$$\begin{aligned} W =& \frac{1-2\nu}{2\nu}\mu\left(J^{-\frac{2\nu}{1-2\nu}} - 1\right) + \frac{3}{2}\mu(J^{2/3} - 1) \\ &+ \sum_{i=1}^{M} \frac{\mu_i}{\alpha_i}\left(\bar{\lambda}_1^{\alpha_i} + \bar{\lambda}_2^{\alpha_i} + \bar{\lambda}_3^{\alpha_i} - 3\right) \\ &+ \sum_{\alpha=1}^{N} \mu_\alpha \left(\frac{1}{2}(\log \mathbf{C})^{\mathrm{dev}} - \boldsymbol{\varepsilon}^{p,\alpha}\right) : \left(\frac{1}{2}(\log \mathbf{C})^{\mathrm{dev}} - \boldsymbol{\varepsilon}^{p,\alpha}\right) \end{aligned} \quad (3.160)$$

where $\nu$ is the Poisson's ratio and $\mu = \frac{1}{2}\left(\mu_1\alpha_1 + \mu_2\alpha_2\right)$.

### 3.8.3 Material modeling with porosity

The hollow sphere model can now be combined with the polyurea model so as to demonstrate the effect of void growth. First, a comparison in Fig. 3.35 between the non-porous and porous material response at high strain rate is shown. Two different meshes at the microscopic level have been used to assess the accuracy of the results. The macroscopic stresses represented correspond to the static definition so as to consider a single microscopic parameter: the void volume fraction.

### 3.8.4 Comparison with experiments

In this section, the non-porous material model described in the foregoing is validated against the experiments of they Taylor test at lower velocity and is then used together with the hollow sphere element to analyze the void evolution in the experiment at higher

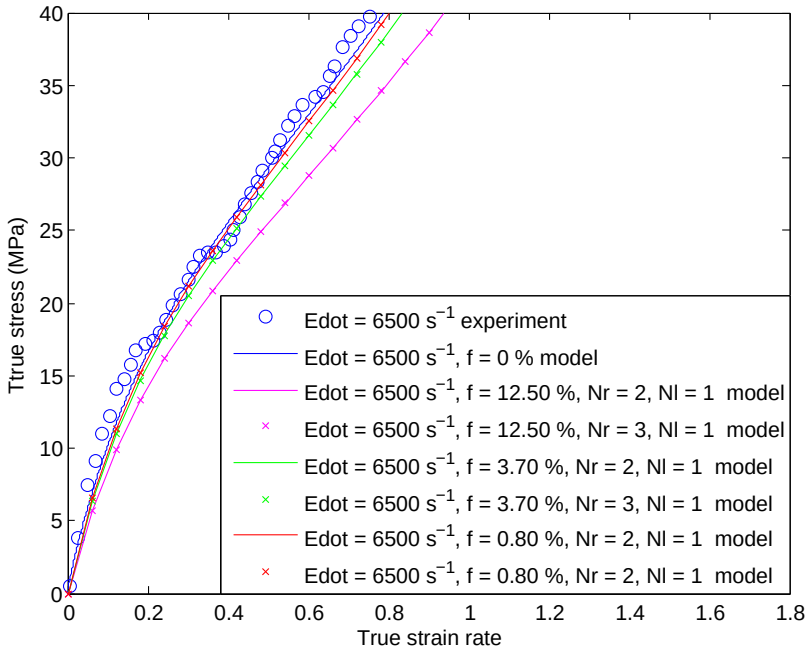


Figure 3.35: Comparison of the uniaxial material response between experiments (Sarva et al., 2007), non-porous material model, and porous material model with two void volume fractions.

velocity. A value for the Poisson's ratio of $\nu = 0.48$ is chosen in the finite element simulation.

Numerically, tetrahedral elements based on mean volumetric deformation under finite kinematics with of bubbles in the faces of the simplicial elements, are used at the macroscopic scale. They are chosen so as to overcome the locking problems that might arise due to the fact that the material is nearly incompressible. Two different mesh sizes, represented in Fig. 3.36, were used in order to guarantee convergence of the numerical result. Regarding the temporal discretization, an explicit dynamic method is used for the time evolution of the system. A constant time step proportional to the CFL condition is employed. Several proportional factors were used in order to assess the convergence in time for a given mesh.

Fig. 3.37 shows the temporal evolution of the length and maximum radius compared with the experiments, demonstrating convergence. The shape evolution is shown in Fig. 3.38, where very good agreement is observed during the compression stage. The differences attendant to the expansion phase and to the contour of the bar close to the contact surface, could be due to friction or adhesion, effects that have not been included

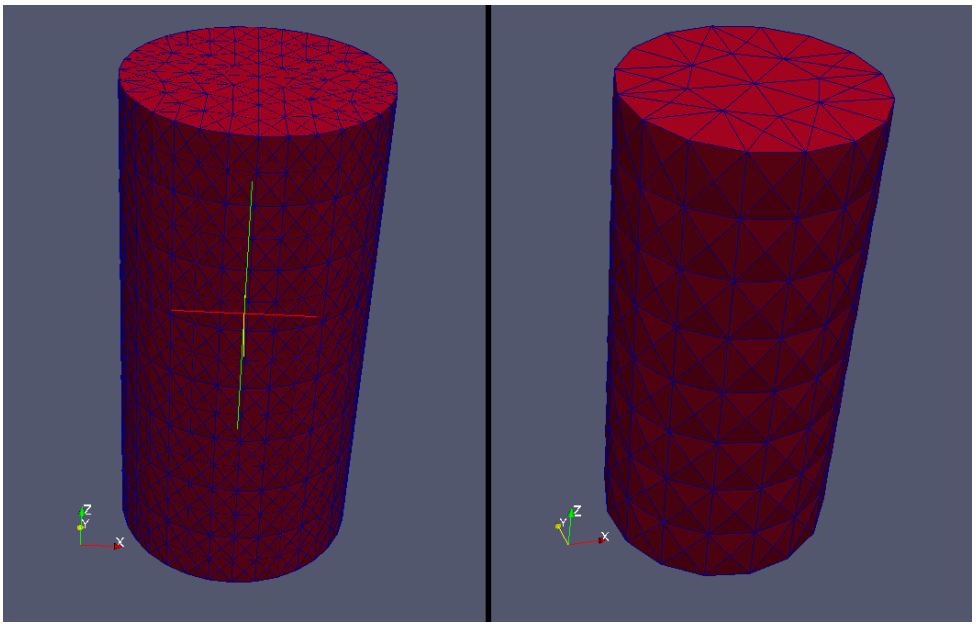

Figure 3.36: Fine mesh ( 48000 nodes and 20000 elements) and coarse mesh ( 6000 nodes and 2500 elements) used in the finite element simulation of the Taylor test.

in the simulations.

Next, the porous material is used on the lower 90% of the bar for the simulation at higher velocity. In order to have a single parameter describing the micromechanical model, the static definition of the macroscopic stresses is used. Aside from these considerations, the macroscopic model evolves with an explicit dynamic algorithm, similar to the non-porous case. A parallel implementation of the Optimal Transportation Meshfree method (OTM) (Li et al., 2010) is used to resolve the fields in space. In particular, the results shown are performed with 1500 nodes.

The determinant of the deformation gradient is represented over the central cross section of the bar at different times during the compression stage in order to perform comparisons with respect to the non porous case at lower velocity. As can be observed from Fig. 3.39, there is a marked dilatation at the bottom part of the bar. The void volume fraction of the material points also increases significantly as is observed in Fig. 3.40. This region of high increase in void volume fraction corresponds qualitatively with the damaged zone in the recovered polyurea samples. Although further simulations and analyses are required to asses the predictability of the model, the feasibility of the proposed two-scale finite element model was demonstrated.

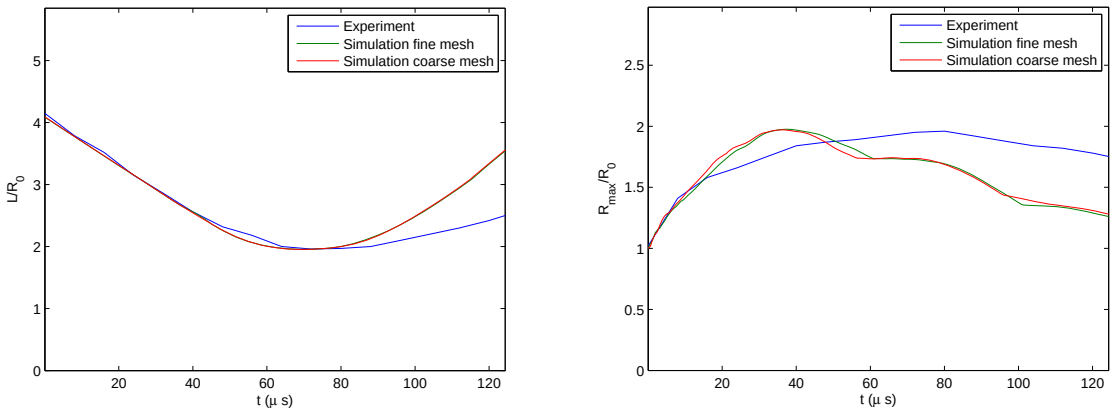


(a) (b)

Figure 3.37: Comparison between experiments (Mock *et al.*)and simulations with two different mesh sizes. (a) Evolution of the normalized length versus time. (b) Evolution of the normalized radius versus time.

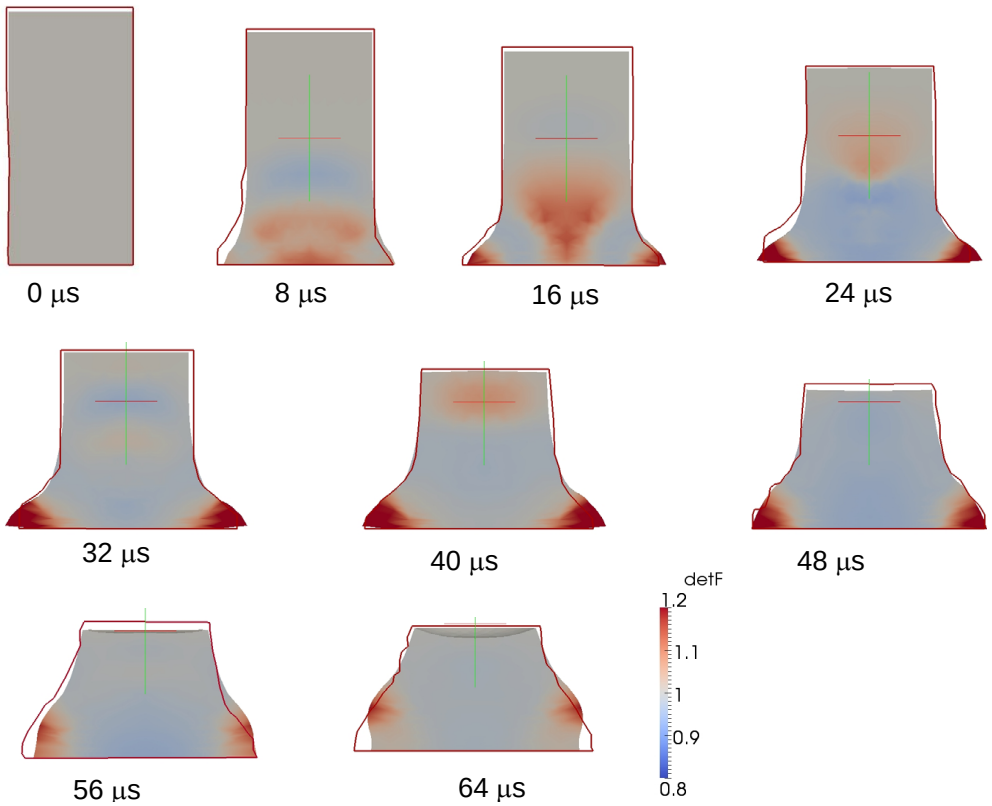


Figure 3.38: Comparison between experimental (Mock *et al.*) and numerical digitized shapes of the bar at different times for the velocity of $v = 245$ m/s. Non-porous material model.

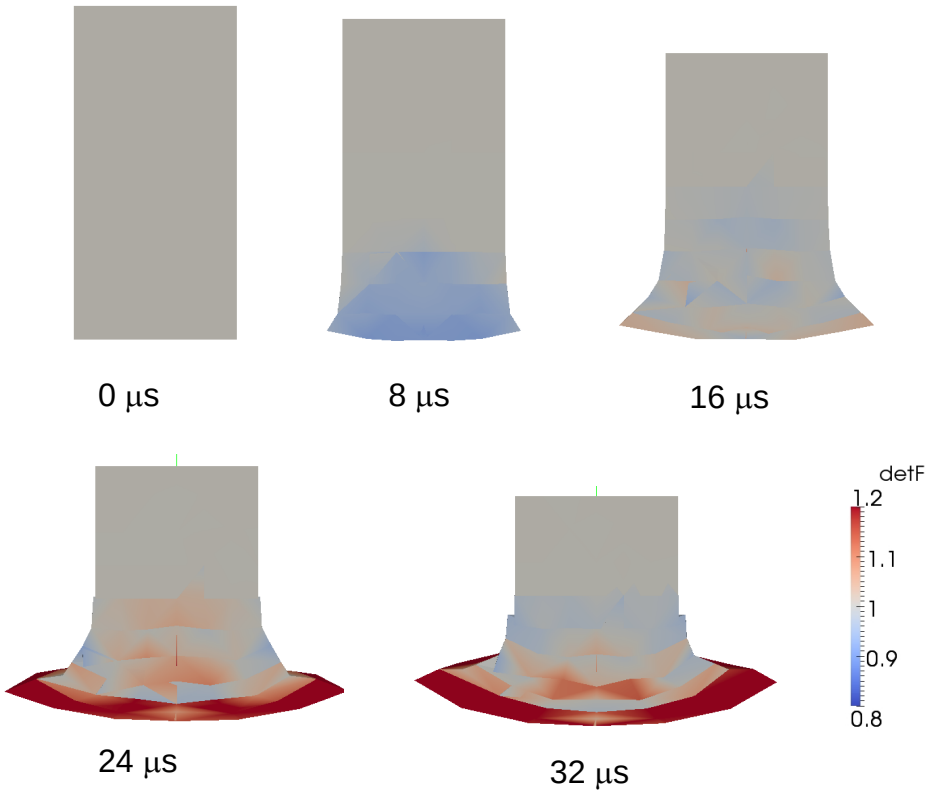


Figure 3.39: Numerical evolution of the Taylor bar experiment at $v = 332$ m/s with the porous material model at initial porosity of 1.5 %.

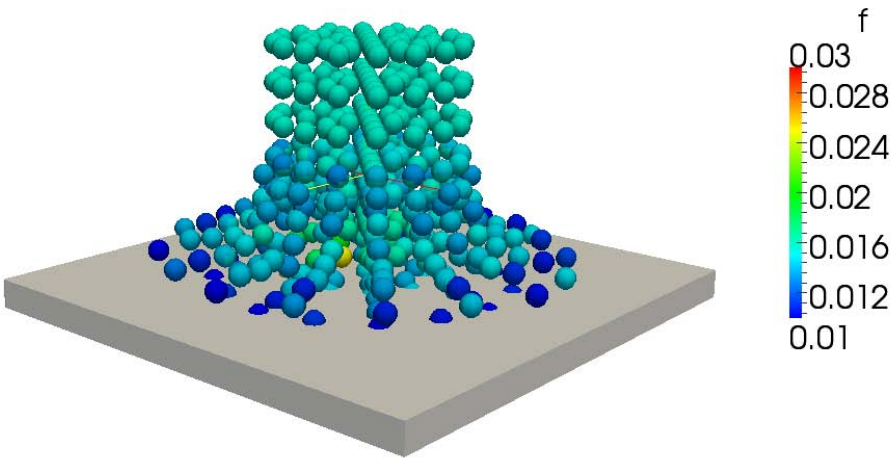


Figure 3.40: Void volume fraction distribution at 32 $\mu$s.

# Chapter 4

# Concluding remarks and further directions

This thesis was devoted to multiscale modeling and simulation of nucleation and growth of voids. In the first part, a complete multiscale model, temperature and pressure dependent, has been formulated for the nucleation of voids via vacancy aggregation. Quantum mechanical results at different volumetric deformations were employed to parametrize a lattice kinetic Monte Carlo model that describes the vacancy diffusion. Additionally, a continuum mechanics estimate was developed to assert when voids can grow by plastic deformation, establishing the transition between void growth controlled by diffusion and void growth dominated by plasticity. A very interesting conclusion drawn from the study was the size effect on plastic void growth, which was a necessary ingredient in the continuous estimate so as to match the quasi-continuum calculations. Most of the elements composing the atomistic model can be found in previous publications. A complete multiscale model that provides nucleation times from ab-initio calculations was, though, unknown to the author. These results were possible through the introduction of many simplifying assumptions, which leaves room for further improvements. Amongst those, more accurate calculations of energetics of big clusters of vacancies can be considered by means of interaction potentials. Interesting comparisons can also be performed between the proposed estimate for nucleation criteria and studies of dislocation emissions from voids (Stevens et al., 1972, Meyers and Aimone, 1983, Wolfer, 1988, Lubarda et al., 2004).

The second part of the thesis was dedicated to the development of a consistent two-level finite element description of porous materials under general loading conditions. The first

step consisted of extending the well known averaging results over representative volume elements, so as to include microdynamic effects within the finite kinematic framework. Two cases were considered in the continuous setting. The first case involved separation of length scales with time as a common variable between the two levels; and in the second one, separation of time scales is further assumed. By performing averages on the variational principles of mechanics at local equilibrium, the sought-after macro-variables and balance equations were obtained. The required space and time discretization for numerical purposes was then analyzed. Advantage was taken of the variational framework previously established, to base the discretization in the theory of variational integrators. On the other hand, the space discretization of the hollow sphere (RVE chosen to describe the porous material), was performed with an element especially developed for a spherical geometry. It consisted of spherical shell elements with an approximation space based on spherical harmonics. The resulting constitutive law, after such discretization, has the property of respecting the symmetries of the material. This property is generally not satisfied by standard finite element formulations. A quadrature rule was also developed, which allows exact computation of the stiffness matrix, mass matrix and void volume fraction; and an exact analytic expression is provided to impose affine boundary conditions on the boundary of the domain.

The averaging results obtained are applicable to any heterogeneous material in which a representative volume can be identified. The range of applications is therefore very wide and comprises the design of composites or materials with microstructure. An interesting direction for further studies is the careful determination of the size of the representative volume element for nonlinear elastodynamics. In the event of microscopic instabilities, the size of the RVE needs to be sufficient to capture the critical bifurcation mode (see for instance Geymonat et al. (1993) and Saiki et al. (2002)). An example of such an instability is the necking phenomena between neighboring voids responsible for their coalescence or the formation of shear bands and subsequently void sheet between voids at a distance comparable to their size (ans J. A. Psioda, 1975, Tvergaard, 1981b). To capture this latest stage of damage, an RVE that contains multiple voids is therefore necessary. The recent work of Henao and Mora-Corral (2010) holds promise for constructing such type of RVE.

Concerning the modeling of ductile failure, much remains to be done in order to have a full multiscale model from quantum mechanics to macroscopic fracture. There are two points of major difficulty which were not addressed in this thesis: the formal derivation of the statistical aspects of nucleation in a form ready to be input to the upper scales in the hierarchy; and predictive models of coalescence.

# Appendix A

# Exact integration of the stiffness matrix

In the case of linear elasticity for an isotropic and homogeneous material, exact integration of the stiffness matrix implies exact integration of

$$\int \frac{\partial N_{rlm}}{\partial X_i}\frac{\partial N_{spq}}{\partial X_j} R^2 \sin\Theta \, dR \, d\Theta \, d\Phi \qquad i,j = 1,2,3 \tag{A.1}$$

with

$$\begin{aligned}
\frac{\partial N_{rlm}}{\partial X_1} &= \mathcal{R}_r'(R) Y_{lm}(\Theta,\Phi)\sin\Theta\cos\Phi + \mathcal{R}_r(R)\frac{\partial Y_{lm}(\Theta,\Phi)}{\partial\Theta}\frac{\cos\Theta\cos\Phi}{R} \\
&\quad + \mathcal{R}_r(R)\frac{\partial Y_{lm}(\Theta,\Phi)}{\partial\Phi}\frac{-\sin\Phi}{R\sin\Theta} \\
\frac{\partial N_{rlm}}{\partial X_2} &= \mathcal{R}_r'(R) Y_{lm}(\Theta,\Phi)\sin\Theta\sin\Phi + \mathcal{R}_r(R)\frac{\partial Y_{lm}(\Theta,\Phi)}{\partial\Theta}\frac{\cos\Theta\sin\Phi}{R} \\
&\quad + \mathcal{R}_r(R)\frac{\partial Y_{lm}(\Theta,\Phi)}{\partial\Phi}\frac{\cos\Phi}{R\sin\Theta} \\
\frac{\partial N_{rlm}}{\partial X_3} &= \mathcal{R}_r'(R) Y_{lm}(\Theta,\Phi)\cos\Theta + \mathcal{R}_r(R)\frac{\partial Y_{lm}(\Theta,\Phi)}{\partial\Theta}\frac{-\sin\Theta}{R}
\end{aligned} \tag{A.2}$$

Separation of variables in the approximation space allows separate integration along each coordinate. The radial direction involves standard polynomials and the azimuthal direction trigonometric polynomials. For both of these cases there exist quadrature rules that provide exact integration, as described in Section 3.5.2. This appendix is devoted to the integration along the polar direction. It will be proven that a Gauss-Legendre quadrature rule under the transformation $x = \cos\Theta$ integrates exactly the non-zero values of the stiffness matrix. In the cases in which the quadrature rule in the polar direction is not exact, integration along the azimuthal direction results in a zero value, giving an

overall exact quadrature rule.

All the different integrals appearing in the computation of the stiffness matrix are analyzed in the following.

Case 1

$$\int_0^{\pi}\int_0^{2\pi} Y_{lm}(\Theta,\Phi)Y_{pq}(\Theta,\Phi)\sin^3\Theta\cos^2\Phi\,d\Theta\,d\Phi \tag{A.3}$$

Integration along $\Theta$ results in

$$\int_0^{\pi} P_l^m(\cos\Theta)P_p^q(\cos\Theta)\sin^3\Theta\,d\Theta = \int_{-1}^{1} P_l^m(x)P_p^q(x)(1-x^2)\,dx \tag{A.4}$$

under the transformation $x = \cos\Theta$. When $m+q$ is even, the integrand is a polynomial of degree at most of $2N_l+2$, and can therefore be integrated exactly with the proposed quadrature rule. When $m+q$ is odd, integration along $\Phi$ is zero.

$$\begin{aligned}
&\int_0^{2\pi}\cos(m\Phi)\cos(q\Phi)\cos^2\Phi\,d\Phi = 0\\
&\int_0^{2\pi}\sin(m\Phi)\sin(q\Phi)\cos^2\Phi\,d\Phi = 0\\
&\int_0^{2\pi}\cos(m\Phi)\sin(q\Phi)\cos^2\Phi\,d\Phi = 0\\
&\int_0^{2\pi}\sin(m\Phi)\cos(q\Phi)\cos^2\Phi\,d\Phi = 0
\end{aligned} \tag{A.5}$$

Case 2

$$\int_0^{\pi}\int_0^{2\pi} Y_{lm}(\Theta,\Phi)\frac{\partial Y_{pq}(\Theta,\Phi)}{\partial\Theta}\sin^2\Theta\cos\Theta\cos^2\Phi\,d\Theta\,d\Phi \tag{A.6}$$

Using the recurrence formula of the associated Legendre functions of varying degree (Abramowitz and Stegun, 1965), integration along $\Theta$ results in

$$\begin{aligned}
\int_0^{\pi} P_l^m(\cos\Theta)\frac{dP_p^q(\cos\Theta)}{d\Theta}\sin^2\Theta\cos\Theta\,d\Theta &= \int_{-1}^{1} P_l^m(x)P_p^{q'}(x)(x^2-1)x\,dx\\
&= \int_{-1}^{1} pP_l^m(x)P_p^q(x)x^2\,dx - \int_{-1}^{1}(p+q)P_l^m(x)P_{p-1}^q(x)x\,dx
\end{aligned} \tag{A.7}$$

When $m+q$ is even, the integrands are polynomials of degree $2N_l+2$ at most. When $m+q$ is odd, integration along $\Phi$ is zero (equivalent to Case 1).

Case 3

$$\int_0^{\pi}\int_0^{2\pi} Y_{lm}(\Theta,\Phi)\frac{\partial Y_{pq}(\Theta,\Phi)}{\partial\Phi}\sin\Theta\sin\Phi\cos\Phi\,d\Theta\,d\Phi \tag{A.8}$$

Integration along $\Theta$ results in

$$\int_0^{\pi} P_l^m(\cos\Theta)P_p^q(\cos\Theta)\sin\Theta\,d\Theta = \int_{-1}^{1} P_l^m(x)P_p^q(x)\,dx \tag{A.9}$$

When $m+q$ is even, the integrand is a polynomial of degree $2N_l$. When $m+q$ is odd, integration along $\Phi$ results in a zero value.

$$\begin{aligned}
&\int_0^{2\pi}\cos(m\Phi)\cos(q\Phi)\sin\Phi\cos\Phi\,d\Phi = 0\\
&\int_0^{2\pi}\sin(m\Phi)\sin(q\Phi)\sin\Phi\cos\Phi\,d\Phi = 0\\
&\int_0^{2\pi}\cos(m\Phi)\sin(q\Phi)\sin\Phi\cos\Phi\,d\Phi = 0\\
&\int_0^{2\pi}\sin(m\Phi)\cos(q\Phi)\sin\Phi\cos\Phi\,d\Phi = 0
\end{aligned} \tag{A.10}$$

Case 4

$$\int_0^{\pi}\int_0^{2\pi}\frac{\partial Y_{lm}(\Theta,\Phi)}{\partial\Theta}\frac{\partial Y_{pq}(\Theta,\Phi)}{\partial\Theta}\sin\Theta\cos^2\Theta\cos^2\Phi\,d\Theta\,d\Phi \tag{A.11}$$

Integration along $\Theta$ results in

$$\int_0^{\pi}\frac{dP_l^m(\cos\Theta)}{d\Theta}\frac{dP_p^q(\cos\Theta)}{d\Theta}\cos^2\Theta\sin\Theta\,d\Theta = \int_{-1}^{1} P_l^{m'}(x)P_p^{q'}(x)(1-x^2)x^2\,dx \tag{A.12}$$

When $m$ and $q$ are even, we need to integrate exactly polynomial of degree $2N_l+2$. When $m$ and $q$ are both odd

$$\begin{aligned}
&\int_{-1}^{1} P_l^{m'}(x)P_p^{q'}(x)(1-x^2)x^2\,dx = \int_{-1}^{1}\frac{d(p(x)\sqrt{1-x^2})}{dx}\frac{d(q(x)\sqrt{1-x^2})}{dx}(1-x^2)x^2\,dx\\
&= \int_{-1}^{1} p'(x)q'(x)x^2(1-x^2)^2\,dx + \int_{-1}^{1} x^4p(x)q(x)\,dx\\
&- \int_{-1}^{1} x^3(1-x^2)(p'(x)q(x)+p(x)q'(x))\,dx
\end{aligned} \tag{A.13}$$

where $p(x)$ and $q(x)$ are polynomials of degree at most $N_l-1$. The integrands are

polynomials of degree at most $2N_l + 2$. When $m + q$ is odd, integration along $\Phi$ results in a zero value (equivalent to Case 1).

Case 5

$$\int_0^{\pi} \int_0^{2\pi} \frac{\partial Y_{lm}(\Theta, \Phi)}{\partial \Theta} \frac{\partial Y_{pq}(\Theta, \Phi)}{\partial \Phi} \cos\Theta \cos\Phi \sin\Phi \, d\Theta \, d\Phi \tag{A.14}$$

Integration along $\Theta$ results in

$$\int_0^{\pi} \frac{dP_l^m(\cos\Theta)}{d\Theta} P_p^q(\cos\Theta) \cos\Theta \, d\Theta = -\int_{-1}^{1} P_l^{m'}(x) P_p^q(x) x \, dx \tag{A.15}$$

If $m$ and $q$ are even, polynomials of degree $2N_l$ need to be integrated exactly. If they are both odd

$$\begin{aligned} \int_{-1}^{1} P_l^{m'}(x) P_p^q(x) x \, dx &= \int_{-1}^{1} \frac{d(\sqrt{1-x^2}p(x))}{dx} \sqrt{1-x^2} q(x) x \, dx \\ &= \int_{-1}^{1} -x^2 p(x) q(x) \, dx + \int_{-1}^{1} (1-x^2) p'(x) x q(x) \, dx \end{aligned} \tag{A.16}$$

where $p(x)$ and $q(x)$ are polynomials of degree at most $N_l - 1$. In this case, polynomials of degree $2N_l$ need to be integrated exactly . If $m+q$ is odd, then integration along $\Phi$ is zero (equivalent to Case 3)

Case 6

$$\int_0^{\pi} \int_0^{2\pi} \frac{\partial Y_{lm}(\Theta, \Phi)}{\partial \Phi} \frac{\partial Y_{pq}(\Theta, \Phi)}{\partial \Phi} \frac{\sin^2\Phi}{\sin\Theta} \, d\Theta \, d\Phi \tag{A.17}$$

Integration along $\Theta$ results in

$$\int_0^{\pi} P_l^m(\cos\Theta) P_p^q(\cos\Theta) \frac{1}{\sin\Theta} \, d\Theta = \int_{-1}^{1} P_l^m(x) P_p^q(x) \frac{1}{1-x^2} \, dx \tag{A.18}$$

If $m$ and $q$ are both odd, polynomials of degree $2N_l - 2$ need to be integrated exactly. If they are both even and non-zero (otherwise the integral is zero), from the definition of the associated Legendre functions as a function of the Legendre polynomials (Abramowitz and Stegun, 1965), it is easy to see that the integrand is a polynomial of degree at most of $2N_l - 2$. If $m + q$ is odd, integration along $\Phi$

results in a zero value

$$\begin{aligned}
&\int_0^{2\pi} \cos(m\Phi)\cos(q\Phi)\sin^2\Phi\, d\Phi = 0 \\
&\int_0^{2\pi} \sin(m\Phi)\cos(q\Phi)\sin^2\Phi\, d\Phi = 0 \\
&\int_0^{2\pi} \sin(m\Phi)\sin(q\Phi)\sin^2\Phi\, d\Phi = 0 \\
&\int_0^{2\pi} \cos(m\Phi)\sin(q\Phi)\sin^2\Phi\, d\Phi = 0
\end{aligned} \tag{A.19}$$

Case 7

$$\int_0^{\pi}\int_0^{2\pi} Y_{lm}(\Theta,\Phi)Y_{pq}(\Theta,\Phi)\sin^3\Theta\sin^2\Phi\, d\Theta\, d\Phi \tag{A.20}$$

Integration along $\Theta$ results in

$$\int_0^{\pi} P_l^m(\cos\Theta)P_p^q(\cos\Theta)\sin^3\Theta\, d\Theta = \int_{-1}^{1} P_l^m(x)P_p^q(x)(1-x^2)\, dx \tag{A.21}$$

If $m+q$ is even, we need to integrate exactly polynomial of order $2N_l+2$. If $m+q$ is odd, then integration along $\Phi$ results in a zero value (equivalent to Case 6).

Case 8

$$\int_0^{\pi}\int_0^{2\pi} Y_{lm}(\Theta,\Phi)\frac{\partial Y_{pq}(\Theta,\Phi)}{\partial\Theta}\sin^2\Theta\cos\Theta\sin^2\Phi\, d\Theta\, d\Phi \tag{A.22}$$

Integrations along $\Theta$ and $\Phi$ are equivalent to Cases 2 and 6, respectively.

Case 9

$$\int_0^{\pi}\int_0^{2\pi} \frac{\partial Y_{lm}(\Theta,\Phi)}{\partial\Theta}\frac{\partial Y_{pq}(\Theta,\Phi)}{\partial\Theta}\cos^2\Theta\sin\Theta\sin^2\Phi\, d\Theta\, d\Phi \tag{A.23}$$

Integrations along $\Theta$ and $\Phi$ are equivalent to Cases 4 and 6, respectively.

Case 10

$$\int_0^{\pi}\int_0^{2\pi} \frac{\partial Y_{lm}(\Theta,\Phi)}{\partial\Phi}\frac{\partial Y_{pq}(\Theta,\Phi)}{\partial\Phi}\frac{\cos^2\Phi}{\sin\Theta}\, d\Theta\, d\Phi \tag{A.24}$$

Integrations along $\Theta$ and $\Phi$ are equivalent to Cases 6 and 1, respectively.

Case 11

$$\int_0^{\pi}\int_0^{2\pi} Y_{lm}(\Theta,\Phi)Y_{pq}(\Theta,\Phi)\cos^2\Theta\sin\Theta\, d\Theta\, d\Phi \tag{A.25}$$

If $m+q$ is even, polynomials of order $2N_l+2$ need to be integrated exactly. If $m+q$ is odd, integration along $\Phi$ results in a zero value.

$$\begin{aligned}
\int_0^{2\pi} \cos(m\Phi)\cos(q\Phi)\,d\Phi &= 0 \\
\int_0^{2\pi} \sin(m\Phi)\sin(q\Phi)\,d\Phi &= 0 \\
\int_0^{2\pi} \cos(m\Phi)\sin(q\Phi)\,d\Phi &= 0 \\
\int_0^{2\pi} \sin(m\Phi)\cos(q\Phi)\,d\Phi &= 0
\end{aligned} \tag{A.26}$$

Case 12

$$\int_0^{\pi}\int_0^{2\pi} Y_{lm}(\Theta,\Phi)\frac{\partial Y_{pq}(\Theta,\Phi)}{\partial\Theta}\cos\Theta\sin^2\Theta\,d\Theta\,d\Phi \tag{A.27}$$

Integrations along $\Theta$ and $\Phi$ are equivalent to Cases 2 and 11, respectively.

Case 13

$$\int_0^{\pi}\int_0^{2\pi} \frac{\partial Y_{lm}(\Theta,\Phi)}{\partial\Theta}\frac{\partial Y_{pq}(\Theta,\Phi)}{\partial\Theta}\sin^3\Theta\,d\Theta\,d\Phi \tag{A.28}$$

Integrations along $\Theta$ and $\Phi$ are equivalent to Cases 4 and 11, respectively.

Case 14

$$\int_0^{\pi}\int_0^{2\pi} Y_{lm}(\Theta,\Phi)Y_{pq}(\Theta,\Phi)\sin^3\Theta\cos\Phi\sin\Phi\,d\Theta\,d\Phi \tag{A.29}$$

Integrations along $\Theta$ and $\Phi$ are equivalent to Cases 1 and 3, respectively.

Case 15

$$\int_0^{\pi}\int_0^{2\pi} Y_{lm}(\Theta,\Phi)\frac{\partial Y_{pq}(\Theta,\Phi)}{\partial\Theta}\sin^2\Theta\cos\Theta\cos\Phi\sin\Phi\,d\Theta\,d\Phi \tag{A.30}$$

Integrations along $\Theta$ and $\Phi$ are equivalent to Cases 2 and 3, respectively.

Case 16

$$\int_0^{\pi}\int_0^{2\pi} Y_{lm}(\Theta,\Phi)\frac{\partial Y_{pq}(\Theta,\Phi)}{\partial\Phi}\sin\Theta\cos^2\Phi\,d\Theta\,d\Phi \tag{A.31}$$

Integrations along $\Theta$ and $\Phi$ are equivalent to Cases 3 and 1, respectively.

Case 17

$$\int_0^{\pi}\int_0^{2\pi} \frac{\partial Y_{lm}(\Theta,\Phi)}{\partial\Theta}\frac{\partial Y_{pq}(\Theta,\Phi)}{\partial\Theta}\cos^2\Theta\sin\Theta\cos\Phi\sin\Phi\,d\Theta\,d\Phi \tag{A.32}$$

Integrations along $\Theta$ and $\Phi$ are equivalent to Cases 4 and 3, respectively.

Case 18

$$\int_0^{\pi}\int_0^{2\pi} \frac{\partial Y_{lm}(\Theta,\Phi)}{\partial\Theta}\frac{\partial Y_{pq}(\Theta,\Phi)}{\partial\Phi}\cos\Theta\cos^2\Phi\, d\Theta\, d\Phi \tag{A.33}$$

Integrations along $\Theta$ and $\Phi$ are equivalent to Cases 5 and 1, respectively.

Case 19

$$\int_0^{\pi}\int_0^{2\pi} \frac{\partial Y_{lm}(\Theta,\Phi)}{\partial\Phi}Y_{pq}(\Theta,\Phi)\sin\Theta\sin^2\Phi\, d\Theta\, d\Phi \tag{A.34}$$

Integrations along $\Theta$ and $\Phi$ are equivalent to Cases 3 and 6, respectively.

Case 20

$$\int_0^{\pi}\int_0^{2\pi} \frac{\partial Y_{lm}(\Theta,\Phi)}{\partial\Phi}\frac{\partial Y_{pq}(\Theta,\Phi)}{\partial\Theta}\cos\Theta\sin^2\Phi\, d\Theta\, d\Phi \tag{A.35}$$

Integrations along $\Theta$ and $\Phi$ are equivalent to Cases 5 and 6, respectively.

Case 21

$$\int_0^{\pi}\int_0^{2\pi} \frac{\partial Y_{lm}(\Theta,\Phi)}{\partial\Phi}\frac{\partial Y_{pq}(\Theta,\Phi)}{\partial\Phi}\frac{1}{\sin\Theta}\cos\Phi\sin\Phi\, d\Theta\, d\Phi \tag{A.36}$$

Integrations along $\Theta$ and $\Phi$ are equivalent to Cases 6 and 3, respectively.

Case 22

$$\int_0^{\pi}\int_0^{2\pi} Y_{lm}(\Theta,\Phi)Y_{pq}(\Theta,\Phi)\sin^2\Theta\cos\Theta\cos\Phi\, d\Theta\, d\Phi \tag{A.37}$$

Integrations along $\Theta$ results in

$$\int_0^{\pi} P_l^m(\cos\Theta)P_p^q(\cos\Theta)\sin^2\Theta\cos\Theta\, d\Theta = \int_{-1}^{1} P_l^m(x)P_p^q(x)x\sqrt{1-x^2}\, dx \tag{A.38}$$

If $m+q$ is odd, polynomials of degree $2N_l+1$ need to be integrated exactly. If $m+q$ is even, integration along $\Phi$ results in zero value

$$\begin{aligned}
&\int_0^{2\pi}\cos(m\Phi)\cos(q\Phi)\cos\Phi\, d\Phi = 0\\
&\int_0^{2\pi}\sin(m\Phi)\sin(q\Phi)\cos\Phi\, d\Phi = 0\\
&\int_0^{2\pi}\cos(m\Phi)\sin(q\Phi)\cos\Phi\, d\Phi = 0\\
&\int_0^{2\pi}\sin(m\Phi)\cos(q\Phi)\cos\Phi\, d\Phi = 0
\end{aligned} \tag{A.39}$$

Case 23

$$\int_0^{\pi}\int_0^{2\pi} Y_{lm}(\Theta,\Phi)\frac{\partial Y_{pq}(\Theta,\Phi)}{\partial\Theta}\sin^3\Theta\cos\Phi\,d\Theta\,d\Phi \tag{A.40}$$

Integrations along $\Theta$ results in

$$\int_0^{\pi} P_l^m(\cos\Theta)\frac{dP_p^q(\cos\Theta)}{d\Theta}\sin^3\Theta\,d\Theta = -\int_{-1}^{1} P_l^m(x)P_p^{q'}(x)(1-x^2)\sqrt{1-x^2}\,dx \tag{A.41}$$

If $m+q$ is odd, polynomials of degree $2N_l+2$ need to be integrated exactly. If $m+q$ is even integration over $\Phi$ is equivalent to Case 22.

Case 24

$$\int_0^{\pi}\int_0^{2\pi} \frac{\partial Y_{lm}(\Theta,\Phi)}{\partial\Theta}Y_{pq}(\Theta,\Phi)\cos^2\Theta\sin\Theta\cos\Phi\,d\Theta\,d\Phi \tag{A.42}$$

Integrations along $\Theta$ results in

$$\int_0^{\pi} \frac{dP_l^m(\cos\Theta)}{d\Theta}P_p^q(\cos\Theta)\cos^2\Theta\sin\Theta\,d\Theta = -\int_{-1}^{1} P_l^{m'}(x)P_p^q(x)x^2\sqrt{1-x^2}\,dx \tag{A.43}$$

If $m$ is even and $q$ is odd, polynomials of degree $2N_l+2$ need to be integrate exactly. If $m$ odd and $q$ even

$$\begin{aligned}&\int_{-1}^{1} P_l^{m'}(x)P_p^q(x)x^2\sqrt{1-x^2}\,dx = \int_{-1}^{1}\frac{d(p(x)\sqrt{1-x^2})}{dx}q(x)x^2\sqrt{1-x^2}\,dx\\ &= \int_{-1}^{1} x^2(1-x^2)p'(x)q(x)\,dx - \int_{-1}^{1} x^3p(x)q(x)\,dx\end{aligned} \tag{A.44}$$

where $p(x)$ and $q(x)$ are polynomials of degree at most $N_l-1$ and $N_l$ respectively. The integrands are then polynomials of degree at most of $2N_l+2$. If $m+q$ is even, integration along $\Phi$ is equivalent to Case 22.

Case 25

$$\int_0^{\pi}\int_0^{2\pi} \frac{\partial Y_{lm}(\Theta,\Phi)}{\partial\Theta}\frac{\partial Y_{pq}(\Theta,\Phi)}{\partial\Theta}\cos\Theta\sin^2\Theta\cos\Phi\,d\Theta\,d\Phi \tag{A.45}$$

Integration along $\Theta$ results in

$$\int_0^{\pi} \frac{dP_l^m(\cos\Theta)}{d\Theta}\frac{dP_p^q(\cos\Theta)}{d\Theta}\cos\Theta\sin^2\Theta\,d\Theta = \int_{-1}^{1} P_l^{m'}(x)P_p^{q'}(x)(1-x^2)\sqrt{1-x^2}x\,dx \tag{A.46}$$

If $m+q$ is odd, it results in

$$\begin{aligned}&\int_{-1}^{1} \frac{dp(x)\sqrt{1-x^2}}{dx} q'(x)(1-x^2)\sqrt{1-x^2}x\,dx \\ &= \int_{-1}^{1} p'(x)q'(x)(1-x^2)^2 x\,dx - \int_{-1}^{1} p(x)q'(x)x^2(1-x^2)\,dx\end{aligned} \tag{A.47}$$

where $p(x)$ and $q(x)$ are polynomials of degree at most $N_l - 1$ and $N_l$, respectively. The integrands are then polynomials of degree at most $2N_l + 2$. If $m+q$ is even, integration over $\Phi$ leads to a zero value (equivalent to Case 22).

Case 26

$$\int_0^{\pi}\int_0^{2\pi} \frac{\partial Y_{lm}(\Theta,\Phi)}{\partial\Phi} Y_{pq}(\Theta,\Phi)\cos\Theta\sin\Phi\,d\Theta\,d\Phi \tag{A.48}$$

Integration along $\Theta$ becomes

$$\int_0^{\pi} P_l^m(\cos\Theta)P_p^q(\cos\Theta)\cos\Theta\,d\Theta = \int_{-1}^{1} P_l^m(x)P_p^q(x)x\frac{1}{\sqrt{1-x^2}}\,dx \tag{A.49}$$

If $m+q$ is odd, need to integrate exactly polynomial of degree $2N_l$. If $m+q$ is even, integration along $\Phi$ leads to a zero value

$$\begin{aligned}&\int_0^{2\pi}\cos(m\Phi)\cos(q\Phi)\sin\Phi\,d\Phi = 0 \\ &\int_0^{2\pi}\sin(m\Phi)\sin(q\Phi)\sin\Phi\,d\Phi = 0 \\ &\int_0^{2\pi}\cos(m\Phi)\sin(q\Phi)\sin\Phi\,d\Phi = 0 \\ &\int_0^{2\pi}\sin(m\Phi)\cos(q\Phi)\sin\Phi\,d\Phi = 0\end{aligned} \tag{A.50}$$

Case 27

$$\int_0^{\pi}\int_0^{2\pi} \frac{\partial Y_{lm}(\Theta,\Phi)}{\partial\Phi}\frac{\partial Y_{pq}(\Theta,\Phi)}{\partial\Theta}\sin\Theta\sin\Phi\,d\Theta\,d\Phi \tag{A.51}$$

Integration along $\Theta$ becomes

$$\int_0^{\pi} P_l^m(\cos\Theta)\frac{dP_p^q(\cos\Theta)}{d\Theta}\sin\Theta\,d\Theta = -\int_{-1}^{1} P_l^m(x)P_p^{q'}(x)\sqrt{1-x^2}\,dx \tag{A.52}$$

If $m$ is odd and $q$ is even, polynomials of degree $2N_l$ need to be integrated exactly.

If $m$ is even and $q$ odd

$$\begin{aligned}&\int_{-1}^{1} q(x)\frac{d(p(x)\sqrt{1-x^2})}{dx}\sqrt{1-x^2}\,dx \\ &= \int_{-1}^{1} q(x)p'(x)(1-x^2)\,dx - \int_{-1}^{1} q(x)p(x)x\,dx\end{aligned} \tag{A.53}$$

where $p(x)$ and $q(x)$ are polynomials of degree $N_l - 1$ and $N_l$, respectively. The integrands are polynomials of degree at most $2N_l$. If $m+q$ is even, integration over $\Phi$ is equivalent to Case 26.

Case 28

$$\int_0^{\pi}\int_0^{2\pi} Y_{lm}(\Theta,\Phi)Y_{pq}(\Theta,\Phi)\sin^2\Theta\cos\Theta\sin\Phi\,d\Theta\,d\Phi \tag{A.54}$$

Integrations along $\Theta$ and $\Phi$ are equivalent to the Cases 22 and 26 respectively.

Case 29

$$\int_0^{\pi}\int_0^{2\pi} Y_{lm}(\Theta,\Phi)\frac{\partial Y_{pq}(\Theta,\Phi)}{\partial\Theta}\sin^3\Theta\sin\Phi\,d\Theta\,d\Phi \tag{A.55}$$

Integrations along $\Theta$ and $\Phi$ are equivalent to the Cases 23 and 26 respectively.

Case 30

$$\int_0^{\pi}\int_0^{2\pi} \frac{\partial Y_{lm}(\Theta,\Phi)}{\partial\Theta}Y_{pq}(\Theta,\Phi)\cos^2\Theta\sin\Theta\sin\Phi\,d\Theta\,d\Phi \tag{A.56}$$

Integrations along $\Theta$ and $\Phi$ are equivalent to the Cases 24 and 26 respectively.

Case 31

$$\int_0^{\pi}\int_0^{2\pi} \frac{\partial Y_{lm}(\Theta,\Phi)}{\partial\Theta}\frac{\partial Y_{pq}(\Theta,\Phi)}{\partial\Theta}\cos\Theta\sin^2\Theta\sin\Phi\,d\Theta\,d\Phi \tag{A.57}$$

Integrations along $\Theta$ and $\Phi$ are equivalent to the Cases 25 and 26 respectively.

Case 32

$$\int_0^{\pi}\int_0^{2\pi} \frac{\partial Y_{lm}(\Theta,\Phi)}{\partial\Phi}Y_{pq}(\Theta,\Phi)\cos\Theta\cos\Phi\,d\Theta\,d\Phi \tag{A.58}$$

Integrations along $\Theta$ and $\Phi$ are equivalent to the Cases 26 and 22 respectively.

Case 33

$$\int_0^{\pi}\int_0^{2\pi} \frac{\partial Y_{lm}(\Theta,\Phi)}{\partial\Phi}\frac{\partial Y_{pq}(\Theta,\Phi)}{\partial\Theta}\sin\Theta\cos\Phi\,d\Theta\,d\Phi \tag{A.59}$$

Integrations along $\Theta$ and $\Phi$ are equivalent to the Cases 27 and 22 respectively.

Exact integration of the stiffness matrix requires an exact integration of polynomials of degree $2N_l + 2$ in the $\Theta$ direction and trigonometric polynomial of degree $2N_l + 2$ in the $\Phi$ direction. This can be achieved with

$$\begin{aligned} N_{q\Theta} &= N_l + 2 \\ N_{q\Phi} &= 2N_l + 3 \end{aligned} \tag{A.60}$$

# Appendix B

# Exact integration of the mass matrix

In the case of linear elasticity, for an isotropic and homogeneous material, exact integration of the mass matrix implies exact integration of

$$\int \partial N_{rlm} \partial N_{spq} R^2 \sin\Theta \, dR \, d\Theta \, d\Phi = \left( \int_a^b R_r(R) R_s(R) R^2 \, dR \right) \left( \int_0^\pi \int_0^{} 2\pi Y_{lm} Y_{pq} \sin(\Theta) \, d\Theta \, d\Phi \right) \tag{B.1}$$

Similar to the analysis for the stiffness matrix, integration along each coordinate is analyzed independently. The radial direction requires the integration of polynomials of order 4, if linear shape functions are used, requiring 3 quadrature points per layer. This leads to a total number of $N_{qr} = 3N_r$ for the entire hollow sphere.

In direction $\Theta$, the integrals are of the type

$$\int_0^\pi P_l^m(\cos\Theta) P_p^q(\cos\Theta) \sin(\Theta) \, d\Theta = \int_{-1}^1 P_l^m(x) P_p^q(x) \, dx \tag{B.2}$$

where the change of variables $x = \cos(\Theta)$ has been used. If $m+q$ is even, the integrand is a polynomial of degree at most $2N_l$, requiring $N_{q\Theta} = N_l + 1$. If $m+q$ is odd, integration

along $\Phi$ results in a zero value

$$\begin{aligned}
&\int_0^{2\pi} \cos(m\Phi)\cos(q\Phi)\, d\Phi = 0 \\
&\int_0^{2\pi} \sin(m\Phi)\sin(q\Phi)\, d\Phi = 0 \\
&\int_0^{2\pi} \cos(m\Phi)\sin(q\Phi)\, d\Phi = 0 \\
&\int_0^{2\pi} \sin(m\Phi)\cos(q\Phi)\, d\Phi = 0
\end{aligned} \tag{B.3}$$

These integrals can be performed exactly. The highest degree of the trigonometric polynomials encountered in the integration of the mass matrix is $2N_l$. The number of equally spaced quadrature points required for exact integration is $N_{q\Phi} = 2N_l + 1$

# Appendix C

# Void volume fraction

A common damage parameter in porous material models is the void volume fraction. It is therefore desirable to evaluate that quantity with a bounded error. It will be proven in this section that the proposed quadrature rule allows its exact evaluation, as well.

The void volume fraction is the ratio between the volume enclosed by the outer surface and the inner surface in the deformed configuration. The final volume enclosed by a surface of initial radius $\bar{R}$, for all cases in which $r(\theta, \varphi) = r\left(\theta(\bar{R}, \Theta, \Phi), \varphi(\bar{R}, \Theta, \Phi)\right)$ is a function, is (see Fig. C )

$$V = \int_{\theta=0}^{\pi} \int_{\varphi=0}^{2\pi} \int_{r'=0}^{r} r'^2 \sin\theta \, dr' \, d\theta \, d\varphi = \int_{\theta=0}^{\pi} \int_{\varphi=0}^{2\pi} \frac{r^3}{3} \sin\theta \, d\theta \, d\varphi \tag{C.1}$$

One can express this integral using the coordinates from the undeformed configuration

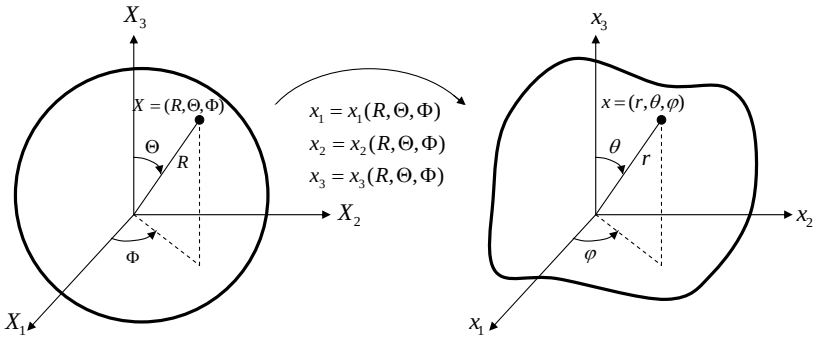


Figure C.1: Final configuration of an initially spherical surface.

using the relations

$$\begin{aligned}\theta(\Theta,\Phi) &= \arccos\left(\frac{x_3(\Theta,\Phi)}{\sqrt{x_1^2(\Theta,\Phi)+x_2^2(\Theta,\Phi)+x_3^2(\Theta,\Phi)}}\right)\\ \varphi(\Theta,\Phi) &= \arctan\left(\frac{x_2(\Theta,\Phi)}{x_1(\Theta,\Phi)}\right)\end{aligned} \tag{C.2}$$

where $x_i(\Theta,\Phi) = x_i(\bar{R},\Theta,\Phi)$, as defined in Eq. 3.101.

The final volume enclosed by the surface is then

$$\begin{aligned}V &= \int_{\Theta=0}^{\pi}\int_{\Phi=0}^{2\pi}\frac{x_1^2(\Theta,\Phi)+x_2^2(\Theta,\Phi)+x_3^2(\Theta,\Phi)}{3}\sqrt{x_1^2(\Theta,\Phi)+x_2^2(\Theta,\Phi)}|J(\Theta,\Phi)|\,d\Theta\,d\Phi\\ &= \int_{\Theta=0}^{\pi}\int_{\Phi=0}^{2\pi}\frac{1}{3}\left[\frac{\partial x_3}{\partial\Phi}\left(-x_2\frac{\partial x_1}{\partial\Theta}+x_1\frac{\partial x_2}{\partial\Theta}\right)+x_3\left(\frac{\partial x_2}{\partial\Phi}\frac{\partial x_1}{\partial\Theta}-\frac{\partial x_1}{\partial\Phi}\frac{\partial x_2}{\partial\Theta}\right)+\frac{\partial x_3}{\partial\Theta}\left(x_2\frac{\partial x_1}{\partial\Phi}-x_1\frac{\partial x_2}{\partial\Phi}\right)\right]d\Theta\end{aligned} \tag{C.3}$$

where $|J(\Theta,\Phi)| = |\frac{\partial(\theta,\varphi)}{\partial(\Theta,\Phi)}|$

## C.1 Exact integration

The terms involved in the computation of the void volume fraction (C.3) are of the type

$$\int_{\Theta=0}^{\pi}\int_{\Phi=0}^{2\pi}\frac{\partial Y_{rs}}{\partial\Phi}Y_{pq}\frac{\partial Y_{lm}}{\partial\Theta}\,d\Theta\,d\Phi \tag{C.4}$$

Integration along the $\Theta$ direction under transformation $x = \cos\Theta$ results in

$$\int_0^{\pi}P_r^s(\cos\Theta)P_p^q(\cos\Theta)\frac{dP_l^m(\cos\Theta)}{d\Theta}\,d\Theta = -\int_{-1}^{1}P_r^s(x)P_p^q(x)P_l^{m'}(x)\,dx \tag{C.5}$$

- If $m$ and $s+q$ are even, polynomials of degree $3N_l-1$ need to be integrated exactly.

- If $m$ and $s+q$ are odd, the integrand is a polynomial of degree at most of $3N_l-2$.

Note

$$
\begin{aligned}
&P_l^m(x) = \sqrt{1-x^2}p(x) \\
&P_l^{m'}(x) = \frac{1}{\sqrt{1-x^2}}\left[(1-x^2)p'(x) - xp(x)\right] \\
&P_r^s(x)P_p^q(x) = q(x)\sqrt{1-x^2} \\
&\int_{-1}^{1} P_r^s(x)P_p^q(x)P_l^{m'}(x)\,dx = \int_{-1}^{1} q(x)\left[(1-x^2)p'(x) - xp(x)\right]\,dx
\end{aligned}
\tag{C.6}
$$

where $p(x)$ and $q(x)$ are polynomials of degree at most of $N_l - 1$ and $2N_l - 2$, respectively.

- If $m$ is even and $(s+q)$ is odd, or vice versa, then integration along $\Phi$ results in a zero value

$$
\begin{aligned}
&\int_0^{2\pi} \cos(s\Phi)\cos(q\Phi)\cos(m\Phi)\,d\Phi = 0 \\
&\int_0^{2\pi} \cos(s\Phi)\cos(q\Phi)\sin(m\Phi)\,d\Phi = 0 \\
&\int_0^{2\pi} \cos(s\Phi)\sin(q\Phi)\cos(m\Phi)\,d\Phi = 0 \\
&\int_0^{2\pi} \cos(s\Phi)\sin(q\Phi)\sin(m\Phi)\,d\Phi = 0 \\
&\int_0^{2\pi} \sin(s\Phi)\sin(q\Phi)\cos(m\Phi)\,d\Phi = 0 \\
&\int_0^{2\pi} \sin(s\Phi)\sin(q\Phi)\sin(m\Phi)\,d\Phi = 0
\end{aligned}
\tag{C.7}
$$

Exact integration of the void volume fraction requires an exact integration of a polynomial of degree $3N_l - 1$ in the $\Theta$ direction and trigonometric polynomial of degree $3N_l$ in the $\Phi$ direction. This can be achieved with the proposed quadrature rule and the following number of quadrature points

$$
\begin{aligned}
&N_{q\Theta} \geq \frac{3N_l}{2} \\
&N_{q\Phi} = 3N_l + 1
\end{aligned}
\tag{C.8}
$$

# Appendix D

# Viscoelastic parameters in a relaxation test. Incompressible case

This appendix is concerned with the determination of viscoelastic parameters from experimental uniaxial relaxation tests in the limit of infinitesimal strain. In particular for this section, the material is assumed to be incompressible and to follow the following stress-strain relation

$$\sigma_{ij} = 2\mu_\infty + p\delta_{ij} + \sum_\alpha 2\mu_\alpha \left(\varepsilon_{ij} - \varepsilon_{ij}^{p,\alpha}\right) \tag{D.1}$$

where $\varepsilon_{ij}^{p,\alpha}$ are internal variables associated to the viscoelastic processes.

The parameters of the model are obtained by term to term comparison with the relaxation behavior, represented as

$$E(t) = E_\infty + \sum_{\alpha=1}^{18} E_\alpha e^{-t/\tau_\alpha} \tag{D.2}$$

where $E_\infty$ and $E_\alpha$ are given by fitting to experimental relaxation curves (see for instance Knauss and Zhao (2007))

The relaxation curve for the constitutive law in Eq. D.1, is derived by imposing a constant strain (step function) on a given direction ($\varepsilon_{11} = \text{constant}$), leaving $\sigma_{22} = \sigma_{33} = 0$. By incompressibility

$$\varepsilon = \varepsilon^{\text{dev}} = \begin{pmatrix} \varepsilon_{11} & 0 & 0 \\ 0 & -\frac{1}{2}\varepsilon_{11} & 0 \\ 0 & 0 & -\frac{1}{2}\varepsilon_{11} \end{pmatrix} \tag{D.3}$$

The evolution equations for the internal variables are

$$\begin{aligned} \dot{\varepsilon}_{11}^{p,\alpha} &= \frac{\varepsilon_{11} - \varepsilon_{11}^{p,\alpha}}{\tau^{\alpha}} \\ \dot{\varepsilon}_{22}^{p,\alpha} &= \frac{-\frac{1}{2}\varepsilon_{11} - \varepsilon_{22}^{p,\alpha}}{\tau^{\alpha}} \end{aligned} \tag{D.4}$$

Integration with respect to time leads

$$\begin{aligned} \varepsilon_{11}^{p,\alpha} &= \varepsilon_{11}\left(1 - e^{-t/\tau^{\alpha}}\right) \\ \varepsilon_{22}^{p,\alpha} &= -\frac{1}{2}\varepsilon_{11}\left(1 - e^{-t/\tau^{\alpha}}\right) \end{aligned} \tag{D.5}$$

On the other hand, the constitutive law on the two directions give

$$\begin{aligned} \sigma_{11} &= 2\mu_{\infty}\epsilon_{11} + \frac{1}{3}\sigma_{11} + \sum_{\alpha} 2\mu_{\alpha}\left(\varepsilon_{11} - \varepsilon_{11}^{p,\alpha}\right) \\ 0 &= -\mu_{\infty}\epsilon_{11} + \frac{1}{3}\sigma_{11} + \sum_{\alpha} 2\mu_{\alpha}\left(-\frac{1}{2}\varepsilon_{11} - \varepsilon_{22}^{p,\alpha}\right) \end{aligned} \tag{D.6}$$

Both equations combined with the temporal evolution of the internal variables provide the desired uniaxial material behavior

$$\sigma_{11} = 3\mu_{\infty}\varepsilon_{11} + \sum_{\alpha} 3\mu_{\alpha}\varepsilon_{11}e^{-t/\tau^{\alpha}} \tag{D.7}$$

By comparison with equation (D.2) the expected values are obtained

$$\begin{aligned} \mu_{\infty} &= \frac{E_{\infty}}{3} \\ \mu_{\alpha} &= \frac{E_{\alpha}}{3} \end{aligned} \tag{D.8}$$

# Appendix E

# Non-constant value of the Poisson's ratio for a compressible viscoelastic material

In this section it will be proven by contradiction that the Poisson's ratio, if different from 0.5, cannot be a constant for a material with constitutive law given by

$$\sigma_{ij} = 2\mu_\infty + \lambda_\infty \varepsilon_{kk}\delta_{ij} + \sum_\alpha 2\mu_\alpha \left(\varepsilon_{ij} - \varepsilon_{ij}^{p,\alpha}\right) \tag{E.1}$$

Let's impose in a similar manner as in Appendix D a step function as a strain on a given direction ($\varepsilon_{11}$). If the Poisson's ratio of the material is a constant $\nu$, then

$$\varepsilon = \begin{pmatrix} \varepsilon_{11} & 0 & 0 \\ 0 & -\nu\varepsilon_{11} & 0 \\ 0 & 0 & -\nu\varepsilon_{11} \end{pmatrix}, \quad \varepsilon^{\text{dev}} = \begin{pmatrix} \frac{2(1+\nu)}{3}\varepsilon_{11} & 0 & 0 \\ 0 & -\frac{(1+\nu)}{3}\varepsilon_{11} & 0 \\ 0 & 0 & -\frac{(1+\nu)}{3}\varepsilon_{11} \end{pmatrix}, \tag{E.2}$$

The temporal evolution of the internal variables are

$$\begin{aligned} \dot{\varepsilon}_{11}^{p,\alpha} &= \frac{\frac{2(1+\nu)}{3}\varepsilon_{11} - \varepsilon_{11}^{p,\alpha}}{\tau^\alpha} \\ \dot{\varepsilon}_{22}^{p,\alpha} &= \frac{-\frac{(1+\nu)}{3}\varepsilon_{11} - \varepsilon_{22}^{p,\alpha}}{\tau^\alpha} \end{aligned} \tag{E.3}$$

which integrated with respect to time give

$$\begin{aligned} \varepsilon_{11}^{p,\alpha} &= \frac{2(1+\nu)}{3}\varepsilon_{11}\left(1-e^{-t/\tau^{\alpha}}\right) \\ \varepsilon_{22}^{p,\alpha} &= \frac{-(1+\nu)}{3}\varepsilon_{11}\left(1-e^{-t/\tau^{\alpha}}\right) \end{aligned} \tag{E.4}$$

The constitutive law can now be written as

$$\begin{aligned} \sigma_{11} &= 2\mu_{\infty}\varepsilon_{11} + \lambda_{\infty}(1-2\nu)\varepsilon_{11} + \sum_{\alpha} 2\mu_{\alpha}\left[\frac{2(1+\nu)}{3}\varepsilon_{11} - \varepsilon_{11}^{p,\alpha}\right] \\ 0 &= -2\mu_{\infty}\nu\varepsilon_{11} + \lambda_{\infty}(1-2\nu)\varepsilon_{11} + \sum_{\alpha} 2\mu_{\alpha}\left[-\frac{(1+\nu)}{3}\varepsilon_{11} - \varepsilon_{22}^{p,\alpha}\right] \end{aligned} \tag{E.5}$$

Equivalently,

$$\begin{aligned} \sigma_{11} &= 2\mu_{\infty}\varepsilon_{11} + \lambda_{\infty}(1-2\nu)\varepsilon_{11} + \sum_{\alpha} 2\mu_{\alpha}\frac{2(1+\nu)}{3}\varepsilon_{11}e^{-t/\tau^{\alpha}} \\ 0 &= -2\mu_{\infty}\nu\varepsilon_{11} + \lambda_{\infty}(1-2\nu)\varepsilon_{11} - \sum_{\alpha} 2\mu_{\alpha}\frac{(1+\nu)}{3}\varepsilon_{11}e^{-t/\tau^{\alpha}} \end{aligned} \tag{E.6}$$

The second equation cannot hold for a finite value of $\varepsilon_{11}$. This indicates that satisfaction of the stress-free condition on directions 2 and 3 necessitates a Poisson's ratio that is time dependent, so that the temporal evolution of the internal variables can be accommodated. This case is treated in the following appendix.

# Appendix F

# Exact viscoelastic parameters for a compressible material

In this section, the case of a compressible material with a non-constant Poisson's ratio is considered. The material is assumed to obey the constitutive law given by Eq. E.1, where $\mu_\infty$, $\lambda_\infty$ and $\mu_\alpha$ are constants.

Let's impose the following deformation

$$\varepsilon = \begin{pmatrix} \varepsilon_{11} & 0 & 0 \\ 0 & -\nu\varepsilon_{11} + \delta\varepsilon_{22} & 0 \\ 0 & 0 & -\nu\varepsilon_{11} + \delta\varepsilon_{22} \end{pmatrix}, \tag{F.1}$$

$$\varepsilon^{\text{dev}} = \begin{pmatrix} \frac{2(1+\nu)}{3}\varepsilon_{11} - \frac{2}{3}\delta\varepsilon_{22} & 0 & 0 \\ 0 & -\frac{(1+\nu)}{3}\varepsilon_{11} + \frac{1}{3}\delta\varepsilon_{22} & 0 \\ 0 & 0 & -\frac{(1+\nu)}{3}\varepsilon_{11} + \frac{1}{3}\delta\varepsilon_{22} \end{pmatrix} \tag{F.2}$$

where $\nu$ and $\varepsilon_{11}$ are constant and $\delta\varepsilon_{22}$ is time dependent.

The constitutive law in two of the principal directions, under uniaxial stress, is

$$\begin{aligned} \sigma_{11} &= 2\mu_\infty\varepsilon_{11} + \lambda_\infty\left[(1-2\nu)\varepsilon_{11} + 2\delta\varepsilon_{22}\right] + \sum_\alpha 2\mu_\alpha\left[\frac{2(1+\nu)}{3}\varepsilon_{11} - \frac{2}{3}\delta\varepsilon_{22} - \varepsilon_{11}^{p,\alpha}\right] \\ 0 &= 2\mu_\infty(-\nu\varepsilon_{11} + \delta\varepsilon_{22}) + \lambda_\infty\left[(1-2\nu)\varepsilon_{11} + 2\delta\varepsilon_{22}\right] + \sum_\alpha 2\mu_\alpha\left[\frac{-(1+\nu)}{3}\varepsilon_{11} + \frac{1}{3}\delta\varepsilon_{22} - \varepsilon_{22}^{p,\alpha}\right] \end{aligned} \tag{F.3}$$

The exact values of $\mu_\alpha$ can be computed from the value of the stresses at $t = 0^+$. At

that time, $\varepsilon_{11}^{p,\alpha} = \varepsilon_{22}^{p,\alpha} = 0$, and therefore

$$\begin{aligned}
\delta\varepsilon_{22}(t=0^+) &= \frac{\frac{(1+\nu)}{3}\sum_\alpha \mu_\alpha + \nu\mu_\infty - \frac{\lambda_\infty}{2}(1-2\nu)}{\mu_\infty + \lambda_\infty + \frac{1}{3}\sum_\alpha \mu_\alpha}\varepsilon_{11} \\
\sigma_{11}(t=0^+) &= \left[2\mu_\infty + \lambda_\infty(1-2\nu) + \frac{4(1+\nu)}{3}\sum_\alpha \mu_\alpha\right]\varepsilon_{11} + \left[2\lambda_\infty - \frac{4\sum_\alpha \mu_\alpha}{3}\right]\delta\varepsilon_{22}(t=0^+)
\end{aligned} \tag{F.4}$$

The value of $\sigma_{11}(t=0^+)$ can be compared to

$$\sigma_{11}(t=0^+) = \left[E_\infty + \sum_\alpha E_\alpha\right]\varepsilon_{11} \tag{F.5}$$

which provides the desired relations

$$\begin{aligned}
E_\infty &= 2\mu_\infty + \lambda_\infty(1-2\nu) \\
0 &= \nu\mu_\infty - \frac{\lambda_\infty}{2}(1-2\nu) \\
E_\alpha &= \frac{2(1+\nu)}{3}\mu_\alpha \frac{2\mu_\infty + 3\lambda\infty}{\mu_\infty + \lambda_\infty + \frac{1}{3}\sum_\beta \mu_\beta}
\end{aligned} \tag{F.6}$$

From the first two equations it is obtained that

$$\begin{aligned}
\lambda_\infty &= \frac{E_\infty \nu}{(1+\nu)(1-2\nu)} \\
\mu_\infty &= \frac{E_\infty}{2(1+\nu)}
\end{aligned} \tag{F.7}$$

Note that if the material is quasi-incompressible

$$\begin{aligned}
&\frac{2\mu_\infty + 3\lambda\infty}{\mu_\infty + \lambda_\infty + \frac{1}{3}\sum_\alpha \mu_\alpha} \to 3 \\
&E_\alpha \to 2(1+\nu)\mu_\alpha
\end{aligned} \tag{F.8}$$

the standard relation between the material parameters hold.

### F.0.1 Exact relaxation curve with one term of the Prony series

In this subsection the exact relaxation curve is derived for the case in which a single term in the Prony series is considered. The same procedure can be applied for multiple relaxation mechanisms, although the equations are highly coupled and the analytic solution increases in complexity.

The constitutive law in the transverse direction is

$$0 = (2\mu_\infty + 2\lambda_\infty)\,\delta\varepsilon_{22} + 2\mu_\alpha\left[\frac{-(1+\nu)}{3}\varepsilon_{11} + \frac{1}{3}\delta\varepsilon_{22} - \varepsilon_{22}^{p,\alpha}\right] \tag{F.9}$$

Taking derivatives, it is readily obtained that

$$\dot{\varepsilon}_{22}^{p,\alpha} = \frac{\mu_\infty + \lambda_\infty + \frac{1}{3}\mu_\alpha}{\mu_\alpha}\delta\dot{\varepsilon}_{22} \tag{F.10}$$

which combined with the evolution law of $\varepsilon_{22}^{p,\alpha}$ and the transversal equilibrium equation, leads to

$$\delta\varepsilon_{22} = \delta\varepsilon_{22}(t=0^+)e^{-\frac{t}{\tau^\alpha}\frac{\mu_\infty+\lambda_\infty}{\mu_\infty+\lambda_\infty+\frac{\mu_\alpha}{3}}} = \delta\varepsilon_{22}(t=0^+)e^{\frac{-t}{\bar{\tau}^\alpha}} \tag{F.11}$$

with $\bar{\tau}^\alpha = \tau^\alpha\frac{\mu_\infty+\lambda_\infty+\frac{1}{3}\mu_\alpha}{\mu_\infty+\lambda_\infty}$. Note that in the incompressible limit $\bar{\tau}^\alpha \to \tau^\alpha$.

The evolution law for $\varepsilon_{11}^{p,\alpha}$ can now be derived

$$\tau^\alpha\dot{\varepsilon}_{11}^{p,\alpha} = \frac{2(1+\nu)}{3}\varepsilon_{11} - \frac{2}{3}\delta\varepsilon_{22} - \varepsilon_{11}^{p,\alpha} \tag{F.12}$$

Integrating with respect to time,

$$\varepsilon_{11}^{p,\alpha} = \frac{2(1+\nu)}{3}\varepsilon_{11}\left(1 - e^{-t/\tau^\alpha}\right) + \frac{2}{3}\frac{\delta\varepsilon_{22}(t=0^+)}{\left(\frac{\tau^\alpha}{\bar{\tau}^\alpha}-1\right)}\left(e^{-t/\bar{\tau}^\alpha} - e^{-t/\tau^\alpha}\right) \tag{F.13}$$

The evolution of the stresses can finally be obtained by combining all these results into the constitutive equation in the first principal direction

$$\begin{aligned}\frac{\sigma_{11}(t)}{\varepsilon_{11}} = E_\infty &+ \frac{4(1+\nu)}{3}\mu_\alpha e^{-t/\tau^\alpha} + \left(2\lambda_\infty - \frac{4}{3}\mu_\alpha\right)\frac{\delta\varepsilon_{22}(t=0^+)}{\varepsilon_{11}}e^{-t/\bar{\tau}^\alpha} \\ &- \frac{4}{3}\mu_\alpha\frac{1}{\left(\frac{\tau^\alpha}{\bar{\tau}^\alpha}-1\right)}\frac{\delta\varepsilon_{22}(t=0^+)}{\varepsilon_{11}}\left(e^{-t/\bar{\tau}^\alpha} - e^{-t/\tau^\alpha}\right)\end{aligned} \tag{F.14}$$

In the incompressible limit

$$\begin{aligned}
&\bar{\tau}^{\alpha} \to \tau^{\alpha} \\
&\delta\varepsilon_{22}(t=0^{+}) \to 0 \\
&2\lambda_{\infty}\delta\varepsilon_{22}(t=0^{+}) \to \frac{2(1+\nu)}{3}\mu_{\alpha} \\
&\frac{1}{\left(\frac{\tau^{\alpha}}{\bar{\tau}^{\alpha}}-1\right)}\frac{\delta\varepsilon_{22}(t=0^{+})}{\varepsilon_{11}} \to -(1+\nu)
\end{aligned} \tag{F.15}$$

and $\sigma_{11}$ evolves according to the expected equation

$$\frac{\sigma_{11}(t)}{\varepsilon_{11}} = E_{\infty} + 2(1+\nu)\mu_{\alpha}e^{-t/\tau^{\alpha}} \tag{F.16}$$

# Bibliography

L. Colombo A. La Magna, S. Coffa. A lattice kinetic Monte Carlo code for the description of vacancy diffusion and self-organization in Si. *Nuclear Instruments and Methods in Physics Research Section B*, 148:262–267, 1999. 9, 10

R. Abeyaratne and N. Triantafyllidis. An investigation of localization in porous elastic material using homogenization theory. *Journal of Applied Mechanics*, 51:481–486, 1984. 47

M. Abramowitz and I.A. Stegun. *Handbook of Mathematical Functions: With Formulas, Graphs, and Mathematical Tables*. Dover publications, 1965. 127, 129

D. C. Ahn, P. Sofronis, M. Kumar, J. Belak, and R. Minich. Void growth by dislocation-loop emission. *Journal of Applied Physics*, 101:063514, 2007. 4

A. V. Amirkhizi, J. Isaacs, J. Mcgee, and S. Nemat-Nasser. An experimentally-based viscoelastic constitutive model for polyurea, including pressure and temperature effects. *Journal of the Mechanics and Physics of Solids*, 25:217–233, 2006. 105

R. H. Van Stone ans J. A. Psioda. Discussion of "metallurgical factors affecting fracture toughness of aluminum alloys". *Metallurgical Transactions A*, 6:668–670, 1975. 124

T. Antoun, L. Seaman, D. R. Curran, G. I. Kanel, S. V. Razorenov, and A. V. Utkin. *Spall Fracture*. Springer, 2003. 4, 25

H. R. Azimi, R. A. Pearson, and R. W. Hertzberg. Fatigue of rubber-modified epoxies: effect of particle size and volume fraction. *Journal of Materials Science*, 31:3777–3789, 1996. xi, 1, 2

M. Bailey, L. Crum, O. Sapozhnikov, A. Evan, J. McAteer, R. Cleveland, and T. Colonius. Cavitation in shock wave lithotripsy. *Proceedings of the 5th International Symposium on Cavitation, Osaka, Japan*, 2003. xi, 2

J. M. Ball. Discontinuous equilibrium solutions and cavitation in nonlinear elasticity. *Philosophical Transactions of the Royal Society of London. Series A, Mathematical and Physical Sciences.*, 306:557–611, 1982. 1, 96

Y. Bao and T. Wierzbicki. On fracture locus in the equivalent strain and stress triaxiality space. *International Journal of Mechanical Sciences*, 46:81–98, 2004. 42

I. Barsoum and J. Faleskog. Rupture mechanisms in combined tension and shear experiments. *International Journal of Solids and Structures*, 44:1768–1786, 2007a. 42

I. Barsoum and J. Faleskog. Rupture mechanisms in combined tension and shear micromechanics. *International Journal of Solids and Structures*, 44:5481–5498, 2007b. 42

R. W. Bauer and H. G. F. Wilsdorf. Void initiation in ductile fracture. *Scripta Metallurgica*, 7:1213–1220, 1973. 1, 4

R. Becker and A. Needleman. Effect of yield surface curvature on necking and failure in porous plastic solids. *Journal of Applied Mechanics*, 53:491–499, 1986. 40

J. Belak. On the nucleation and growth of voids at high strain-rates. *Journal of Computer Aided-Materials Design*, 5:193–206, 1998. 4, 9

J. Belak. Incipient spallation fracture in light metals from 3D x-ray tomography, 2D microscopy, and molecular dynamic simulations. *11th International Conference on Fracture*, 2005. xi, 2

A. A. Benzerga and J. Besson. Plastic potentials for anisotropic porous solids. *European Journal of Mechanics. A*, 20:397–434, 2001. 42

J. Besson. Continuum models of ductile fracture: A review. *International Journal of Damage Mechanics*, 19:3–52, 2010. 41

J. Besson, G. Cailletaud, J. L. Chaboche, and S. Forest. *Non-Linear Mechanics of Materials*. Springer, 2010. 47

P. J. Blatz and W. L. Ko. Application of finite elastic theory to the deformation of rubbery materials*. *Transactions of the Society of Rheology*, 6:223–251, 1962. 118

G. Bolzon and R. Vitaliani. The Blatz-Ko material model and homogenization. *Archive of Applied Mechanics*, 63:228–241, 1993. 47

A. B. Bortz, M. H. Kalos, and J. L. Lebowitz. Energetics and kinetics of vacancy diffusion and aggregation in shocked aluminium via orbital-free density functional theory. *Journal of Computational Physics*, 17:10–18, 1975. 9, 11

S. C. Brenner and L. R. Scott. *The Mathematical Theory of Finite Element Methods*. Springer, 2000. 77

L. M. Brown and J. D. Embury. The initiation and growth of voids at second phase particles. *Proceedings of the 3rd International Conference on Strength of Metals and Alloys*, pages 164–169, 1973. 39

B. Budiansky, J. W. Hutchinson, and S.Slutsky. Void growth and collapse in viscous solids. *Mechanics of Solids. The Rodney Hill 60th Anniversary Volume*, pages 13–45, 1982. 40, 41

W.W. Byerly. *An Elementary Treatise on Fourier Series and Spherical, Cylindrical, and Ellipsoidal Harmonics with Applications to Problems in Mathematical Physics*. Ginn and Company., 1893. 78

F. Cardarelli. *Materials Handbook: A Concise Desktop Reference*. Springer, 2008. 22

M. M. Carrol and A. C Holt. Static and dynamic pre-collapse relations for ductile porous materials. *Journal of Applied Physics*, 43:1626–1636, 1972. 43, 103

P. Ponte Castañeda. The effective mechanical properties of nonlinear isotropic composites. *Journal of the Mechanics and Physics of Solids*, 39:45–71, 1991. 6, 47, 51, 52

P. Ponte Castañeda and P. Suquet. Nonlinear composites. *Advances in Applied Mechanics*, 34:171–302, 1998. 34

P. Ponte Castañeda and M. Zaidman. Constitutive models for porous materials with evolving microstructure. *Journal of the Mechanics and Physics of Solids*, 42:1459–1497, 1994. 34, 41

C. Cawthorne and E. J. Fulton. Voids in irradiated stainless steel. *Nature*, 216:575–576, 1967. 5

J. L. Chaboche. Continuum damage mechanics. 1 general concepts. *Journal of Applied Mechanics*, 55:59–64, 1988. 4

V. Chakkarapani, K. Ravi-Chandar, and K. M. Liechti. Characterization of multiaxial constitutive properties of rubbery polymers. *Journal of Engineering Materials and Technoloy*, 128:489–494, 2006. 105

Y. W. Chang, A. N. Gent, and J. Padovan. Expansion of a cavity in a rubber block under unequal stresses. *International journal of fracture*, 60:283–291, 1993. 95

M. S. Chou-Wang and C. O. Horgan. Cavitation in nonlinear elastodynamics for neo-Hookean materials. *International Journal of Engineering Science*, 27:967–973, 1989. 96

S. Christy, H. R. Pak, and M. A. Meyers. *Metallurgical Applications of Shock-Wave and High-Strain-Rate Phenomena*. New York and Basel, 1986. xi, 4, 5

D. Cioranescu and J. S. J. Paulin. Homogenization in open sets with holes. *Journal of Mathematical Analysis and applications*, 71:590–607, 1979. 51

A. C. F. Cocks and M. F. Ashby. On creep fracture by void growth. *Progress in Material Science*, 27:189–244, 1982. 8

R. Cortes. The growth of microvoid under intense dynamic loading. *International Journal of Solids and Structures*, 29:1339–1350, 1992a. 43

R. Cortes. Dynamic growth of microvoids under combined hydrostatic and deviatoric stresses. *International Journal of Solids and Structures*, 29:1637–1645, 1992b. 43

R. Courant, K. Friedrichs, and H. Lewy. Partial differential equations of mathematical physics. *Mathematische Annalen*, 100:32–74, 1928. 92

A. M. Cuitino and M. Ortiz. Ductile fracture by vacancy condensation in fcc single crystals. *Acta Materialia*, 44(2):427–436, 1996. 20

D. R. Curran, L. Seaman, and D. A. Shockley. Dynamic failure in solids. *Physics Today*, 30:46–55, 1977. xi, 2, 4

C. Czarnota, N. Jaques, S. Mercier, and A. Molinari. Modelling of dynamic ductile fracture and application to the simulation of plate impact tests on tantalum. *Journal of the Mechanics and Physics of Solids*, 56:1624 –1650, 2008. 44

J. Dai, W. D. Seider, and T. Sinno. Lattice kinetic Monte Carlo simulations of defect evolution in crystals at elevated temperature. *Molecular Simulation*, 32:305–314, 2006. 10

D. A. Dalton, J. Brewer, A. C. Bernstein, W. Grigsby, D. Milathianaki, E. Jackson, R. Adams, P. Rambo, J. Schwarz, A. Edens, M. Geissel, I. Smith, E. Taleff, and T. Ditmire. Laser-induced spall of aluminum and aluminum alloys at high strain rates. *Shocked Compression of Condensed Matter*, 955:501–504, 2007. 20

J. M. Duva and J. W. Hutchinson. Constitutive potentials for dilutely voided nonlinear materials. *Mechanics of Materials*, 3:41–54, 1984. 40

L. P. Dvila, P. Erhart, E. M. Bringa, M. A. Meyers, V. A. Lubarda, M. S. Schneider, R. Becker, and M. Kumar. Atomistic modeling of shock-induced void collapse in copper. *Applied Physics Letters*, 86:161902, 2005. 4

T. ElSayed, W. Mock, A. Mota, F. Fraternalli, and M. Ortiz. Computational assessment of ballistic impact on a high strength structural steel/polyurea composite plate. *Computational Mechanics*, 43:525–534, 2009. 105

J. Faleskog, X. Gao, and C. F. Shih. Cell model for nonlinear fracture analysis i. micromechanics calibration. *International Journal of Fracture*, 89:355–373, 1998. 39

H. Gao, Y. Huang, and W. D. Nix. Modeling plasticity at the micrometer scale. *Naturwissenschaften*, 86:507–515, 1999. 22

X. Gao and J. Kim. Modeling of ductile fracture: Significance of void coalescence. *International Journal of Solids and Structures*, 43:6277–6293, 2006. 42

W. M. Garrison and N. R. Moody. Ductile fracture. *Journal of Physics and Chemistry of Solids*, 48:1035–1074,, 1987. 3

V. Gavini. Role of macroscopic deformations in energetics of vacancies in aluminum. *Physical Review Letters*, 101:205503, 2008. xii, 16

V. Gavini. Role of the defect core in energetics of vacancies. *Proceedings of the Royal Society A*, 465:3239–3266, 2009a. 9, 15, 20, 21

V. Gavini. Private communication, 2009b. 22

A. N. Gent. Cavitation in rubber, a cautionary tale. *Rubber Chemistry and Technology*, 63:G49–G53, 1990. 96

A. N. Gent and P. B. Lindley. Internal rupture of bonded rubber cylinders in tension. *Proceedings of the Royal Society of London. Series A, Mathematical and Physical Sciences.*, 258:195–205, 1958. 1, 95

P. Germain, Q. S. Nguyen, and P. Suquet. Continuum thermodynamics. *Journal of Applied Mechanics*, 50:1010–1020, 1983. 34

G. Geymonat, S. Müller, and N. Triantafyllidis. Homogenization of nonlinearly elastic materials, microscopic bifurcation and macroscopic loss of rank-one convexity. *Archive for Rational Mechanics and Analysis*, 122:231–290, 1993. 124

W. F. Giauque and P. F. Meads. The heat capacities and entropies of aluminum and copper from 15 to 300 $^{\circ}K$. *Journal of the American Chemical Society*, 63 : 1897 − −1901, 1941. 23

M. Gologanu, J. B. Leblond, and J. Devaux. Approximate models for ductile metals containing non-spherical voids. Case of axisymmetric prolate ellipsoidal cavities. *Journal of the Mechanics and Physics of Solids*, 41:1723–1754, 1993. 41, 42

M. Gologanu, J. B. Leblond, and J. Devaux. Approximate models for ductile metals containing non-spherical voids. Case of axisymmetric oblate ellipsoidal cavities. *Journal of Engineering Materials and Technology*, 116:290–297, 1994. 41

S. H. Goods and L. M. Brown. The nucleation of cavities by plastic deformation. *Acta Metallurgica*, 27:1–15, 1979. 4, 39

R. A. Gordon. *The Integrals of Lebesgue, Denjoy, Perron, and Henstock*. Graduate Studies in Mathematics, 1994. 45

A. L. Gurson. Continuum theory of ductile rupture by void nucleation and growth: Part I - Yield criteria and flow rules for porous ductile media. *Journal of Engineering Materials and Technology*, 99:2–15, 1977a. 4, 7, 37, 99

A. L. Gurson. Porous rigid-plastic materals containing rigid inclusions - yield function, plastic potential, and void nucleation. *Proceedings of the International Conference on Fracture Mechanics*, 2A:357–364, 1977b. 4, 37, 38

B. P. Haley, K. M. Beardmore, and N. Gronbech-Jensen. Vacancy clustering and diffusion in silicon: Kinetic lattice monte carlo simulations. *Physical Review B*, 74:045217, 2006. 9

J. W. Hancock and A. C. Mackenzie. On the mechanisms of ductile failure in high-strength steels subjected to multi-axial stress-states. *Journal of the Mechanics and Physics of Solids*, 24:147–169, 1976. xi, 1, 5, 42

J. L. Hastings, S. K. Estreicher, and P. A. Fedders. Vacancy aggregates in silicon. *Physical Review B*, 56:10 215, 1997. 9

D. Henao. *Variational modelling of cavitation and fracture in nonlinear elasticity.* PhD thesis, University of Oxford, 2009. 96, 97

D. Henao and C. Mora-Corral. Invertibility and weak continuity of the determinant for the modelling of cavitation and fracture in nonlinear elasticity. *Archive for rational mechanics and analysis*, 197:619–655, 2010. 96, 124

R. Hill. A theory of the yielding and plastic flow of anisotropic metals. *Proceedings of the Royal Society of London. Series A*, 193:281–297, 1948. 42

R. Hill. Elastic properties of reinforced solids: some theoretical principles. *Journal of the Mechanics and Physics of Solids*, 11:357–372, 1963. 6, 35, 50

R. Hill. The essential structure of constitutive laws for metal composites and polycrystals. *Journal of the Mechanics and Physics of Solids*, 15:79–95, 1967. 6, 35, 50

R. Hill. On constitutive macro-variables for heterogeneous solids at finite strain. *Proceedings of the Royal Society of London*, 326:131–147, 1972. 6, 35, 47, 50, 51, 54

R. Hill. On macroscopic effects of heterogeneity in elastoplastic media at finite strain. *Mathematical Proceedings of the Cambridge Philosophical Society*, 95:481–494, 1984. 50

R. Hill and J. R. Rice. Elastic potentials and the structure of inelastic constitutive laws. *SIAM Journal on Applied Mathematics*, 25:448–461, 1973. 47, 51

G. Ho, M. T. Ong, K. J. Caspersen, and E. A. Carter. Energetics and kinetics of vacancy diffusion and aggregation in shocked aluminium via orbital-free density functional theory. *Physical Chemistry Chemical Physics*, 9:4951–4966, 2007. xii, 9, 15, 16

C. O. Horgan and D. A. Polignone. Cavitation in nonlinearly elastic solids: A review. *Applied Mechanics Reviews*, 48:471–485, 1995. 96

H. S. Hou and R. Abeyaratne. Cavitation in elastic and elastic-plastic solids. *Journal of the Mechanics and Physics of Solids*, 40:571–591, 1992. 97

Y. Huang and A. J. Kinloch. The role of plastic void growth in the fracture of rubber-toughened epoxy polymers. *Journal of Materials Science Letters*, 11:484–487, 1992. 1

Y. Huang, J. W. Hutchinson, and V. Tvergaard. Cavitation instabilities in elastic-plastic solids. *Journal of the Mechanics and Physics of Solids*, 39:223–241, 1991. 97

D. Hull and D. E. Rimmer. The growth of grain-boundary voids under stress. *Philosophical Magazine*, 4:673–687, 1959. 4

J. W. Hutchinson and V. Tvergaard. Shear band formation in plane strain. *International Journal of Solids and Structures*, 17:451–470, 1981. 40

G. R. Irwin and D. C. Washington. Analysis of stresses and strains near the end of a crack traversing a plate. *Journal of Applied Mechanics*, 24:361–364, 1957. 3

J. N. Johnson and F. L. Addessio. Virtual time. *ACM transactions on programming languages and systems*, 7:404–425, 1985a. 12

J. N. Johnson and F. L. Addessio. Fracture characteristics of three metals subjected to various strains, strain rates, temperatures and pressures. *Engineering Fracture Mechanics*, 21:31–48, 1985b. 1

M. Kailasam and P. P. Castañeda. A general constitutive theory for linear and nonlinear particulate media with microstructure evolution. *Journal of the Mechanics and Physics of Solids*, 46:427–465, 1998. 41

M. Kailasam, N. Aravas, and P. Ponte Castañeda. Porous metals with developing anisotropy: Constitutive models, computational issues and applications to deformation processing. *Computer Modeling in Engineering and Sciences*, 1:105–118, 2000. 41

U. Kaiser, D. A. Muller, J. L. Grazul, A. Chuvilin, and M. Kawasaki. Direct observation of defect-mediated cluster nucleation. *Nature Materials*, 1:102–105, 2002. 3

C. Kane, J. E. Marsden, M. Ortiz, and M. West. Variational integrators and the newmark algorithm for conservative and dissipative mechanical systems. *International Journal for Numerical Methods in Engineering*, 49:1295–1325, 2000. 72

G. I. Kanel, S. V. Razorenov, K. Baumung, and J. Singer. Dynamic yield and tensile strength of aluminum single crystals at temperatures up to the melting point. *Journal of Applied Physics*, 90:136–143, 2001. 20

M. F. Kanninen and C. H. Popelar. *Advanced Fracture Mechanics*. Oxford University Press, 1985. 3

J. Keck. Statistical investigation of dissociation cross-sections for diatoms. *Engineering Fracture Mechanics*, 33:173–182, 1962. 13

J. Kim, X. Gao, and T. S. Srivatsan. Modeling of void growth in ductile solids: effects of stress triaxiality and initial porosity. *Engineering Fracture Mechanics*, 71:379–400, 2004. 42

W. G. Knauss and J. Zhao. Improved relaxation time coverage in ramp-strain histories. *Mechanics of Time-Dependent Materials*, 11:199–216, 2007. 105, 108, 112, 115, 142

J. Koplik and A. Needleman. Void growth and coalescence in porous plastic solids. *International Journal of Solids and Structures*, 24:835–853, 1988. 4

Y. W. Kwon, D. H. Allen, and R. Talreja. *Multiscale Modeling and Simulation of Composite Materials and Structures*. Springer, 2008. 47

J. B. Leblond, G. Perrin, and P. Suquet. Exact results and approximate models for porous viscoplastic solids. *International Journal of Plasticity*, 10:213–235, 1994. 41

J. B. Leblond, G. Perrin, and J. Devaux. An improved Gurson-type model for hardenable ductile metals. *European Journal of Mechanics. A, Solids*, 14:499–527, 1995. 40

B. J. Lee and M. E. Mear. Axisymmetric deformation of power-law solids containing a dilute concentration of aligned spheroidal voids. *Journal of the Mechanics and Physics of Solids*, 40:1805–1836, 1992. 41

J. Lemaitre. Local approach of fracture. *Engineering Fracture Mechanics*, 25:523–537, 1986. 34

A. Lew, J. E. Marsden, M. Ortiz, and M. West. Variational time integrators. *International Journal for Numerical Methods in Engineering*, 60:153–212, 2004. 72

B. Li, F. Habbal, and M. Ortiz. Optimal transportation meshfree approximation schemes for fluid and plastic flows. *International Journal for Numerical Methods in Engineering*, pages 1–39, 2010. 120

C. Li and J. Lua. A hyper-viscoelastic constitutive model for polyurea. *Materials Letters*, 63:877–880, 2009. 105

C. L. Liu and J. B. Adams. Structure and diffusion of clusters on ni surfaces. *Surface Science*, 72:73–86, 1992. 9

A. Lo and R. T. Skodje. Kinetic and Monte Carlo models of thin film coarsening: Cross over from diffusion-coalescence to ostwald growth modes. *Journal of Chemical Physics*, 112:1966–1974, 2000. 10

O. Lopez-Pamies. Onset of cavitation in compressible, isotropic, hyperelastic solids. *Journal of elasticity*, 94:115–145, 2009. 96

B. D. Lubachevsky. Efficient parallel simulations of dynamic ising spin systems. *Journal of Computational Physics*, 75:103–122, 1988. 12

V. A. Lubarda, M. S. Schneider, D. H. Kalantar, B. A. Regminton, and M. A. Meyers. Void growth by dislocation emission. *Acta Materiala*, 52:1397–1408, 2004. 123

J. Lubliner. On the structure of the rate equations of materials with internal variables. *Acta Mechanica*, 17:109–119, 1973. 71

J. Lubliner. *Plasticity Theory*. Macmillan, 1990. 97

R. L. Lyles and H. G. F. Wilsdorf. Microcrack nucleation and fracture in silver crystals. *Acta Metallurgica*, 23:269, 1975. 4

E. Maire, C. Bordreuil, L. Babout, and J. C. Boyer. Damage initiation and growth in metals. comparison between modelling and tomography experiments. *Journal of the Mechanics and Physics of Solids*, 53:2411–2434, 2005. 3

J. Marian, J. Knap, and M. Ortiz. Nanovoid cavitation by dislocation emission in aluminum. *Physical Review Letters*, 93:165503, 2004. 4, 6, 10, 21, 22

J. Marian, J. Knap, and M. Ortiz. Nanovoid deformation in aluminum under simple shear. *Acta Materialia*, 53:2893–2900, 2005. 4, 21

B. Marini, F. Mudry, and A. Pineau. Experimental study of cavity growth in ductile rupture. *Engineering Fracture Mechanics*, 22:989–996, 1985. 37

J. E. Marsden and T. J. R. Hughes. *Mathematical Foundations of Elasticity*. Dover, 1993. 52, 56

J. E. Marsden and T. S.Ratiu. *Introduction to Mechanics and Symmetry*. Springer, 1999. 52

E. Martinez, J. Marian, M. H. Kalos, and J. M. Perlado. Synchronous parallel kinetic monte carlo for continuum diffusion-reaction systems. *Journal of Computational Physics*, 227: 3804–3823, 2008. xi, 9, 11, 12, 13, 17

F. A. McClintock. A criterion for ductile fracture by the growth of holes. *Journal of Applied Mechanics*, 35:363–371, 1968. 36

M. E. Mear and J. W. Hutchinson. Influence of yield surface curvature on flow localization in dilatant plasticity. *Mechanics of Materials*, 4:395–407, 1985. 40

M. A. Meyers. *Dynamic Behaviour of Materials*. Wiley-Interscience, 1994. 22, 23

M. A. Meyers and C. T. Aimone. Dynamic fracture (spalling) of metals. *Progress in Materials Science*, 28:1–96, 1983. 123

M. A. Meyers, S. Traiviratana, V. A. Lubarda, D. J. Benson, and E. M. Bringa. The role of dislocations in the growth of nanosized voids in ductile failure of metals. *JOM Journal of the Minerals, Metals and Materials Society*, 61:35–41, 2009. 6

J. C. Michel and P. Suquet. The constitutive law of nonlinear viscous and porous materials. *Journal of the Mechanics and Physics of Solids*, 40:783–812, 1992. 41

A. Molinari and S. Mercier. Micromechanical modelling of porous materials under dynamic loading. *Journal of the Mechanics and Physics of Solids*, 49:1497–1516, 2001. 6, 35, 44, 50, 60, 103

V. Monchiet, O. Cazacu, E. Charkaluk, and D. Kondo. Macroscopic yield criteria for plastic anisotropic materials containing spheroidal voids. *International Journal of Plasticity*, 24: 1158–1189, 2008. 42

T. F. Morgeneyer, M. J. Starink, and I. Sinclair. Evolution of voids during ductile crack propagation in an aluminium alloy sheet toughness test studied by synchrotron radiation computed tomography. *Acta Materialia*, 56:1671–1679, 2008. 3

S. Müller. Homogenization of nonconvex integral functionals and cellular elastic materials. *Archive for Rational Mechanics and Analysis*, 99:189–212, 1987. 52

L. E. Murr. *Interfacial Phenomena in Metals and Alloys*. Reading, Mass., 1975. 22

K. Nahshon and J. W. Hutchinson. Modification of the gurson model for shear failure. *European Journal of Mechanics A/Solids*, 27:1–17, 2008. 43

A. Neddleman. Void growth in an elasti-plastic medium. *Journal of Applied Mechanics*, 41: 964–970, 1972. 38

A. Neddleman. A continuum model for void nucleation by inclusion debonding. *Journal of Applied Mechanics*, 54:525–531, 1987. 4

S. Nemat-Nasser. Averaging theorems in finite deformation plasticity. *Mechanics of Materials*, 31:493–523, 1999. 6, 35, 50

N. Newmark. A method of computation for structural dynamics. *ASCE Journal of the Engineering Mechanics Division*, 85:67–94, 1959. 72

R. W. Ogden. On the overall moduli of non-linear elastic composite materials. *Journal of the Mechanics and Physics of Solids*, 22:541–553, 1974. 6, 35, 47, 50, 51

M. Ortiz. *Continuum Mechanics Course Notes. Ae 160.* 2010. 61

M. Ortiz and A. Molinari. Effect of strain hardening and rate sensitivity on the dynamic growth of a void in a plastic material. *Journal of Applied Mechanics - Transactions of the ASME*, 59:48–53, 1992. 43

M. Ortiz and L. Stainier. The variational formulation of viscoplastic constitutive updates. *Computer Methods in Applied Mechanics and Engineering*, 171:419–444, 1999. 82

J. Pan, M. Saje, and A. Needleman. Localization of deformation in rate sensitive porous plastic solids. *International Journal of Fracture*, 21:261–278, 1983. 41

T. Pardoen and J. W. Hutchinson. An extended model for void growth and coalescence. *Journal of the Mechanics and Physics of Solids*, 48:2467–2512, 2000. 4

O. Penrose. The becker-döring equations at large times and their connection with the lsw theory. *Journal of Statistical Physics*, 89:305–320, 1997. 9

R. Phillips. *Crystals, defects and microstructure: modeling across scales.* Cambridge University Press, 2001. 5, 20

A. Pineau. *Advances in Fracture Research.* Cambridge University Press, 1982. 34

A. Pineau. Development of the local approach to fracture over the past 25 years: theory and applications. *International Journal of Fracture*, 138:139–166, 2006. 4, 34

Y. A. Pishchalnikov, O. A. Sapozhnikov, M. R. Bailey, J. C. Williams, Jr. R. O. Cleveland, T. Colonius, L. A. Crum, A. P. Evan, and J. A. McAteer. Cavitation bubble cluster activity in the breakage of kidney stones by lithotripter shockwaves. *Journal of Endourology*, 17:435–446, 2003. 1

D. A. Porter and K. E. Easterling. *Phase Transformations in Metals and Alloys*. Chapman and Hall, 1981. 20, 21

G. P. Potirniche, J. L. Hearndon, M. F. Horstemeyer, and X. W. Ling. Lattice orientation effects on void growth and coalescence in fcc single crystals. *International Journal of Plasticity*, 22:921–942, 2006. 4

K. E. Puttick. Ductile fracture in metals. *Philosophical Magazine*, 4:964–969, 1959. 4

R. Radovitzky and M. Ortiz. Error estimation and adaptive meshing in strongly nonlinear dynamic problems. *Computer Methods in Applied Mechanics and Engineering*, 172:203–240, 1999. 52, 71, 72

R. Raj and M. F. Ashby. Intergranular fracture at elevated temperature. *Acta Metallurgica*, 23:653–666, 1975. 8

J. R. Rice. A path independent integral and the approximate analysis of strain concentration by notches and cracks. *Journal of Applied Mechanics*, 35:379–386, 1968. 3

J. R. Rice and D. M. Tracey. On the ductile enlargement of voids in triaxial stress fields. *Journal of the Mechanics and Physics of Solids*, 17:201–217, 1969. 36, 40, 41

C. M. Roland and R. Casalini. Effect of hydrostatic pressure on the viscoelastic response of polyurea. *Polymer*, 48:5747–5752, 2007. 105

C. M. Roland, J. N. Twigg, Y. Vu, and P. H. Mott. High strain rate mechanical behavior of polyurea. *Polymer*, 48:574–578, 2007. 105

G. Rousselier. Ductile fracture models and their potential in local approach of fracture. *Nuclear Engineering and Design*, 105:97–111, 1987. 34

R. E. Rudd and J. F. Belak. Void nucleation and associated plasticity in dynamic fracture of polycrystalline copper: an atomistic simulation. *Computational Materials Science*, 24: 148–153, 2002. 4, 9

R. E. Rudd and J. Q. Broughton. Concurrent coupling of length scales in solid state systems. *Physica Status Solidi - B - Basic Solid State Physics*, 217:251–291, 2000. 4

I. Saiki, K. Terads, K. Iked, and M. Hori. Appropriate number of unit cells in a representative volume element for micro-structural bifurcation encountered in a multi-scale modeling. *Computer Methods in Applied Mechanics and Engineering*, 191:2561–2585, 2002. 124

E. Sanchez-Palencia. *Non-Homogeneous Media and Vibration Theory (Lecture Notes in Physics)*. Springer, 1980. 52

G. Sansone. *Orthogonal Functions*. Interscience Publishers, 1959. 77, 78

S. S. Sarva, S. Deschanel, M. C. Boyce, and W. Chen. Stress-strain behavior of a polyurea and a polyrethane from low to high strain rates. *Polymer*, 48:2208–2213, 2007. xv, 105, 107, 110, 112, 113, 114, 115, 117, 119

F. Seitz. On the theory of vacancy diffusion in alloys. *Physical review*, 74:1513–1523, 1948. 9

E. T. Seppälä, J. Belak, and R. E. Rudd. Effect of stress triaxiality on void growth in dynamic fracture of metals: A molecular dynamics study. *Physical Review B*, 69:134101, 2004. 4

S. Shima and M. Oyane. Rigorous synchronous relaxation algorithm for parallel kinetic monte carlo simulations of thin film growth. *Physical review. B, Condensed matter and materials physics*, 71:115436, 2005. 12

K. E. Sickafus, E. A. Kotomin, and B. P. Uberuaga. *Radiation Effects in Solids*. Springer, 2007. 11

T. Sinno, Z. K. Jiang, and R. A. Brown. Atomistic simulation of point defects in silicon at high temperature. *Applied Physics Letters*, 68:3028–3030, 1996. 9

R. J. M. Smit, W. A. M. Brekelmans, and H. E. H. Meijer. Prediction of the mechanical behavior of nonlinear heterogeneous systems by multi-level finite element modeling. *Computer Methods in Applied Mechanics and Engineering*, 155:181–192, 1998. 34

M. R. Sorensen and A. F. Voter. Temperature-accelerated dynamics for simulation of infrequent events. *Journal of Chemical Physics*, 112:9599–9606, 2000. 14

P. Steinmann, C. Miehe, and E. Stein. On the localization analysis of orthotropic hill type elastoplastic solids. *Journal of the Mechanics and Physics of Solids*, 42:1969–1994, 1994. 42

A. L. Stevens, L. Davison, and W. E. Warren. Spall fracture in aluminum monocrystals: a dislocation-dynamics approach. *Journal of Applied Physics*, 43:4922–4927, 1972. 123

A. Strachan, T. Cagin, and W. A. Goddard III. Critical behavior in spallation failure of metals. *Physical Review B*, 63:060103, 2001. 20

A. H. Stroud. *Numerical Quadrature and Solution of Ordinary Differential Equations*. Springer-Verlag, 1974. 81

Z. Su and P. Coppens. Rotation of real spherical harmonics. *Acta Crystallographica Section A*, 50:636 –643, 1994. 78

K. Terada and N. Kikuchi. A class of general algorithms for multi-scale analyses of heterogeneous media. *Computer Methods in Applied Mechanics and Engineering*, 190:5427–5464, 2001. 52

W. Tong and G. Ravichandran. Dynamic pore collapse in viscoplastic materials. *Journal of Applied Physics*, 74:2425–2435, 1993. 43

F. R. Tuler and B. M. Butcher. A criterion for the time dependence of dynamic fracture. *The International Journal of Fracture Mechanics*, 4:431–437, 1968. 4

V. Tvergaard. Effect of kinematic hardening on localized necking in biaxially stretched sheets. *International Journal of Mechanical Sciences*, 20:651–658, 1978. 40

V. Tvergaard. Influence of voids on shear band instabilities under plane strain conditions. *International Journal of Fracture*, 17:389–407, 1981a. 38, 39

V. Tvergaard. Ductile fracture by cavity nucleation between larger voids. *Journal of the Mechanics and Physics of Solids*, 30:265–286, 1981b. 124

V. Tvergaard. Material failure by void coalescence in localized shear bands. *International Journal of Fracture*, 18:659–672, 1982. xii, 38

V. Tvergaard. Effect of yield surface curvature and void nucleation on plastic flow localization. *Journal of the Mechanics and Physics of Solids*, 35:43–60, 1987. 40

V. Tvergaard. Material failure by void growth to coalescence. *Advances in Applied Mechanics*, 27:83–151, 1990. 1, 4, 38

V. Tvergaard and A. Needleman. Analysis of the cup-cone fracture in a round tensile bar. *Acta Metallurgica*, 32:157–169, 1984. 38, 39

B. P. Uberuaga, R. Smith, A. R. Cleave, F. Montalenti, G. Henkelman, R. W. Grimes, A. F. Voter, and K. E. Sickafus. Structure and mobility of defects formed from collision cascades in mgo. *Physical Review Letters*, 92:115505, 2004. 9

G. H. Vineyard. Frequency factors and isotope effects in solid state rate processes. *Journal of Physics and Chemistry of Solids*, 3:121–127, 1957. 9, 13

P. M. Voyles, D. A. Muller, J. L. Grazul, P. H. Citrin, and H. J. L. Gossmann. Atomic-scale imaging of individual dopant atoms and clusters in highly n-type bulk si. *Nature*, 416: 826–829, 2002. 3

Z. P. Wang and C. T. Sun. Modeling micro-inertia in heterogeneous materials under dynamic loading. *Wave motion*, 36:473–485, 2002. 6, 35

K. Weinberg and T. Böhme. Condensation and growth of Kirkendall voids in intermetallic compounds. *IEEE Transactions on components and packaging technologies*, 32:684–692, 2009. 9

K. Weinberg and M. Ortiz. Kidney damage in extracorporeal shock wave lithotripsy: a numerical approach for different shock profiles. *Biomechanics and Modeling in Mechanobiology*, 8:285–299, 2009. 4

K. Weinberg, A. Mota, and M. Ortiz. A variational constitutive model for porous metal plasticity. *Computational Mechanics*, 37:142–152, 2006. 43

J. H. Weiner. *Statistical Mechanics of Elasticity*. Dover, 2002. 14

M. L. Williams and R. A. Schapery. Spherical flaw instability in hydrostatic tension. *International Journal of Fracture Mechanics*, 1:64–71, 1965. 96

W. G. Wolfer. The pressure for dislocation loop punching by a single bubble. *Philosophical Magazine A*, 58:285–297, 1988. 123

T. W. Wright and K. T. Ramesh. Dynamic void nucleation and growth in solids: A self-consistent statistical theory. *Journal of the Mechanics and Physics of Solids*, 56:336–359, 2008. 60

L. Xue. Damage accumulation and fracture initiation in uncracked ductile solids subject to triaxial loading. *International Journal of Solids and Structures*, 44:5163–5181, 2007. 43

W. M. Young and E. W. Elcock. Monte carlo studies of vacancy migration in binary ordered alloys: I. *Proceedings of the Physical Society of London*, 89:735–746, 1966. 9

K. S. Zhang, J. B. Bai, and D. François. Numerical analysis of the influence of the lode parameter on void growth. *International Journal of Solids and Structures*, 38:5847–5856, 2001. 42

Z. L. Zhang, C. Thaulow, and J. Odegård. A complete Gurson model approach for ductile fracture. *Engineering Fracture Mechanics*, 67:155–168, 2000. 39

W. Zhu, Z. Song, X. Deng, H. He, and X. Cheng. Lattice orientation effect on the nanovoid growth in copper under shock loading. *Physical Review B*, 75:024104, 2007. 4

M. G. Zielonka. *Configurational forces and variational mesh adaption in solid dynamics*. PhD thesis, California Institute of Technology, 2006. 52